Solar Power Generation Capability and Three-Port Converters for PV-Battery Powered Applications

by

Mohammad Al-Soeidat

A Thesis Submitted in Fulfillment of the
Requirements for the Degree

Doctor of Philosophy

University of Technology Sydney

Faculty of Engineering and Information Technology

School of Electrical and Data Engineering

Sydney, Australia

January, 2020

Certificate of Originality

I certify that the work in this thesis has not previously been submitted for a degree nor has it been submitted as part of requirements for a degree except as part of the collaborative doctoral degree and/or fully acknowledged within the text.

I also certify that the thesis has been written by me. Any help that I have received in my research work and the preparation of the thesis itself has been acknowledged. In addition, I certify that all information sources and literature used are indicated in the thesis. This research is funded by the Al-Hussein Bin Talal University scholarship. This research is supported by Australian Government Research Training Program.

Production Note:
Signature: Signature removed prior to publication.

Date: 7/1/2020
Mohammad Al-Soeidat

ABSTRACT

Solar energy is one of the most useful sources of sustainable energy. Intermittency negatively affects the efficiency and reliability of solar power. To mitigate such a problem, a power electronic converter is used to enhance the solar power generation capability, such as detecting faulty solar photovoltaic (PV) cells to be eliminated from the solar system or tracking the maximum power point (MPPT). Other advantages of power converters are integrating energy storage systems (ESS) with the solar energy system and managing power flow.

Solar cell power performance is greatly affected by two critical factors, aging and cracks. In order to mitigate their negative effects on the solar system, these cells are to be substituted by new cells; therefore, replacing the solar panels. In this research, an active crack detection method is proposed that can detect the cracked cells within a solar string by using AC parameter characterization without a need to have a physical inspection.

In this research, an analog voltage-based MPPT algorithm for individual PV module is proposed and experimentally verified. The maximum power points of solar cell can be joined by an approximately linear line. The slope of this line varies depending on the type and characteristic of the panels. Utilizing this characteristic, a bipolar junction transistor (BJT) is used to implement a variable voltage reference as the DC load line of the BJT can be designed to match the MPP line of the PV panel. This improves the accuracy of the maximum power point reference voltage without the need for a digital controller or PID controller.

This research also proposes two novel compact three-port converters. The proposed converters are used to interface a PV module, battery and load. The proposed converters are able to achieve MPPT, battery power management and output voltage regulation simultaneously. The first converter can be used for a stand-alone system or in a microgrid structure. The second converter is useful when bidirectional power flow is needed at the output port for some applications, such as grid-connected

solar system and electric vehicle where regenerative braking is used. Each converter combines three converters to form one integrated converter by sharing some components such as switches, inductors and capacitors. Thus, the converters have a high power density and fewer components compared to the traditional DC-DC converters. The integrated PV-battery system is the promised solution for both intermittency and the unpredictable load demand.

I would like to dedicate my thesis

To my parents:
Raja Al-Soeidat and Hadieh Khlifat
for their unconditional love.

To my academic advisor:
A/Prof. Dylan Dah-Chuan Lu

To my wife and daughter:
Lina Dweirj and Farah Al-Soeidat

To my family and friend
for their immense support.

Acknowledgements

First and foremost, it is one of the greatest pleasures to be able to pursue my PhD at the University of Technology Sydney, a stimulating environment in which I could grow academically. Throughout this endeavour, I have received a great deal of support and assistance. I would like to express my gratitude to those who believed and trusted in me throughout my study.

In particular, I would like to express my gratitude to my supervisor A/Prof. Dylan Dah-Chuan Lu, whose expertise was invaluable in the formulating of the research topic and for his guidance through each stage of the process to dig deeper into my research area. Your contribution and time are very much appreciated.

In addition, I would like to extend my thanks to Al-Hussein Bin Talal University for their generosity and financial support as they funded my PhD study through the university scholarships. Thank you for enabling this opportunity!

I am grateful for my co-supervisor, Prof. Jianguo Zhu, for his advice and encouragement. I am grateful to my colleagues in our research group. I wish to acknowledge an incomplete list of group members: Alexis Cembrano, Tian Cheng, Habes Khawaldeh, Hamzeh Aljarajreh, Qi Yao, Kaixin Wel, Nurhakimah Mohd Mukhtar and Muhammad Mubashir Alam.

Last and not least, I would like to thank my parents, wife and family for their wise counsel and sympathetic ear. Finally, there are my friends, who were of great support in deliberating over our problems and findings, as well as providing a happy distraction to rest my mind outside of my research.

Mohammad Al-Soeidat
Sydney, Australia, 2020.

List of Publications

Journal Papers

J-1. T. Cheng, **M. Al-Soeidat**, D.D.C. Lu and V. Agelidis, "Experimental study of PV strings affected by cracks," *IET The Journal of Engineering*, vol. 2019, no. 18, pp. 5124-5128, 2019. Available: 10.1049/joe.2018.9320.

J-2. **M. Al-Soeidat**, D.D.C. Lu, and J. Zhu, "An analog BJT-tuned maximum power point tracking technique for PV systems," *IEEE Transactions on Circuits and Systems II: Express Briefs*, vol. 66, no. 4, pp. 637-641, April 2019. doi: 10.1109/TCSII.2018.2865804

J-3. **M. Al-Soeidat**, H. Aljarajreh, H. Khawaldeh, D.D.C. Lu, and J. Zhu, "A Reconfigurable Three-Port DC-DC Converter for Integrated PV-Battery System," *IEEE Journal of Emerging and Selected Topics in Power Electronics*, doi: 10.1109/JESTPE.2019.2941595

J-4. **M. Al-Soeidat**, T. Cheng, D. D. Lu and V. G. Agelidis, "Experimental study of static and dynamic behaviours of cracked PV panels," *IET Renewable Power Generation*, vol. 13, no. 16, pp. 3002-3008, 9 12 2019. doi: 10.1049/iet-rpg.2019.0359

Conference Papers

C-1. **M. Al-Soeidat**, H. Khawaldeh, and D.D.C. Lu, "A Novel High Step-up Three-Port Bidirectional DC/DC Converter for PV-Battery Integrated System," *2020 IEEE Applied Power Electronics Conference (APEC)*, March 2020.

C-2. **M. Al-Soeidat**, H. Khawaldeh, H. Aljarajreh, and D.D.C. Lu, "A compact three-port DC-DC converter for integrated PV-battery system," *2018 IEEE International Power Electronics and Application Conference and Exposition (PEAC)*, Nov 2018, pp. 1-6.

C-3. H. A. Khawaldeh, H. Aljarajreh, **M. Al-Soeidat**, D.D.C. Lu, and L. Li, "Performance investigation of a PV emulator using current source and diode string," *2018 26th International Conference on Systems Engineering (ICSEng)*, Dec 2018, pp. 1-5.

C-4. **M. R. Al-Soeidat**, D.D.C. Lu and J. Zhu, "A more accurate analog voltage based photovoltaic maximum power point tracking technique," *2017 8th International Renewable Energy Congress (IREC)*, March 2017, pp. 1-5.

C-5. **M. R. Al-Soeidat**, A. Cembrano, and D.D.C. Lu, "Comparing effectiveness of hybrid MPPT algorithms under partial shading conditions," *2016 IEEE International Conference on Power System Technology (POWERCON)*, Sep. 2016, pp. 1-6.

Contents

List of Figures

List of Tables

Abbreviation

PV	Photovoltaics
MPP	Maximum Power Point
MPPT	Maximum Power Point Tracking
DMPPT	Distributed Maximum Power Point Tracking
ESS	Energy Storage Systems
SC	Supercapacitor
DC	Direct Current
AC	Alternating Current
I-V Curve	Current-voltage Characteristic Curve
P-V Curve	Power-Voltage Characteristic Curve
FF	Fill Factor
MPC	Multiport Converter
TPC	Three-port Converter
STC	Standard Testing Condition (nominal condition)
HS-NITPC	High Step-up Non-isolated Three-port DC-DC Converter
PSC	Partial Shading Condition
Btu	British Thermal Units
RES	Renewable Energy Sources
BJT	Bipolar Junction Transistor
MOSFET	Metal Oxide Semiconductor Field Effect Transistor
SoC	State of Charge

EV	Electric Vehicle
FOC	Fraction Open Circuit
FSC	Fraction Short Circuit
P&O	Perturb and Observe
InC	Incremental Conduction Method
OCC	One-cycle Control
KVL	Kirchhoff's voltage law
MIMO	Multi-input Multi-output
SISO	Single-input Single-output
SIDO	Single-input Dual-output
DO	Dual-output
DI	Dual-input
DISO	Dual-input Single-output
DIDO	Dual-input Dual-output
CCM	Continuous Conduction Mode
DCM	Discontinuous Conduction Mode
PFM	Pulse-frequency Modulation
TPHBC	Three-port Half-bridge Converter
TPHBC-PR	Three-port Half-bridge Converter with Post Regulation
TPHBC-SR	Three-port Half-bridge Converter Synchronous Regulation
TPHBC-PF	Three-port Half-bridge Converter with Primary Freewheeling
SSPS	Secondary-side Phase-shift
FB-TPC	Full-bridge Three-port Converter

Nomenclature

P_{mpp}	Solar cell power at the maximum power point
I_{sc}	Solar cell short circuit current
V_{oc}	Solar cell open-circuit voltage
I_{ph}	Solar cell light-generated current
D_f	Forward-biased diode
R_{sh}	Shunt resistance
R_s	Series resistance
C_p	Parallel capacitance
$I_{sc;n}$	Short-circuit light-generated current at the nominal condition
K_i	Temperature coefficient of the short circuit current
T	Temperature
T_n	Temperature at nominal condition
G	Irradiance
G_n	Irradiance at nominal condition
V_t	Diode thermal voltage
k	Boltzmann's constant
q	Electron charge.
N_s	Number of series cells
I_d	Diode current
I_0	Diode reverse saturation current
n	Ideality factor of the solar cell diode
I_{sh}	Shunt resistance current
I_{pv}	Solar cell current
Z	Impedance
ω	Angular frequency

C_d	Diffusion capacitance
C_t	Transition capacitance
b	Constant depends on the solar cell
V_j	Junction voltage
V_a	Applied voltage
A	Area of the solar cell
ϵ_0	Permittivity of free space
ϵ_r	Permittivity of the solar cell material
N_D	Doping concentration for n region
N_A	Doping concentration p region
N_i	Intrinsic concentration of electrons & holes for the base semiconductor
τ	Minority carrier lifetime
K_1	Voltage proportional constant
R_B	BJT base resistor
R_C	BJT collector resistor
R_E	BJT emitter resistor
I_B	BJT base current
I_C	BJT collector current
I_E	BJT emitter current
β	BJT DC current gain
V_{BE}	BJT base-emitter voltage
V_{CE}	BJT collector-emitter voltage
R_{PV}	Equivalent resistance seen by the PV panel
R_O	Equivalent resistance of the PV panel
V_{ref}	Reference voltage from BJT

V_{init}	Initial reference voltage to BJT
R_{sens}	Small resistor that is used to measure the PV module output current
V_{sens}	Sensed PV module voltage

Chapter 1

Introductions

1.1 Renewable Energy

The world's population was 2.5 billion in 1950. It, however, reaches 7.6 billion as of mid-2017, and it is predicted to become 9.8 billion by 2050 and 11.2 billion by 2100 [105]. Due to this growing number and the worldwide development, the demand for energy has surged in the commercial, industrial, agricultural and domestic sector. According to [79], total world energy consumptions will rise from 549 quadrillion British thermal units (Btu) in 2012 to 815 quadrillion Btu in 2040, which is an increase of 48%. This high demand for energy has led to an energy crisis in recent years as electrical energy becomes an essential requirement for human lives [95].

In fact, most of the energy is generated by burning traditional sources of energy, such as fossil fuels: coal, oil and natural gas. In fact, these traditional energy sources cannot be replenished in a short time, so it is likely that these resources will run out in the near future. Thus, the cost of generating energy from traditional sources will continually increase [58]. In addition to the increasing concern of the traditional sources of energy shortage, burning of fuel is considered a major cause of many environmental problems, such as global warming and air pollution. It is expected that the world carbon dioxide emissions (CO2), caused by generating energy, will rise from 32.2 billion metric tons in 2012 to 43.2 metric tons by 2040 [79]. Carbon dioxide is one of the greenhouse gas that has causes global warming.

An overwhelming need for renewable energy sources, including wind, solar, geothermal, biomass and hydropower energy have arisen in the world to solve these energy

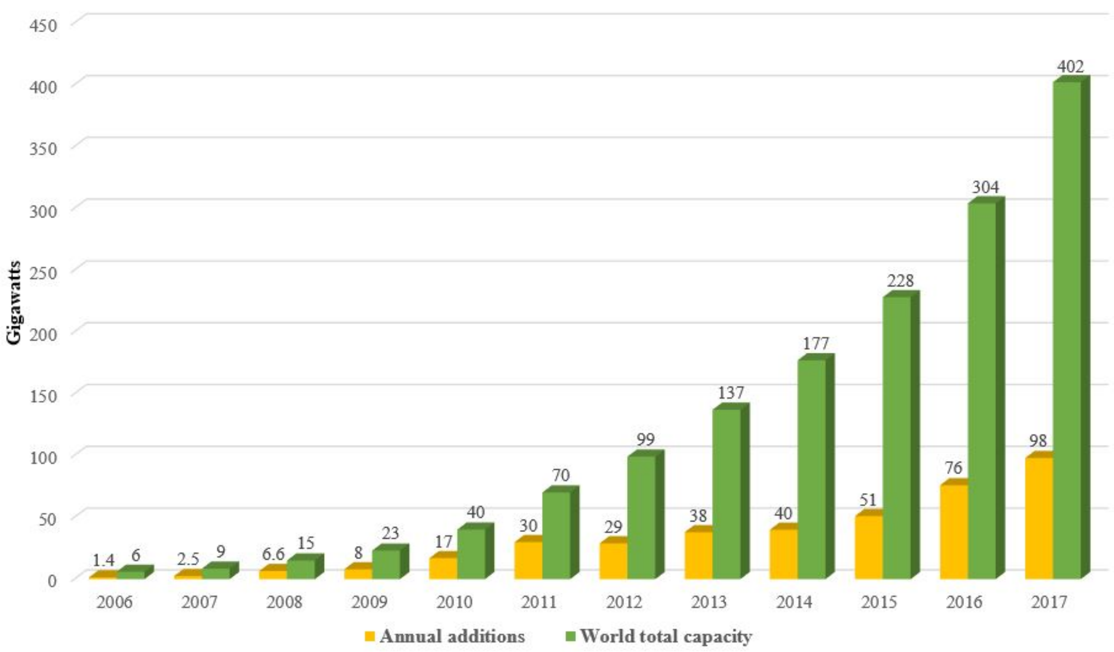

Fig. 1.1 : Solar energy capacity all over the world [85].

issues [17]. Generating electricity from renewable energy sources has increased dramatically in recent years, and it has been the fastest growing source of energy because it is abundant in nature, efficient and environmentally friendly [19]. The total electricity generated from renewable energy increases by 2.9% every year. Renewable energy generated about 22% of the world electricity in 2012. It is expected that this will increase to approximately 29% by 2040 [79]. Among the renewable energy sources, solar energy is one of the fastest growing forms of renewable energy sources due to its low price, long life span, low maintenance and easy installation. As shown in Fig. 1.1, during 2017, approximately 98 GW of solar power capacity was added, an amount equivalent to installing 40,000 solar panels every hour a year [85].

1.2 Background of Solar Energy Generator

The photovoltaic (PV) power system is widely accepted nowadays due to its clean, quiet and durable features. A solar cell or photovoltaic (PV) cell is a semiconductor electrical device used to convert solar radiation energy to electrical energy by the photovoltaic effect [108]. In the PV cell, the positive P-type layer and the negative N-type layer are joined together to form a “PN-junction”, and once it is exposed to the solar radiation, the electrons start moving and generating direct current (DC) as shown in Fig. 1.2.

In order to harvest the maximum power from the solar system, there is a need to study its main component’s behaviour and characteristic, which is the solar cell. For each solar cell, the relation between the voltage and current can be presented by the I-V and P-V curve. These two curves are nonlinear, as shown in Fig. 1.3. The P-V curve represents the relation between the power and voltage for the I-V curve by multiplying the voltage by the current for each point. The I-V curve looks

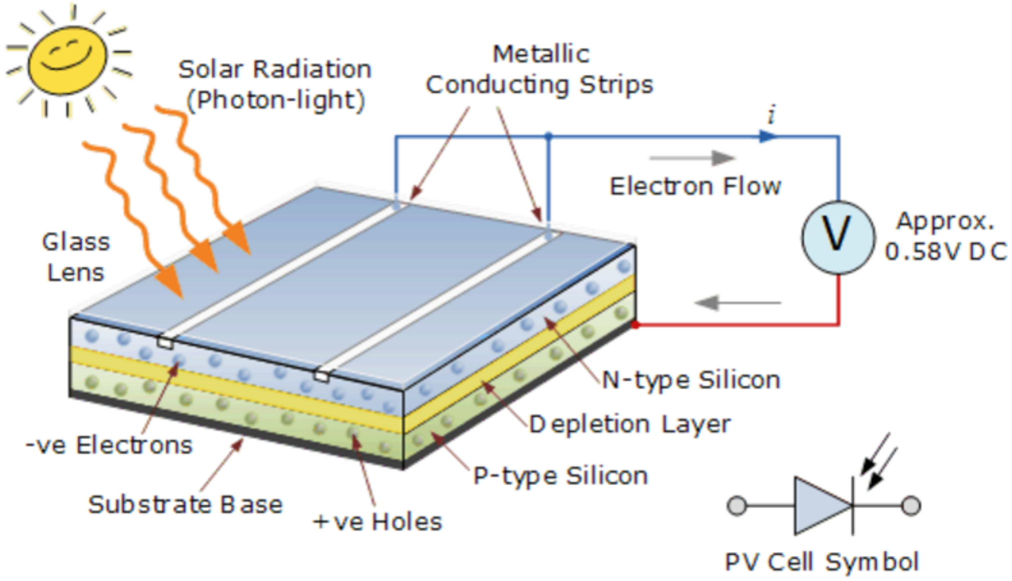

Fig. 1.2 : PV cell structure [48].

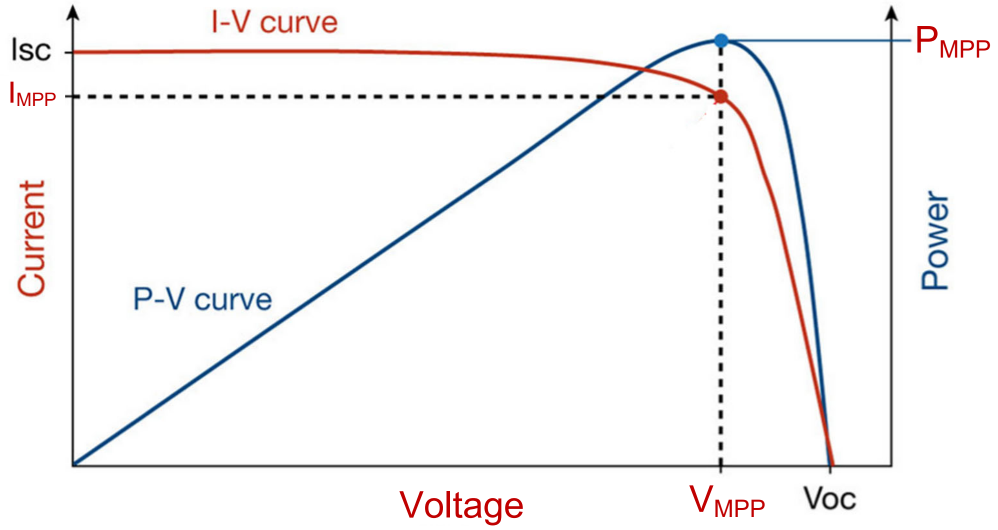

Fig. 1.3 : I-V and P-V curve for PV cell.

similar to the I-V diode curve, but it is inverted because the output current of the solar cell is complimentary to the diode and the shunt resistor current, according to the mathematical model of the solar cell, [27, 74]. The x-axis represents the voltage of the PV cell for both curves, and its value ranges between zero, if there is no solar radiation, to the open circuit voltage V_{oc} of the solar cell. For the I-V curve, the y-axis represents the current of the solar cell, and its value ranges between zero to the short-circuit current I_{SC} for the given cell. The y-axis for the P-V curve represents the generated power, and its value ranges between zero to the maximum power P_{MPP}.

The amount of energy that is harvested from one solar cell is too small. Therefore, some of the cells with identical characteristics should be connected together as a string to form a solar module or panel. The number of cells in each module varies, and it depends on the desired output voltage and power. If more than one module are connected in series, they will form a string. If the strings are connected in parallel, then they will be called a solar array [123]. Fig. 1.4 illustrates the difference between the cell, module, string and array.

The solar system can be grid-connected or a stand-alone power system [46, 119]. In the grid-connected photovoltaic power system, the PV generator system is connected with the utility grid through a power inverter and utility equipment. This power system comes in a small range as a residential rooftop system, or it might come in a large scale as a solar power plant. In the stand-alone power systems, the power generated from the PV generator system is used to feed the load in the rural areas where the utility grid is not available. The stand-alone power system is also useful for different applications, such as a solar vehicle, space, road and emergency signs, solar water pumps, meter reading, etc. Most of the time, the storage battery is used with stand-alone power systems.

1.3 Background of Power Converters

The power generated from the renewable energy source rapidly changes. The solar power can drop in seconds if the solar cell is exposed to shading, a phenomena

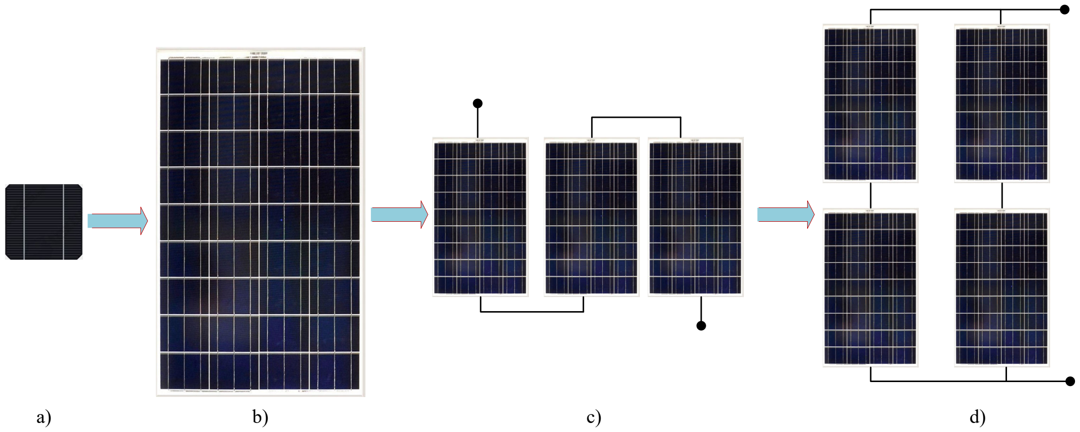

Fig. 1.4 : Solar system structures: a) Cell. b) Module/Panel (cells in series). c) String (modules in series). d) Array (Strings in parallel).

known as intermittency. Also, the efficiency of the photovoltaic panel is still low. It is reported in [98] that only 22.7% of the solar radiation can be converted to solar energy. Therefore, the maximum power point tracking (MPPT) algorithm is needed to get the most power possible from the PV sources. Power electronics converters are used to interface the renewable energy sources, a storage element and load [111]. Typically, the DC-DC power converter is used to track the maximum power point (MPPT), regulate the DC bus voltage and manage the power flow between the ports.

The size and design of the power converters are varied depending on the solar system size and its architecture. The solar system can be formed in the following main architectures [123]:

- Centralized DC/AC inverter structure.
- String DC/AC inverter structure.
- Multi-string inverter structures that can be arranged as:
    - ∗ Centralized DC/AC inverter with centralized DC/DC converter structure.
    - ∗ Centralized DC/AC inverter with string DC/DC converter structure.
    - ∗ Centralized DC/AC inverter with string DC/DC optimizer structure.
- Detached microinverter or the AC module structure.

Fig. 1.5(a) shows the centralized DC/AC inverter structure. The PV modules are series-connected into a string to obtain a high voltage. Then, multi-strings are parallel connected into an array. A blocking diode is needed for each string to prevent the current flowing between the strings. The centralized DC/AC inverter links the array with the DC bus. In this structure, there is no need for a DC/DC converter. Thus, the inverter is responsible for MPPT and grid regulation at the same time. In this configuration, a high voltage inverter is needed. This structure is used for

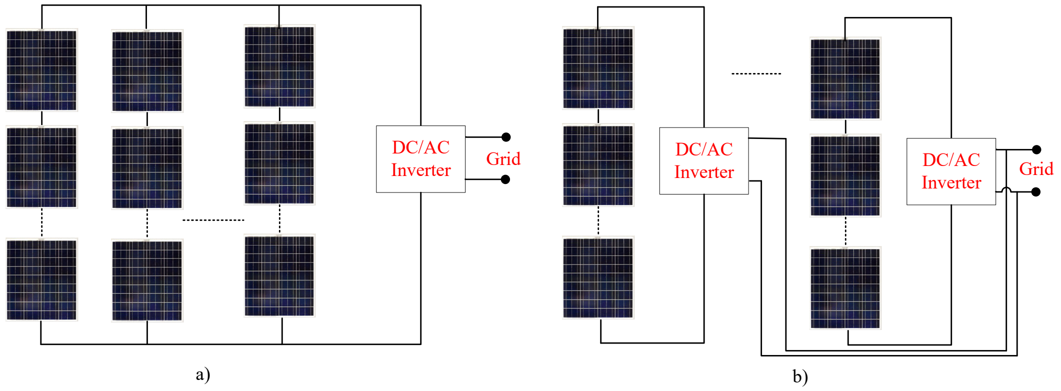

Fig. 1.5 : Solar system architecture: a) Centralized DC/AC inverter. b) String DC/AC inverter.

utility-scale PV power plants up to 1MW. The string DC/AC inverter structure, Fig. 1.5(b), is similar to the centralized DC/AC inverter structure. However, the PV panels are series connected into a string, and the inverter needs to handle the MPPT and voltage regulation at the string level. This structure is used for residential applications in which the typical power capacity is from 1 kW to 10 kW [65]. There are some limitations for the two mentioned structures, such as power loss during partial shading due to using one centralized MPPT for all panels, mismatch loss between the PV modules, and losses in the string diode [1].

The centralized DC/AC inverter with centralized DC/DC converter structure [40], Fig. 1.6(a), and centralized DC/AC inverter with string DC/DC converter structure [20], Fig. 1.6(b), are the modified version to the centralized DC/AC inverter structure and string DC/AC inverter structure, respectively. Nevertheless, a DC/DC converter is cascaded with the inverter. In these two structures, the DC/DC converter is responsible for MPPT, and the inverter is responsible for the grid regulation requirements. As a result, more control freedom is achieved.

The centralized DC/AC inverter with string DC/DC optimizer structure is similar

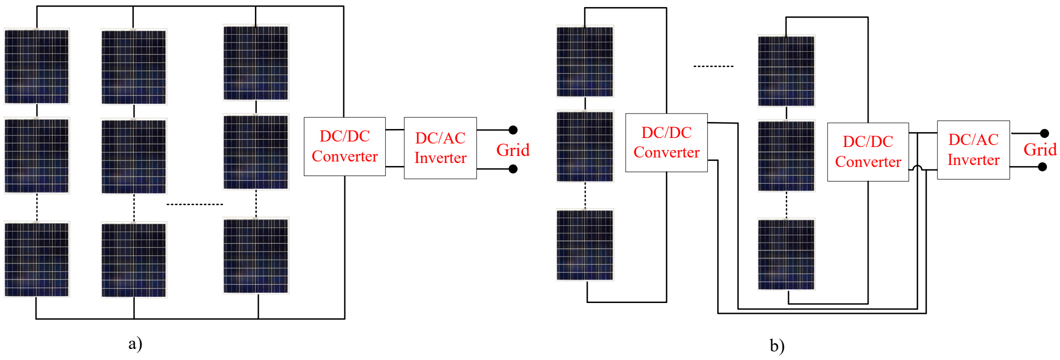

Fig. 1.6 : Solar system architecture: a) Centralized DC/AC inverter with centralized DC/DC converter. b) Centralized DC/AC inverter with string DC/DC converter.

to the centralized DC/AC inverter structure [60]. However, a DC/DC converter is integrated into each PV module, as shown in Fig. 1.7(a). The optimizer is able to achieve the MPPT into a PV module level. Thus, the significant power losses that may happen when mismatch or shading occurs is eliminated. In the grid microinverter (detached microinverter), Fig. 1.7(b), a small inverter is integrated into the PV module similar to the optimizer in the previous structure. The PV panel in this structure could be parallel connected to the grid, or it may be stand-alone for low power applications. Nevertheless, there is no need for a central inverter, and the PV modules are not required to be identical. Other advantages for this structure is that any failures in the PV panel will not affect other panels in the same system [18], and a battery storage element can be integrated into a PV panel if a multi-port converter is used. The integrated inverter structure helps to facilitate plug-and-play.

Due to the intermittent nature of the renewable energy, the power generated from the solar system is not able to supply the instantaneous demand. The power converters are used to track the MPP to support the maximum power possible to

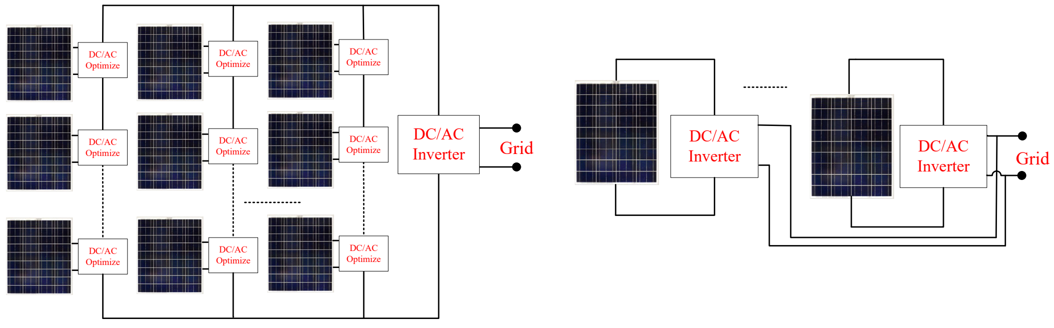

a)

b)

Fig. 1.7 : Solar system architecture: a) Centralized DC/AC inverter with string DC/DC optimizer. b) Grid microinverter.

the load. Even with a highly efficient maximum power point tracker, the converter will not be able to supply the load if the solar energy is not sufficient. An energy storage system (ESS) or supercapacitor (SC) are required to continuously supply power to the load and improve the reliability of the overall system [16]. In this case, more than one converter is required to manage the power flow between the solar panel, battery and load, causing more power losses and bigger system structure. In recent years, designing a multiport converter (MPC) and managing the power flow between the ports became very attractive because the compact structure of MPC reduces the cost and the mass of the system by sharing some components such as switches, capacitors and inductors. It also increases the power density and system reliability. Moreover, MPC uses central control, so less communication channels are required compared to the traditional two-port units. Thus, no communication delays or errors are caused [83, 97].

1.4 Outline

An overview of the PV system and its required power converters are stated in the previous sections. According to the literature survey, there is a space to improve the power quality and reliability of the solar system, either by harvesting the maximum power from the solar system or by utilizing the energy storage system. The organization of this thesis is listed as follows:

In Chapter 2, static and dynamic behaviours of cracked PV panels have studied to evaluate the impact of the crack on the cell, string and system level. The failure mechanism of independent PV string and its effects, potential risks and criticality are experimentally studied. The dynamic behaviour of the solar cell and its mathematical equations are carefully derived. A novel technique to detect the cracked cell has proposed, and experimental studies are carried out. Finally, the effect of the cracked cell has been examined on the system level by comparing the generated output power from parallel and series-connected solar panels, and the generated output power from the cracked panel. The generated output power is compared as well to the output power generated from the partially shaded panel with and without bypass diode.

In Chapter 3, a simple and cost-effective analog BJT-tuned voltage reference maximum power point tracking (MPPT) method for photovoltaic (PV) modules is proposed. In this chapter, MPPT algorithms are reviewed, then the proposed analog MPPT circuit with an improved tracking accuracy for PV modules are experimentally verified. The algorithm is voltage-based, and it uses a BJT-tuned circuit to better model and track the I-V characteristics of the PV module.

In Chapter 4, a literature review for the multi-port converter is presented. The literature review includes isolated, non-isolated and partly- isolated converters. In this chapter, a comparison between these converters is presented in order to select the suitable topology to integrate the PV with energy storage system (ESS).

In Chapter 5, a new non-isolated three-port DC-DC converter (NITPC), to integrate a battery storage with a PV module is proposed. In addition to the traditional MPC advantages, the proposed design has many other advantages, such as harvesting a maximum power from the renewable energy source by achieving maximum power point tracking (MPPT) and boosting the output voltage to a high voltage level by cascading the PV module, battery and coupled inductor. Other advantages of the proposed circuit include using one-stage conversion, less component voltage stress and low operation duty ratio. Moreover, the converter continually supplies the load and regulates the output voltage by managing the power flow between the ports at any time during day-time, even under changing weather, partial shading and unpredictable output demand for standalone PV system. The converter, in fact, is able to supply the load and regulate the output voltage during night-time.

In Chapter 6, a new high step-up non-isolated three-port DC-DC converter (HS-NITPC) is proposed. The converter is designed to integrate a solar panel with battery storage in order to boost its voltage, reduce the effect of solar energy intermittency and enhance the solar power performance under unpredictable load demand. The converter combines three converters to form one integrated converter by sharing some components. Thus, the converter has a high power density and fewer components compared to the traditional DC-DC converters. The coupled inductor is used to achieve a high output regulated voltage, transfer energy among the ports and facilitate maximum power point tracking for the solar panel. A hardware prototype was built and tested to verify the proposed circuit at 180 W input power. The proposed converter is suitable for stand-alone or grid-connected solar system. Moreover, it could be used in the electric vehicle where regenerative braking is used.

Finally, a conclusion summary and suggestions for future works are presented in Chapter 7.

Chapter 2

Static and Dynamic Behaviours of Cracked PV Panels

2.1 Overview

2.1.1 Literature Review

Shaded and cracked solar cells have a significant effect on the power generated from the solar system. The reason behind this effect is that during normal operational conditions, all solar cells have similar characteristics and performances, and they operate at forward-biased. Therefore, the current will flow smoothly. On the other hand, the cracked and shaded cells may cause electrical isolation and discontinuity due to operating at reverse-biased. As a result, the cracked and shaded cells will have a different operating point compared to the normal cells, and this will cause a power mismatch which produces hot spots that may damage the panel or lead to melting of solder joints.

By referring to Fig. 2.1(b), the maximum power point of a normal PV cell is at the top line (blue line). However, when the cell is cracked or shaded, the operating point will drop to the lower line (red line). To reduce the effect of this phenomenon, bypass diodes are connected in parallel in opposite polarity with each solar module as shown in the Fig. 2.1(a), or it may be connected with the string for some PV panels. This bypass diode will normally improve the system efficiency and reliability [84]. When cells are unshaded and uncracked, each solar cell is forward biased. As a result, the bypass diode will be reversed-biased. In other words, the bypass diode will act as an open circuit, and all of the PV cells will have the same

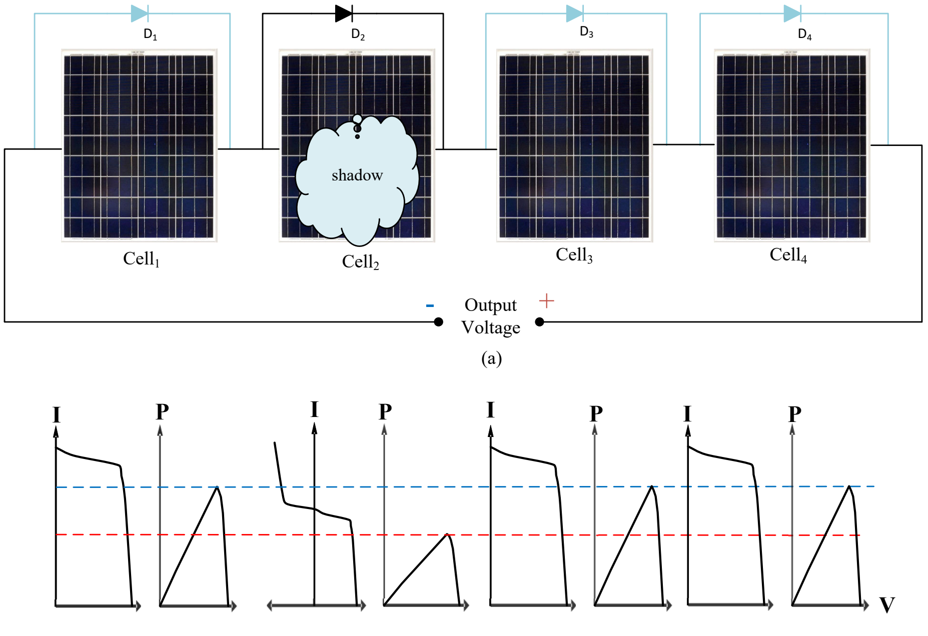

(a)

(b)

Fig. 2.1 : a) String PV modules in series with bypass diode. b) I-V and P-V curves of normal panels and one panel with some cells cracked or shaded.

characteristics and P-V shape. When the cells are cracked and shaded, the solar cell becomes reverse biased; and consequently the bypass diode will conduct, acting as a short circuit. As a result, the current will not flow through the shaded or cracked cell [94].

PV panels are considered relatively as reliable components with long service life if compared to its interfaced power electronics circuits. Moreover, most of the manufacturers provide a considerably long term output power warranty, which guarantees within the warranty period that the output power of the solar panel would be no less than 80% of minimum ‘Peak Power Standard Test Conditions’. For example, Sharp Mono solar panel: NURC300 has a product warranty of 10 years and linear performance of 25 years [91], and all solar panels from Solar Technology

International Ltd have 20 year cell warranty and 10 year module warranty [69], etc. However, some recent work claims that large power losses are induced by micro-cracks, which significantly reduce the power efficiency of the panel and shorten its lifespan [32]. The conclusion is obtained from 10 PV panels (Panel Model: Romag SMT6 (60)P PV Modules with 25-year power output warranty) for a 7-year operation at the University of Huddersfield, United Kingdom [33]. The measured efficiencies of the two degraded panels with defects are 80.73% and 85.43% while the efficiencies of other normal panels are between 97% - 99%. The panel with efficiency at 80.73% indicates that it is approaching its end of life, which is much shorter than the expected long lifespan.

Based on this concern, the micro-cracks failure mechanisms are reviewed [32, 62, 61, 49, 41, 36]. The cracks are most likely generated during the manufacturing, transportation and installation stages. Furthermore, the mechanical stress such as snow loads could increase the possibility of developing a large crack [62]. Kontges states that the direct impact of the micro-cracks on the solar panel is limited, and no losses occur when the separation area, due to micro-cracks, is under 8% [61]. However, if the inactive area continuously grows with the cracks to around 12%-50%, the power losses increase almost linearly.

Load tests were conducted in [49] and [41], which were aimed at evaluating the criticality of different types of cracks and predicting the losses caused by them and their propagation, respectively. A high criticality is considered if the crack has a high possibility to form an electrical isolated area of 16%-24% [49]. Results in [41] indicate that cracks do not necessarily cause permanent electrical isolation. Losing the electrical connection can be observed when the cell is under mechanical stress. The connections, however, may be recovered after the stress is removed. Both the results by [49] and [41], indicate that the cracks that are in parallel to the busbar are the most critical ones, among several types of cracks, which not only a have high probability to form an electrical disconnection, but also have high degradation percentages. In [36], an investigation of the impact of the snail trail phenomenon and the micro-cracks on the solar panels is presented. The study concludes that the micro-cracks play a significant role in the degradation of the solar panel performance. The decayed panel performs at a lower maximum power point than the value indicated in the datasheet due to reduced generation current.

2.1.2 Research Gap/Problem

The aforementioned research reviewed the failure mechanism, detrimental effects, criticality, and potential risks of cracks on PV panels. The evaluations in most of the above work are conducted through using the I-V and P-V curves to indicate the output power generation capability, which is the static behaviour of PV panels. Using an impedance spectroscopy is an alternative method to evaluate the crack effect [24, 57, 56, 51], which reflects the dynamic behaviour of a cracked PV panel. In [24], the dynamic impedance of a PV module is derived and verified which shows dependency on bias voltage and frequency. In [57], a comprehensive PV cell model is proposed, and the cell under reverse biased condition is analyzed particularly by measuring both I-V curve and impedance. It is found that the partially shaded or faulty cell becomes reverse biased and forms a hot-spot which will degrade the cell performance. In [56], a method which uses dynamic impedance of a PV string to detect hot spots is proposed. Changes of high frequency AC capacitance and low frequency DC resistance are compared. In [51], impedance spectroscopy is used to detect faulty and degraded PV cells, such as mechanical stress and PV cells with interconnect ribbon disconnection. The Nyquist plots then compare with the measured I-V curve.

Inspired by the studies above, the impacts of cracks appeared on PVs are firstly studied to get a better understanding of their failure mechanism, detrimental effects, criticality and potential risks. In this study, the most common cracked cells are mimicked by six crack scenarios; then, their effects have been reported. Secondly, investigations not only from the static, but also from the dynamic side, to analyze the relationship between the crack severity. The change of operation point in P-V curve and also of the impedance are presented. Thirdly, an online technique to track the cracked cells has been proposed by investigating the ac parameter of the solar cell in the dynamic regime. The proposed technique can examine the cracked cell by injecting a sinusoidal AC signal and monitoring its voltage and current to measure the phase shift. Finally, the extent to which the cracked cells act on the degraded performance of the PV panels has been studied. Thus, experiments focusing on evaluating the output power performances of PV panel which include cracked cells are conducted. In addition, the power performance of identical PV panels, some of which are seriously cracked is presented for a different panel configuration with and without a bypass diode.

This chapter is organized as follows: In Section 2.2, the cracked cells are reviewed, and their impacts are analyzed. In Section 2.3, the solar mathematical module is discussed, and its equations are derived. In Section 2.4, the proposed cracked solar cells tracking technique is discussed and experimentally verified. In Section 2.5, the experiment is conducted to evaluate the performance of PV strings with different connection methods, followed by the conclusion in Section 2.6.

2.2 Review of Impacts of Different Crack Types on PV Panel Output Performances

Firstly, the static behaviour of the PV panel is reviewed in this section, and a series of experimental works are conducted to investigate the impacts of different crack types on their corresponding output performances. The measurements are implemented in the laboratory where the ambient temperature is set to 25°C. A

60W solar panel which has 36 cells (Panel Model: Megavolt Solar MS-M60) is used. The panel is reconfigured to form four independent strings, with each string having nine cells in series. Due to the fact that cracks are formed and aggravated through a long operation period, and not all crack types have significant impacts on the PV panel power generation capacity, artificial cracks are made in this experiment to mimic those serious decayed cracks. Two halogen lamps are used to simulate the solar radiation. Six cases are analyzed to study the effects of different types of cracked cell on the output power of the strings. The enlarged photos of a normal cell and different cracked cells are shown in Fig. 2.2. The scenarios are listed as below:

- One string with no cracks (Fig. 2.2(a)): this string generates I-V and P-V curves under normal working condition, and it is used as a reference.
- One string with one cell horizontally cracked (Fig. 2.2(b)): one cell in the second string has a hairline cut, and this cut is perpendicular to the busbar.
- One string with one cell diagonally cracked between busbar (Fig. 2.2(c)): one cell in the third string is cut between the busbar, and it has a 45° angle.
- One string with one cell cracked diagonally outside the busbar (Fig. 2.2(d)): this cut is similar to the previous cut, but outside the busbar (the cell effective area is reduced by 0.25%).
- One string with one cell partially cracked between busbars (Fig. 2.2(e)): in this case, two cuts, which are parallel and close to the busbar are made. Although the cell is not fully isolated to the busbar, about half of the cell area is eliminated.
- One string with one cell totally cracked (Fig. 2.2(f)): this cut is similar to the partially cracked between busbars. However, two more cuts are made to eliminate the whole cell from the string.

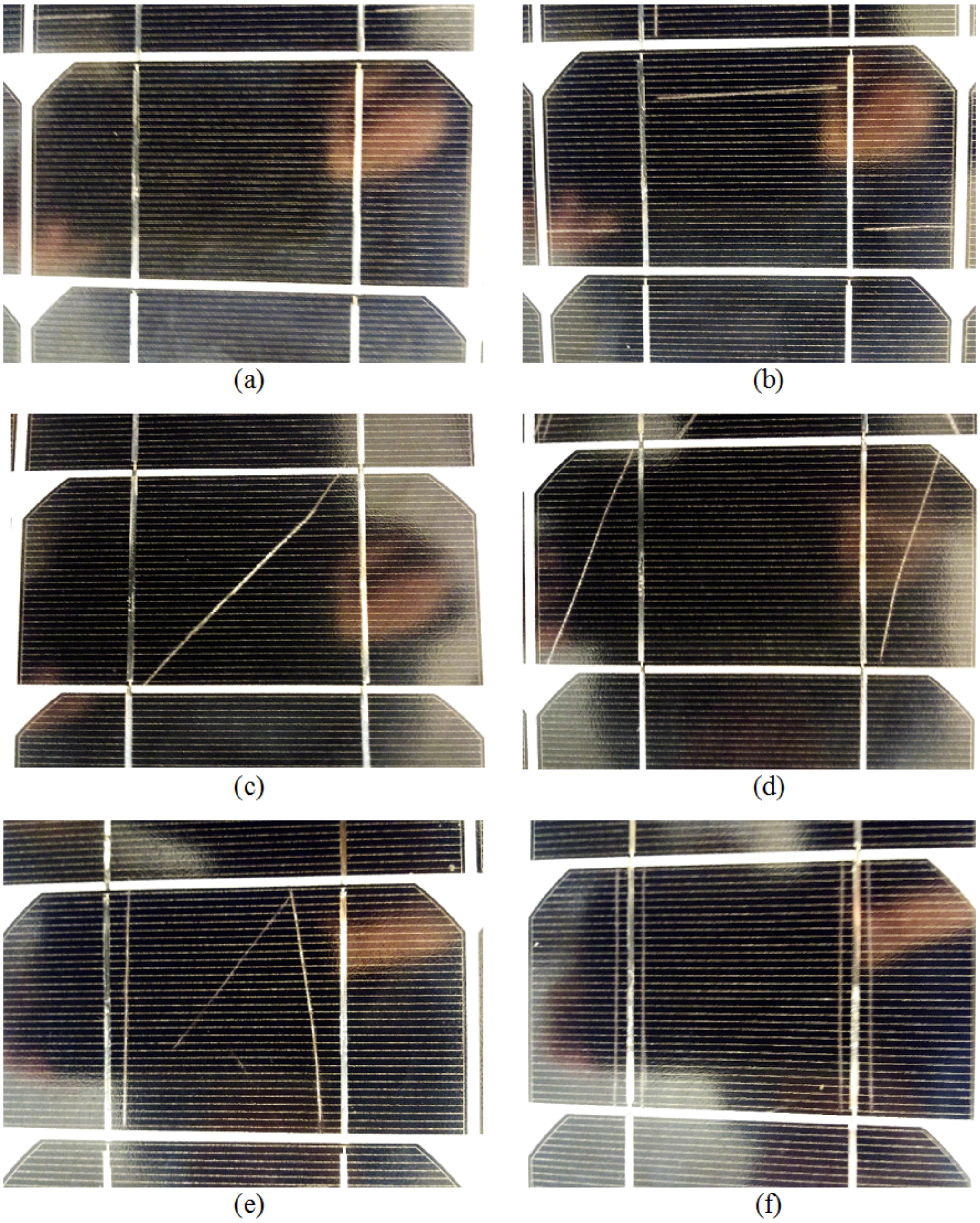

Fig. 2.2 : Enlarged looks of a normal cell and five cracked cells in different PV strings: (a) No cracks. (b) The horizontally cracked cell. (c) The diagonally cracked cell between busbar. (d) The diagonally cracked cell outside busbar. (e) The partially cracked cell between busbar. (f) The totally cracked cell.

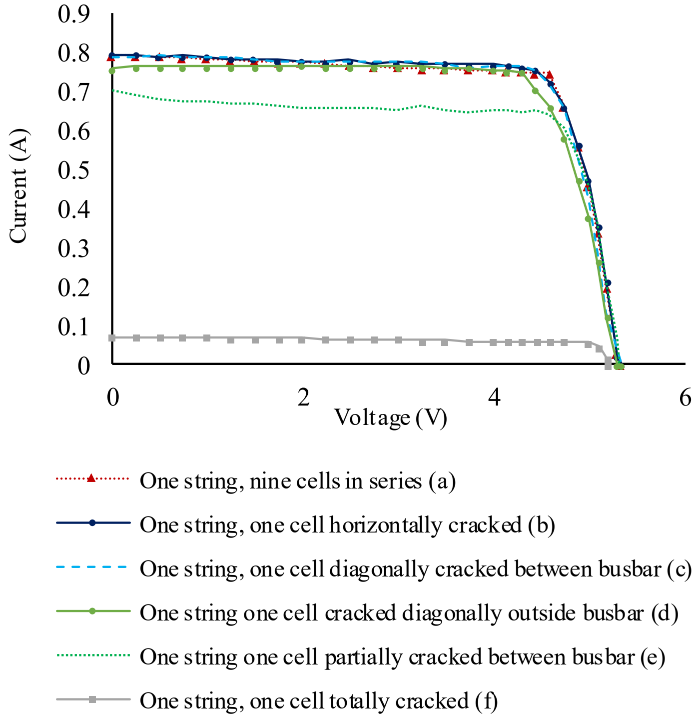

Fig. 2.3 : I-V curves of six different PV strings.

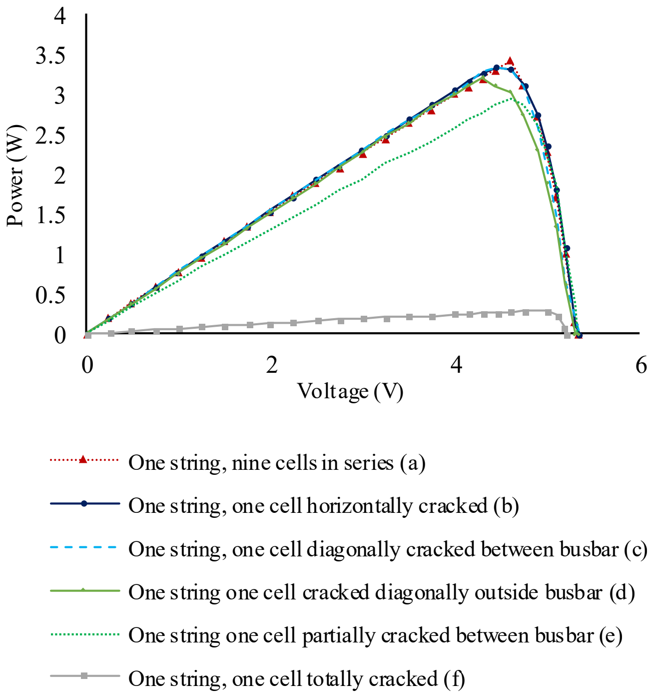

Fig. 2.4 : P-V curves of six different PV strings.

The measured I-V and P-V curves of these six cases are plotted in Figs. 2.3 and 2.4 respectively. As can be seen, the worst scenario happens when a cell is totally cracked, followed by a cell that is partially cracked. The completely cracked cell means the cell loses the electrical connection to the busbar while the partially cracked cell has limited effective area to generate current. Both of these cases show a reduced current of the entire PV string. That is because of the structure of the solar cell. The cell basically is a P-N junction, and the front layer is a negative layer while the back layer is a positive one. In order to link PV cells in series, connections are made by connecting the top layer of the first cell to the bottom layer of the second cell, as shown in Fig. 2.5. The current flows between the two layers, hence, any cells with serious cracks will affect the entire current path. Moreover, the temperature in each case is monitored, to study the potential risk of hot spots caused by cracks.

Table 2.1 provides a summary of the maximum power, virtual power (the short circuit current multiplied by the open circuit voltage), fill factor (FF), normalized efficiency, and temperature of these six cases. The FF is the most important parameter that defines the quality of a PV panel. The FF value can be calculated by

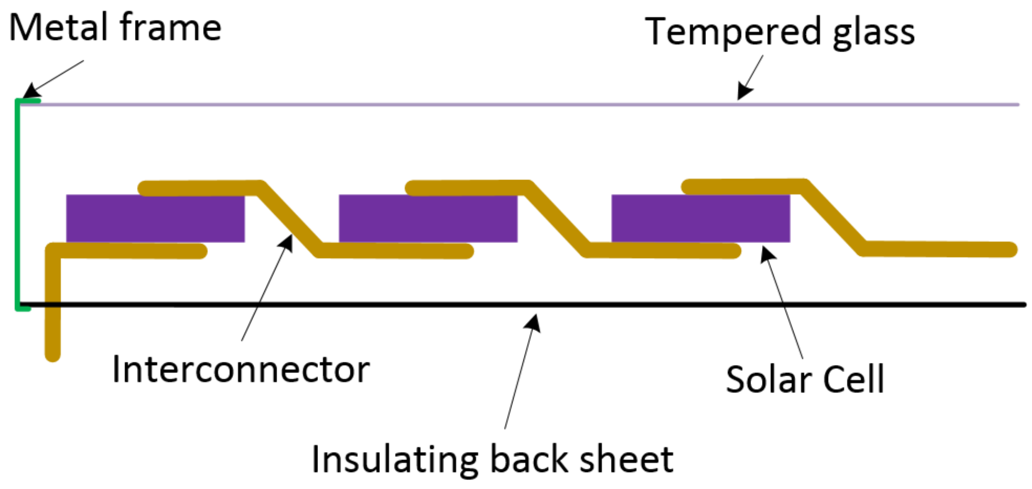

Fig. 2.5 : PV cell physical structure.

Table 2.1 : A Summary of Maximum Power, Virtual Power, Fill Factor, Efficiency and Temperature of Six Different Crack Types

Case Study(1 String with 9 Cells in series)	Maximum Power	virtual Power (I_{short}*V_{open})	Fill Factor	Normalized Efficiency	Temperature (°C)
Normal String, no cracks	3.410	4.216	0.8089	1	27
1 cell horizontally cracked	3.343	4.221	0.7920	0.98034	29
1 cell diagonally cracked between busbars	3.338	4.195	0.7959	0.97891	29
1 cell cracked diagonally outside busbar	3.209	4.043	0.7937	0.94093	30
1 cell partially cracked between busbar	2.942	3.722	0.7904	0.86272	31
1 cell totally cracked	0.279	0.364	0.7677	0.08194	34

finding the ratio of maximum power over the virtual power which is used to define the quality of a PV panel as described in (2.1).

$$FF = \frac{P_{mpp}}{I_{sc}V_{oc}} \tag{2.1}$$

where P_m is the maximum power and I_{sc} short circuit current and V_{op} is the open circuit voltage.

Higher FF value implies higher solar cell quality [62]. The results have shown that, with the increasing of seriousness of a cracked cell in a PV string, the string quality, maximum power generate capability and efficiency are reduced accordingly. The room temperature is set to 25°C, and the PV panel is cooled down before doing the next experiment. The temperature increases possibly due to the halogen lamps in the first case, and with the increasing level of cracks, the temperature rises accordingly. Case 6 shows the string increases to 34°C and the two neighboring cells increase to 31°C, which possibly can be developed to a hot spot.

2.3 Dynamic Photovoltaic Modeling

The single-diode module [43, 11, 12, 93, 34, 10, 75, 73], as shown in Fig. 2.6(a), is the most commonly used method to find the equivalent circuit of a PV cell. In most cases, the PV cells, which are arranged in an array form, are connected to switch-mode power converters to either track the maximum power point or regulate the output voltage. These power converters increase the harmonics penetration due to their switching frequency. The appeared ripple causes some dynamic characteristic for the solar cells; therefore, the single-diode module becomes less accurate [13]. The PV cell is in fact a p-n junction semiconductor with parasitic resistances, capacitance, and inductance. The large-signal model is more useful to study the behaviour of the PV cell as the charge storage at the junction is considered under the power mismatch that can be caused by the partial shading, aging, degradation and cell microcracks [57, 100, 110]. The large-signal model shown in Fig. 2.6(b) consists of a current source where the light-generated current I_{ph} is directly proportional to the solar irradiance, a forward biased diode D_f, a shunt resistance R_{sh}, a series resistance R_s and a parallel capacitance C_p. The light-generated current I_{ph} is given as

$$I_{ph}(G,T) = [I_{sc,n} + K_i(T - T_n)]\frac{G}{G_n} \tag{2.2}$$

where the $I_{sc,n}$ is the short-circuit light-generated current at the nominal condition (standard testing condition usually 25 °C and 1000 W/m^2), K_i is the temperature coefficient of the short circuit current, T is the tested temperature, G is the tested irradiance and T_n & G_n are temperature & irradiance at nominal condition, respectively [108]. According to the diode equations the diode thermal voltage at different temperature is given as

$$V_t(T) = \frac{kT}{q}N_s \tag{2.3}$$

where k is Boltzmann's constant, q is an electron charge, and N_s is the number of series cells. The diode current is given as

$$I_d = I_0[exp(\frac{V_d}{nV_t}) - 1] = I_0[exp(\frac{V_{pv}+I_{pv}R_s}{nV_t}) - 1] \tag{2.4}$$

where I_0 is the diode reverse saturation current and α is the diode ideality factor that ranges from 1 to 2. According to Ohm's law, the current flows in the shunt resistor is given as

$$I_{sh} = \frac{V_d}{R_{sh}} = \frac{V_{pv} + I_{pv}R_s}{R_{sh}} \tag{2.5}$$

By considering the above equation the solar cell current is expressed as

$$\begin{gathered} I_{pv} = I_{ph} - I_d - I_{sh} \\ I_{pv} = I_{ph} - I_0[exp(\frac{V_{pv}+I_{pv}R_s}{nV_t}) - 1] - \frac{(V_{pv} + I_{pv}R_s)}{R_{sh}} \end{gathered} \tag{2.6}$$

The value of the parallel capacitor changes in accordance to different operating points of the solar cell as it is described in (2.7).

$$I_{C_p} = C_p\frac{dV_d}{dt} \tag{2.7}$$

According to the above study of the solar cell behaviour in the static regime and its derivative equations (2.2)-(2.7), it is notable that it is not possible to catch any change in the parasitic capacitance that can be caused by the solar cells again due to degradation. Therefore, the dynamic regime and associated ac parameters become very attractive in order to study and determine the behaviour of the solar cell. The AC small-signal of the equivalent large-signal model that is shown in Fig. 2.6(b) is depicted in Fig. 2.7, and its impedance Z is presented in (2.8). It is clear that the effect of the parallel capacitor C_p appears by studying the dynamic regime.

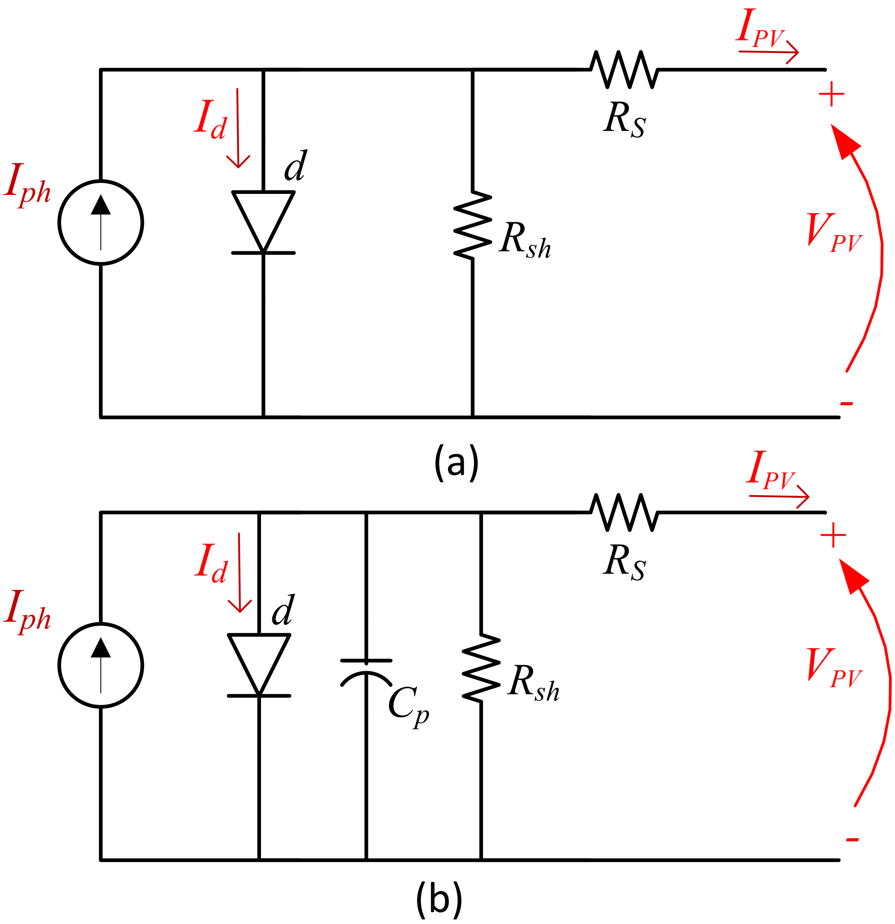

Fig. 2.6 : Equivalent circuit of solar PV module: a) single-diode module. b) large-signal model.

$$Z = [R_s + \frac{R_{sh}}{1+(\omega C_p R_{sh})^2}] - \jmath[\frac{\omega C_p R_{sh}^2}{1+(\omega C_p R_{sh})^2}] \tag{2.8}$$

The parallel capacitor C_p is the sum of the diffusion capacitance C_d and the transition capacitance C_t. In fact, these capacitances are nonlinear values depending on the operating point voltage [28]. According to [64,28], the transition capacitance C_t is caused by the separation of charges in the space charge region and is given by

$$C_t = \frac{b}{\sqrt{V_j - V_a}} = A\sqrt{\frac{Nq\epsilon_0\epsilon_r}{2(V_j - V_a)}} \tag{2.9}$$

where a constant b depends on the solar cell, V_j is the junction voltage, V_a is the applied voltage, A is the area of the solar cell, q is the elementary charge, ϵ_0 is the permittivity of free space, ϵ_r represents the relative permittivity of the solar cell material, and N_D and N_A are the doping concentration in cm^3 in the n and p regions, respectively. The value of the doping concentration, junction voltage and

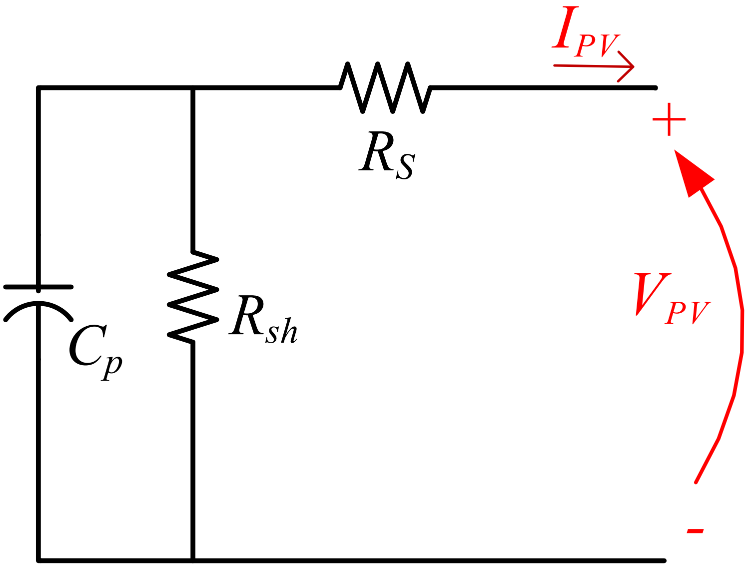

Fig. 2.7 : Ac small-signal solar cell model of Fig. 2.6(a).

constant b are defined as

$$\begin{aligned} N &= \frac{N_D N_A}{N_D + N_A} \\ V_j &= \frac{kT}{q} ln[\frac{N_D N_A}{N_i^2}] \\ b &= A\sqrt{\frac{Nq\epsilon_0\epsilon_r}{2}} \end{aligned} \tag{2.10}$$

where N_i is the intrinsic concentration of electrons & holes for the base semiconductor. The diffusion capacitance C_d is notable during forward biased of the p-n junction, and its value depends on the frequency and voltage according to [28].

$$C_d = \frac{\tau q}{2kT} I_0 exp(\frac{qV_a}{nkT}), \omega\tau << 1 \tag{2.11}$$

where τ is minority carrier lifetime. According to [104, 88, 2] the minority carrier lifetime is highly degraded by the solar cell aging during outdoor exposure. Thus, the electrical parameters of the solar cell are more likely to change with time. Accordingly, the cracked and aged solar cell creates a change in parallel capacitors value associated with the solar cell during the dynamic regime. This behaviour can be used to detect the cracked solar cell, and it can be achieved by operating the solar cell at a different frequency.

2.4 AC Small-signal to Investigate Cracked Cells

2.4.1 Experiment Setup

The PV modules show nonlinear parallel capacitance when they are connected to a high frequency power converters [57, 13]. In this experiment, the dynamic behaviour of the normal solar cell is investigated and compared with a cracked cell to prove that the crack and aging affect the solar cell parallel capacitor. Another objective for this experiment is to prove that cracks diagnosis of the PV cell can be carried out by investigating the dynamic performance of the PV cells while it is connected online, without the need for physical inspection of the solar panels. Fig.

2.8 shows a simplified connection diagram showing the equipment setup for testing dynamic behaviour of the solar panel with and without cracked cells.

In this experiment, three of the PV strings that is used in the first experiment are used with the same cracked arrangements namely; normal string with no cracks, string with one cell cracked between the busbar, and string with one cell totally cracked. A function generator is directly connected to the PV module where a sinusoidal signal at 1 V_{p-p} and the overall DC offset equals the voltage at the maximum power point at 4.7 V, and it is injected to the PV cells. An oscilloscope (Tektronix TBS2000) is used to capture the injected voltage waveform and the reflected current while the frequency of the sinusoidal signal is swept from 1 Hz to 1 MHz as shown in the actual equipment setup in Fig. 2.9. The solar panel was arranged in such a way so that it is not exposed to any radiation but responding only to the injected ac signal.

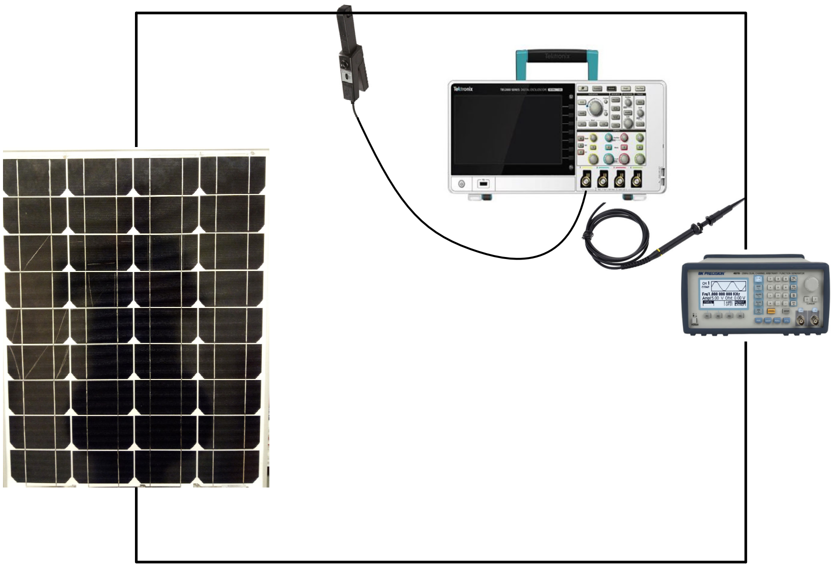

Fig. 2.8 : Simplified connection diagram showing the equipment setup for testing dynamic behaviour of the solar panel with and without cracked cells.

2.4.2 Experiment Results

The injected voltage and the reflected current waveforms are captured and analyzed while performing a frequency sweep. Fig. 2.10 shows the waveforms of the injected voltage and the reflected current for the string with normal cells and the string with one cell totally cracked at 100 kHz frequency. Results show that the current leads the voltage which implies that the equivalent circuit of the solar cell is no longer of purely resistive nature as it is derived in the single-diode module, particularly when it is connected to switching power converters. Nevertheless, the waveform implies that the equivalent circuit of the solar cell behaves as a capacitive circuit. According to the recorded waveform, the current leads the voltage by 27° for the normal string while it increases by 11.66° to become 38.66° for string with one cell totally cracked.

The solar cell impedance and the phase shift are calculated in order to obtain the Bode plot. The Bode plot for the three strings is presented in Fig. 2.11. It is clearly illustrated from the plot that the impedance increases for the PV strings with

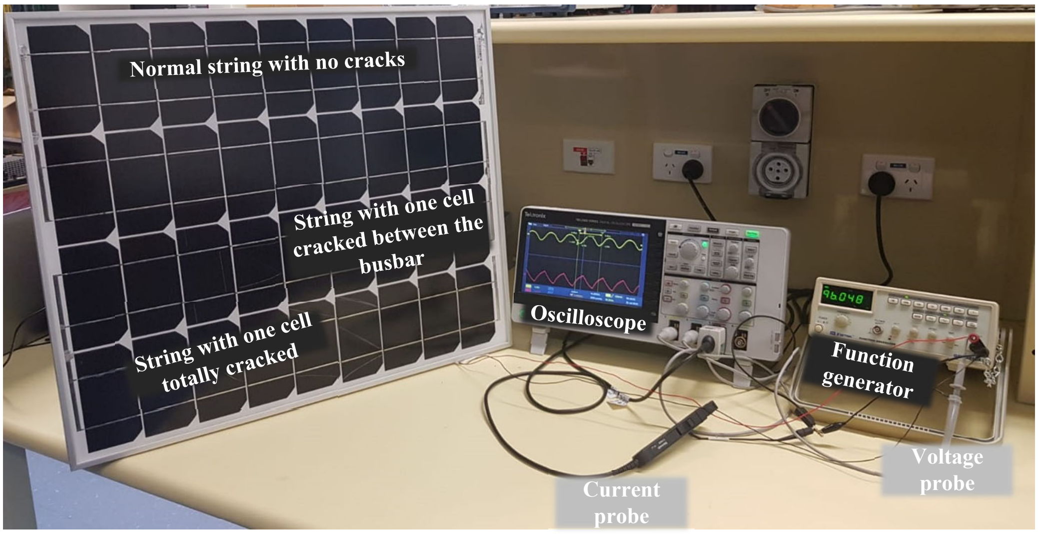

Fig. 2.9 : Experiment setup for testing dynamic behaviour of the solar panel with and without cracked cells.

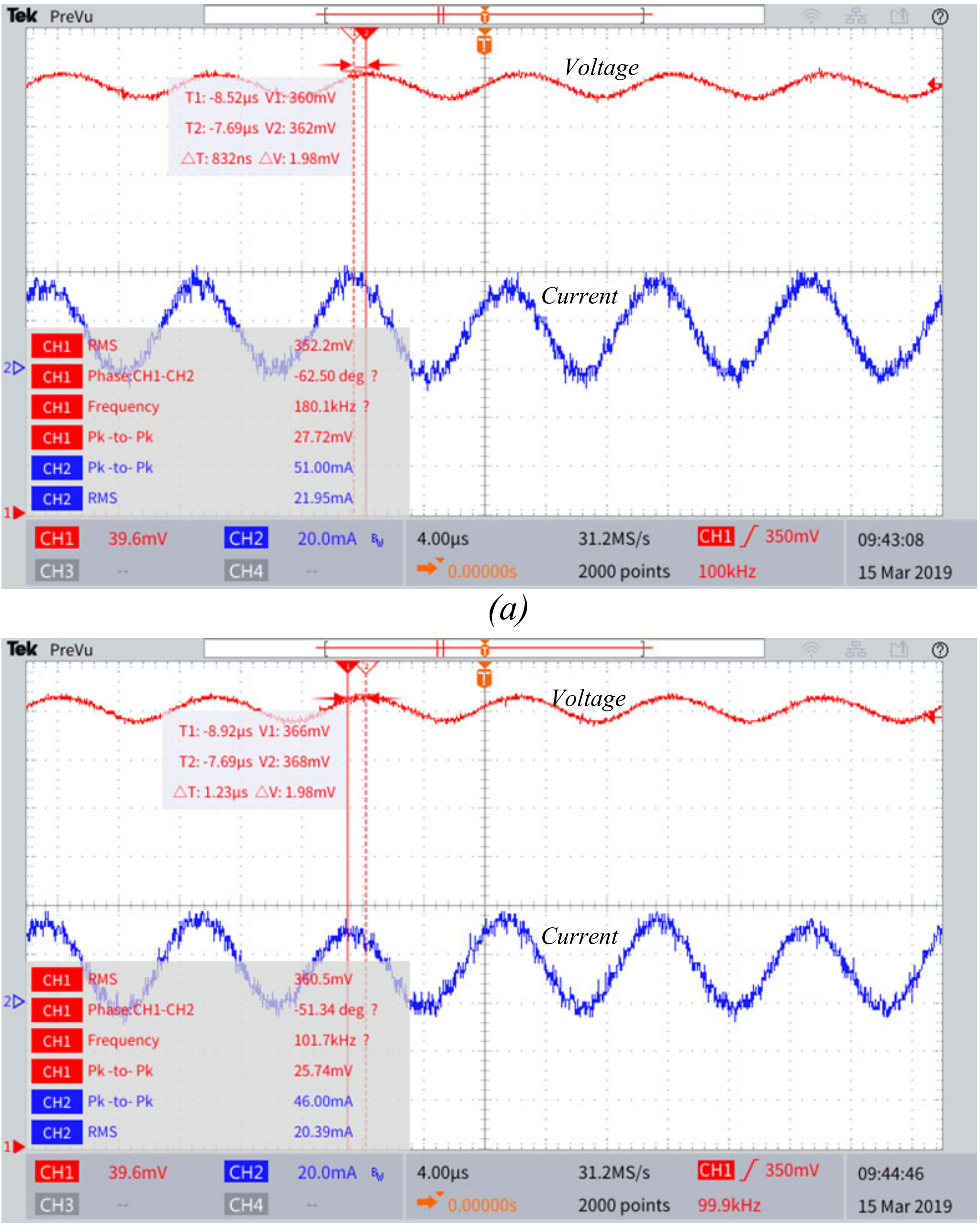

T1: -8.52µs V1: 360mV
T2: -7.69µs V2: 362mV
△T: 832ns △V: 1.98mV

CH1	RMS	352.2mV
CH1	Phase:CH1-CH2	-62.50 deg ?
CH1	Frequency	180.1kHz ?
CH1	Pk-to-Pk	27.72mV
CH2	Pk-to-Pk	51.00mA
CH2	RMS	21.95mA

CH1 39.6mV CH2 20.0mA 4.00µs 31.2MS/s CH1 ∕ 350mV 09:43:08
CH3 -- CH4 -- 0.00000s 2000 points 100kHz 15 Mar 2019

(a)

T1: -8.92µs V1: 366mV
T2: -7.69µs V2: 368mV
△T: 1.23µs △V: 1.98mV

CH1	RMS	360.5mV
CH1	Phase:CH1-CH2	-51.34 deg ?
CH1	Frequency	101.7kHz ?
CH1	Pk-to-Pk	25.74mV
CH2	Pk-to-Pk	46.00mA
CH2	RMS	20.39mA

CH1 39.6mV CH2 20.0mA 4.00µs 31.2MS/s CH1 ∕ 350mV 09:44:46
CH3 -- CH4 -- 0.00000s 2000 points 99.9kHz 15 Mar 2019

(b)

Fig. 2.10 : Waveform for the injected voltage and the reflected current: a) string with normal cells. b) string with one cell totally cracked, at 100 kHz frequency.

microcracks. This provides the evidence for the drop of the power generated from the PV string if there is at least one cell cracked. The phase response also shows a clear indicator for a cracked string at the resonant frequency (≈120kHz). For the other scenarios where the normalized efficiency of the strings is greater than 94%(Table 2.1), the cracked solar panel was demonstrated at small capacitive behaviour.

2.5 Performance Evaluation of PV Panel and System with Different Connection Methods

In order to investigate the effect of the cracks further, and to confirm that the cracks affect the behaviour of the solar cell regardless of its brand and manufacture, the previous experiments (Sections 2.2 and 2.4) have been reperformed by using a 20W solar panel with 36 cells (Panel Model: Powertech ZM9055). The experiment results show that the output power performance is similar to the one in the previous experiment. In addition to studying how the cracked cells affect individual PV string output power, the following experimental work investigates and compares the performance of three groups of experiments as described below:

- Evaluation of output performances of a normal PV panel, a panel with two cracked cells and a panel with two shaded cells.
- Investigation and comparison of performances among three different PV panel strings, namely, two normal PV panels connected in series, two PV panel connected in series with one panel is serious cracked, and two PV panels connected in series with one panel serious cracked and bypass diodes are used.
- Investigation and comparison of output performance between two PV panels connected in parallel and two PV panels connected in parallel with one panel

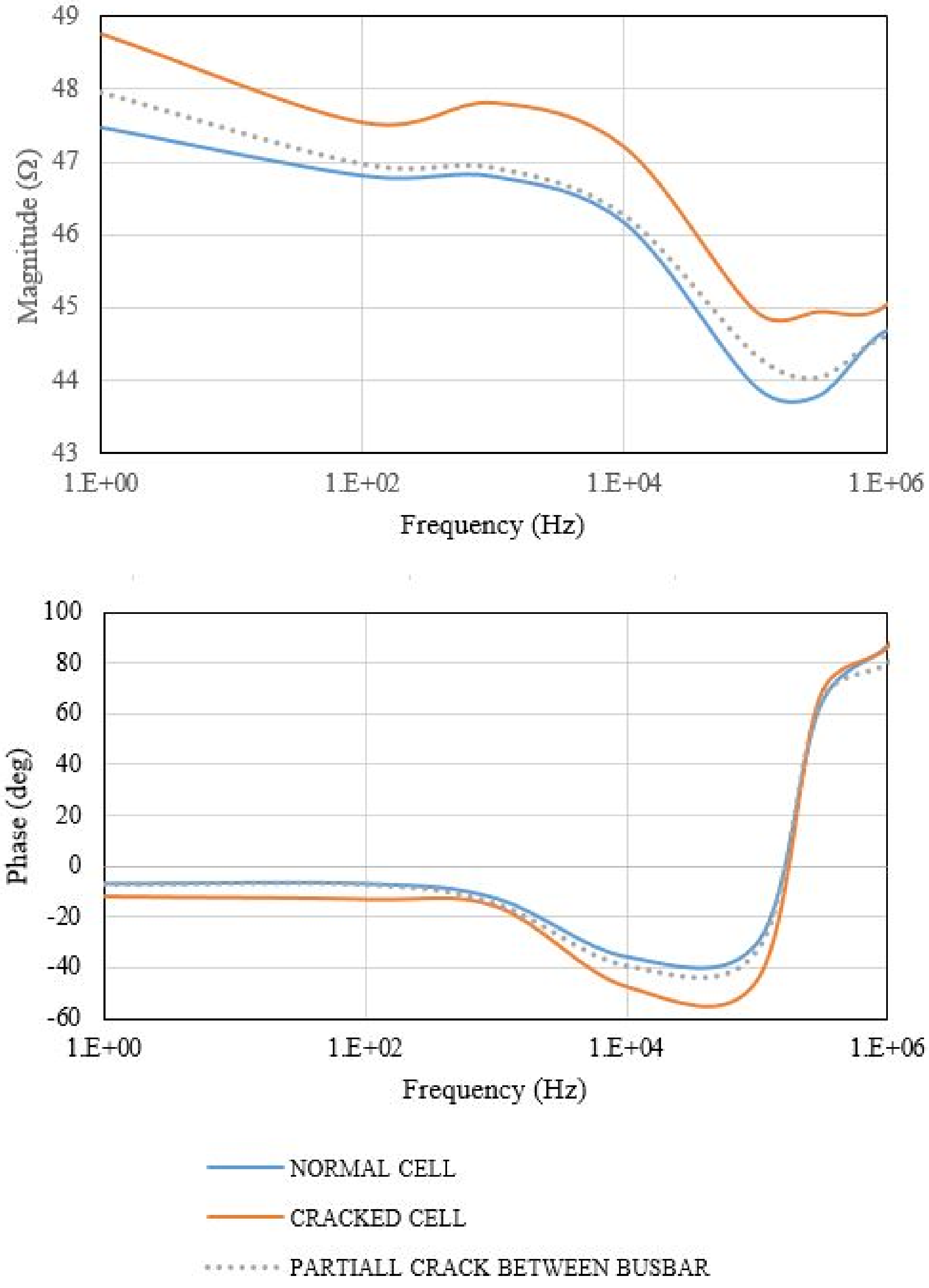

Fig. 2.11 : PV ac small-signal model bode plot.

having serious cracked cells. It is worth noting that the bypass diode which is adopted to mitigate the crack impacts is also studied and compared.

The experimental results of aforementioned three groups are shown in Figs. 2.12 to 2.14 respectively. As can be observed in Fig. 2.12, the detrimental impact of the cracks is more critical than the partial shading effect when the cells are seriously cracked. In Fig. 2.13, the results indicate that, the serious cracked panel clamps the current of the PV string, and hence, significantly reduces the generation power. In addition, the extra bypass diode can effectively mitigate this phenomenon. The results shown in Fig. 2.14 reveal that the operation of the normal panel is not affected by the cracked one in the parallel connected PV string, and the bypass diode is useless with the parallel connection. However, the overall power is still lower.

According to the previous investigation and study, the crack greatly affects the performers of the solar cell, and it gets greater when the cells form a string or a panel. When it comes to the solar system, one panel with a few cracked cells can drop the power generated by 90%. Even with bypass diode, the power can drop by 60%. Hence it presents an important need to track the cracked cells to improve the power quality of the solar system.

2.6 Summary

In this chapter, the failure mechanism, detrimental effects, criticality, and potential risks of cracks on independent PV strings are experimentally reviewed by studying the impacts of different crack types. The results verify that the loss of electrical connection between the PV cell and busbar would cause a great reduction of the entire PV string power generation capability. Moreover, a crack detection technique is proposed by studying the dynamic regime of the solar cell in addition to investigating

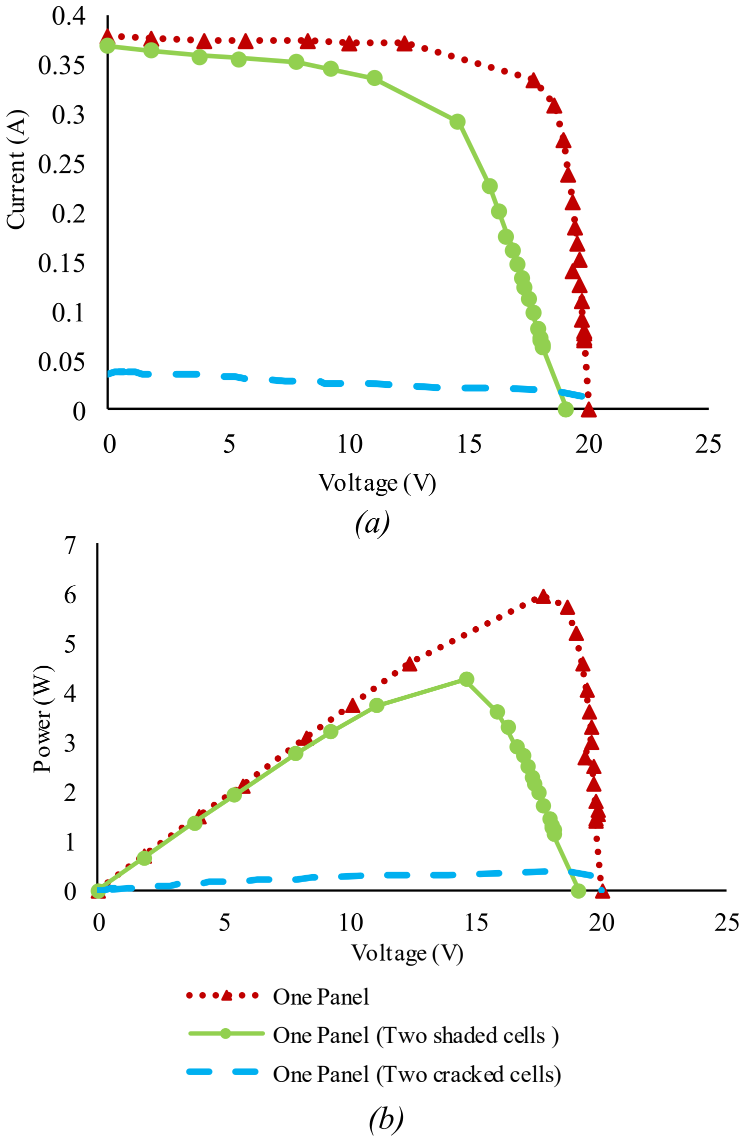

Fig. 2.12 : The performance of one normal panel, one panel with two shaded cells and one panel with two cracked cells. a) I–V curve. b) P–V curve.

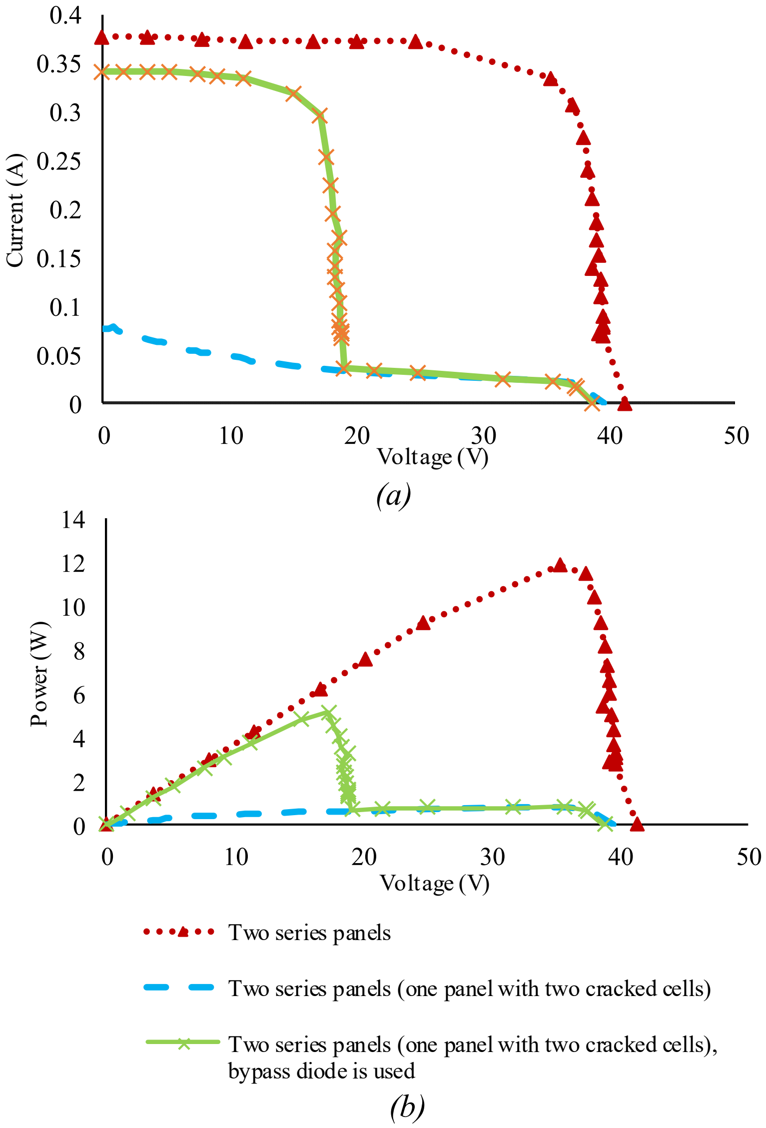

Fig. 2.13 : The performance of two panels connected in series, two panels connected in series with one cracked, and two panels connected in series with one cracked and a bypass diode is connected. a) I–V curve. b) P–V curve.

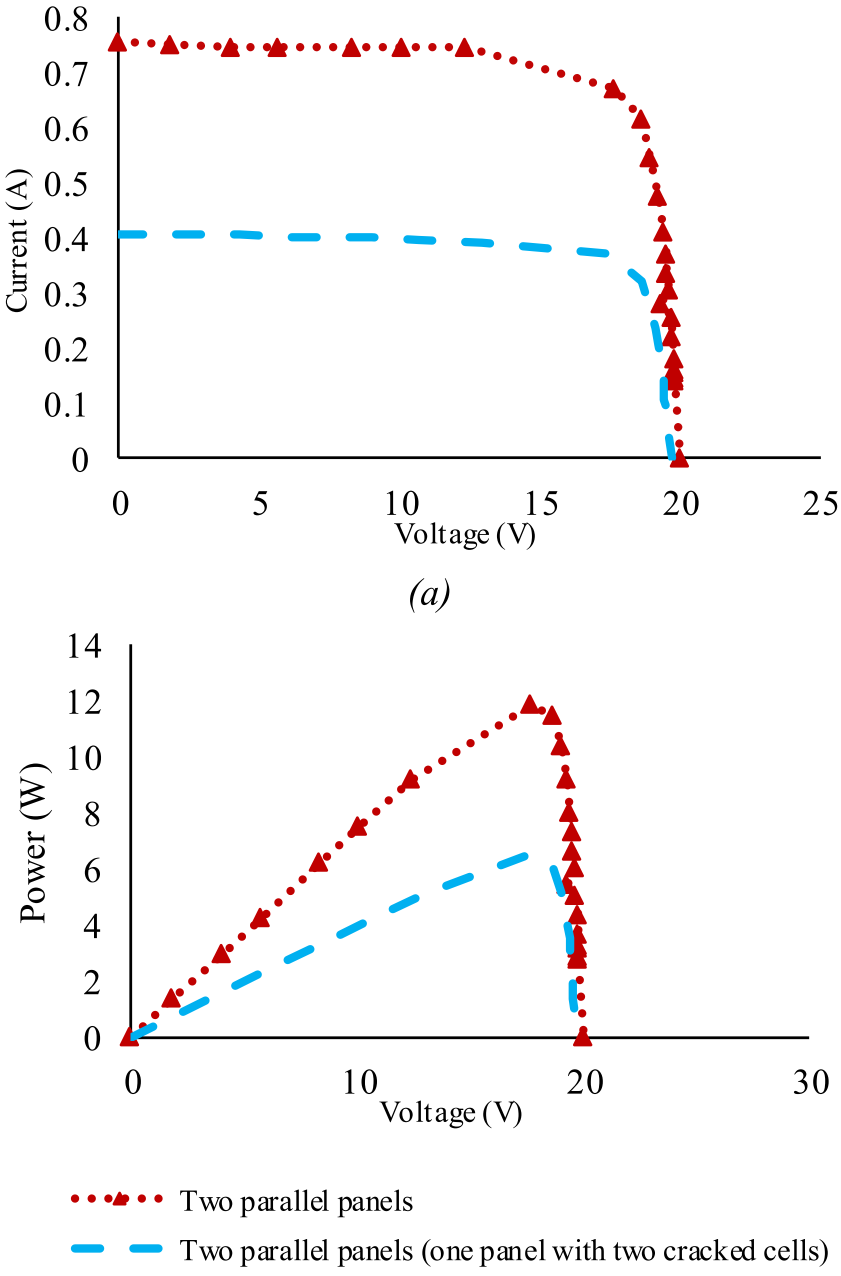

(a)

(b)

Fig. 2.14 : The performance of two panels connected in parallel and two panels connected in parallel with one cracked. a) I–V curve. b) P–V curve.

the AC behaviour of the normal solar string and the cracked solar strings with different severities. The result indicates that the fully cracked strings show a higher resistive and capacitive characteristics at high frequency than others. The results of the experiment show that the current leads the voltage by 27° for the normal string while it increases by 11.66° to become 38.66° for string with one cell totally cracked. Accordingly, the proposed crack detection technique, observing the change in the dynamic behaviour of the solar panel, is regarded as a promising technique to track the cracked, aging and shaded cell to improve overall solar system efficiency and reliability.

A comparison between the series and parallel connected PV panel strings are given. Bypass diodes are recommended to be added to the PV panel string to mitigate the current reduction by the seriously cracked cells. To increase the solar cell lifetime, improve the solar system efficiency and reliability, the proposed crack detection method could be implemented by the solar cell operating converter that may be used for the maximum power point tracking MPPT, or output voltage regulation by injecting AC signal or pulses, then monitoring the reflected current. By detecting the cracked cell, hot spots will be prevented before damaging the solar cell permanently.

Chapter 3

An Analog BJT-Tuned Maximum Power Point Tracking Technique for PV Systems

3.1 Overview

3.1.1 Literature review

With the increasing penetration of photovoltaic (PV) in the energy market due to its clean, quiet and durable features, its performance and reliability become critical. The PV cells have nonlinear electrical properties which require a maximum power point tracker to extract its maximum available power for a given insolation level. The power converter plays a significant role in harvesting energy from the solar module. It is used to harvest the maximum power, control the power flow and regulate the output voltage. The output power from the PV module is affected by the temperature and solar radiation [29] as shown in Fig. 3.1.

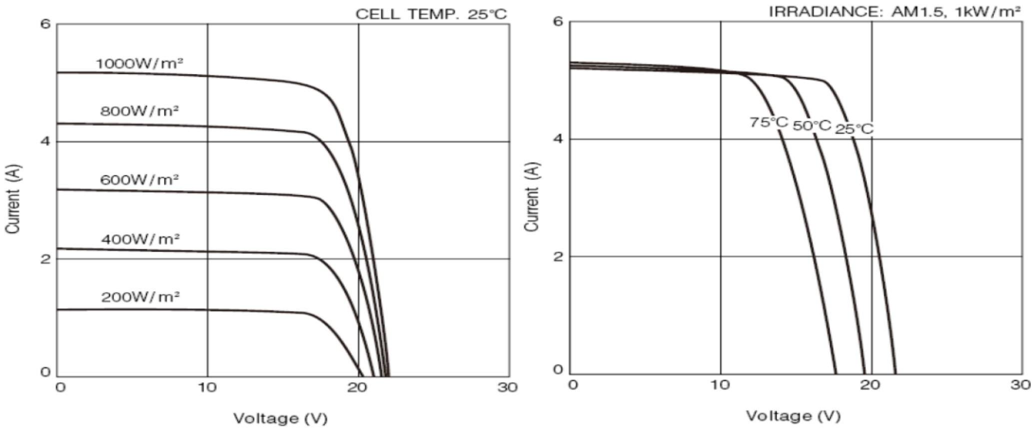

Fig. 3.1 : P-V curve under different temperature and sole radiation [29].

In the last few decades, many MPPT algorithms have been proposed to track the maximum power point [92,3,81,80,71,96,55,59,54]. In general, these algorithms are either too complex, requiring a high-speed computational calculation, or too simple in structure with an inaccurate tracking performance. The most useful techniques are listed below:

- Fraction Open Circuit (FOC) [3, 92].
- Fraction Short Circuit (FSC) [92].
- Perturb and Observe (P&O) [54, 59, 92].
- Incremental Conduction Method (InC) [92].
- Curve-Fitting [96].
- One-Cycle Control (OCC) [96].
- Feedback Voltage or Current [96].
- Current Sweep [96].
- Look-up Table [96].
- Fuzzy Logic (FL)-Based MPPT [96].
- Artificial Neural Network (ANN)-Based MPPT [71].
- Particle Swarm Optimization-Based MPPT (PSO-MPPT) [71].

Each MPPT algorithm has its strengths and weaknesses, in terms of the level of accuracy, tracking speed, algorithm complexity, dynamic tracking under partial shading condition and hardware implementation [53]. For example, feedforward voltage-current MPPT method is considered one of the simplest techniques. A feedforward voltage (or current) uses only one constant reference voltage (or current) in order to indicate the MPP. By controlling the duty cycle of the converter, the error will eventually reach zero, so the PV module operates at the MPP. The disadvantage of this technique is that the reference voltage of the control circuit is constant. Thus, this technique cannot track the maximum power under varying environmental conditions such as changes in the solar radiation and temperature [96].

FOC and FSC require measuring the open-circuit voltage and short circuit current to estimate the voltage and current at the MPP based on the voltage and current proportional constant, respectively. Thus, it is compulsory to disconnect the PV module or the load every time the radiation is changed. This results in frequent and long power interruptions from the load perspective if the radiation changes rapidly [92].

For P&O, the photovoltaic current and voltage are measured to calculate the operation power $P_{mpp-active}$. Then, a small perturb in the duty cycle is introduced to measure the current and voltage again in order to calculate a new value of power $P_{mpp-new}$. Since the comparison of power points ($P_{mpp-active}$ and $P_{mpp-new}$) is continuously performed, the PV voltage oscillates around the vicinity maximum power point instead of remaining at the MPP. However, the disadvantages of this algorithm are that the voltage continually oscillates around MPP, and the MPP efficiency is reduced further if the step size is large [59, 40].

In the Incremental Conduction (InC) algorithm, the slope of the P-V curve is used to achieve MPP. The value of the slope represents the ratio of the incremental conductance to the instantaneous conductance of the PV module. Depending on the three InC algorithm conditions, the duty cycle of the power control can be used to move right or left along the PV curve to achieve maximum power point. Furthermore, this technique is similar to perturbation and observation, and it is utilized in either connection mode stand-alone or grid connection [68, 86].

Under partial shading condition PSC, the I-V and P-V curves are shaped quite differently [112]. If the PV panels are connected in series and parallel to form an array and at least one PV panel is shaded, the numerous peaks or maxima will be lower than the maximum global power. PSC reduces MPPT algorithm efficiency, and it makes it hard to differentiate between the global and local maximum power point [15]. One of the best methods to solve the partial shading effect is tracking the MPP in the PV module level, but this will increase the cost of the system. To overcome this issue, a cost-effective MPP technique is required to be implemented with the PV module.

The implementation of MPPT algorithms can be analog, digital or mixed-signal [55]. In general, the digital control circuit used to track MPP would be much more complicated and expensive than the analog control circuit [96]. In fact, for some applications, such as spacecraft and satellite that rely on solar energy to generate power, the use of an analog control circuit is preferred because of the single-event effects (SEE) caused by the high energy partials from the sun. SEE could cause bit-flips in a memory or register transient pulse or latch-up in the digital logic circuits of a digital control. To reduce the effect of SEE, radiation-hardened technique is applied to these devices. However, the cost and complexity of the system would increase [90]. The analog control circuit is also preferred for indoor energy harvesting such as wireless sensor network [55, 3, 59, 54] and PV antenna [30] because of its low energy consumption.

3.1.2 Research gap/problem

MPPT algorithms can be implemented by an analog or a digital controller. Using the analog control circuit to implement simple MPPT algorithms such as FOC, FSC, feedback voltage and feedback current algorithms which reduces the cost of the system and simplifies the circuit design. However, the accuracy of MPPT is low when the solar insolation is rapidly changing due to their inability or slowness to find a new MPP. On the other hand, the digital control circuit has access to the memory function, the accuracy of operating at the MPP will improve even when the solar radiation variation is high. However, microcontrollers generally are comparatively more sensitive to switching noise and are of higher cost if compared to its analog implementation.

In this chapter, a simple and cost-effective analog MPPT circuit with an improved tracking accuracy is proposed for PV modules. The algorithm is voltage-based but uses a BJT-tuned circuit to better model and track the I-V characteristics of the PV module. The chapter is organized as follows: In Section 3.2, the proposed analog maximum power point algorithm is introduced and analyzed. In Section 3.3, the system setup is discussed. The results are explained and shown in Section 3.4, followed by the conclusion in Section 3.5.

3.2 Operation Principle, Analysis and Implementation of Proposed MPPT

3.2.1 Operation Principle of the Proposed MPPT

A block diagram of the proposed analog MPPT method is shown in Fig. 3.2. It is a voltage and current feedforward control which consists of a BJT, an AND gate, a voltage comparator and a PWM signal generator. The PV voltage is sensed and compared with the voltage reference determined by the BJT. The BJT senses the PV current and implements a variable reference voltage. Thus, any changes in the radiation will lead to a change in the reference voltage, without the need to use a digital controller and a PID controller. An output ‘high’ from the voltage comparator signals a demand for increasing power intake from PV panel and vice versa. A PWM signal generator presets the maximum duty cycle (D) and provides a dead-time to prevent magnetic saturation of the inductor in step-up converters. The voltage comparator and the AND gate work together and reshape the PWM signal to proper PWM patterns with different effective duty cycles to operate the power converter (a boost converter is used in this study) in order to track the maximum power under different insolation levels.

A voltage-feedforward control has been firstly discussed in [47] in order to approximately operate the PV module at MPP. It is considered the simplest MPPT algorithm technique to implement because it compares the operating voltage of the PV module with a constant reference voltage V_{ref}. However, the effects of the changes in solar radiation were not considered. Fraction open circuit voltage (FOC) algorithm is the modified version of the voltage-feedforward control, where the V_{ref} can be modified according to the changes in the solar radiation. In FOC, the open circuit voltage V_{OC} has to be measured to calculate the voltage at MPP V_{MPP}, according to the below linear relationship [96]:

$$V_{MPP} = K_1 * V_{OC} \tag{3.1}$$

where K_1 is the voltage proportional constant, and it has a value between 0.71 and 0.78 depending on the characteristics of the PV module. The main disadvantage of this method is the loss of power when the PV model is disconnected from the system to measure the V_{OC} and scan the entire range of the duty cycle to find V_{MPP}. One potential solution to this issue is the use of a pilot PV cell which has the same characteristic of PV module [103, 9]. However, using a pilot cell would increase the cost and complexity of the system [3].

In the proposed algorithm, once the initial I-V measurement is completed, there is no need to disconnect the PV module frequently to measure V_{OC} in order to reposition the voltage at the maximum power point. Hence, the closed-loop voltage feedforward can be used to sense the input voltage and current. As a result, the

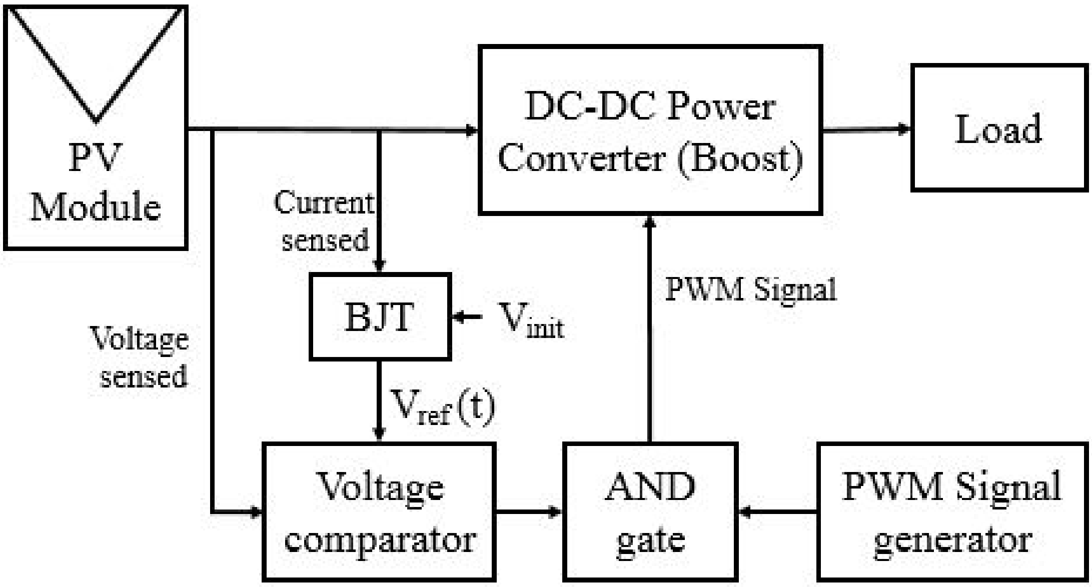

Fig. 3.2 : Proposed improved analog MPPT technique using a voltage-based, BJT-tuned circuit.

drawbacks of fraction open circuit are solved.

As shown in Fig. 3.3, the MPPs of the PV module under different solar radiation levels can be joined by roughly a straight line. The right slope could be found initially by connecting the PV module with a variable resistor bank and measuring the currents and the voltages at different solar radiation levels and impedances. Then, based on the measured values, the P-V curve can be drawn. Thus, the right MPP curve is determined. Then, the proposed algorithm operates the power converter along this line by using a variable reference voltage. This reference voltage, which can be changed according to the solar radiation, can be implemented using a bipolar junction transistor (BJT).

3.2.2 Analysis of the Proposed Analog MPPT Method

3.2.2.1 BJT

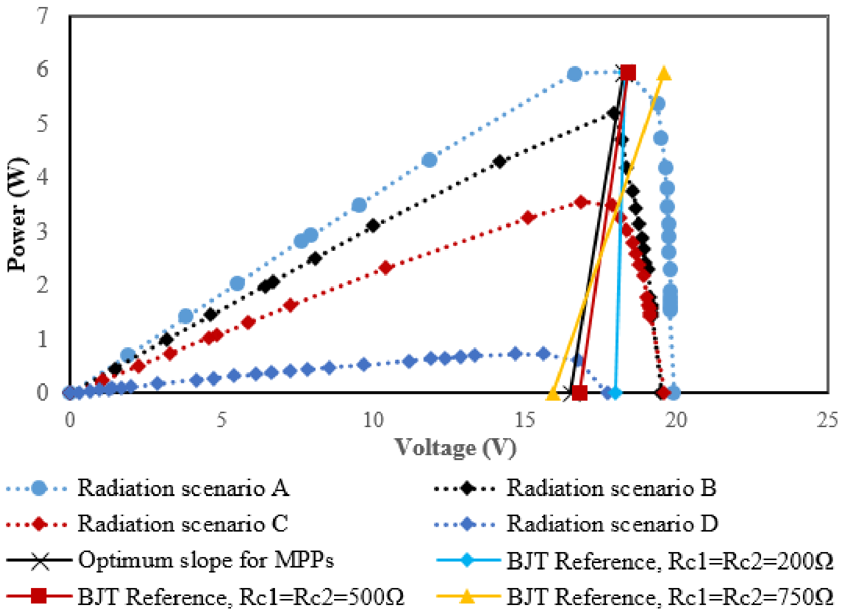

Fig. 3.3 : P-V curve and different voltage reference lines for varying isolation levels.

The bipolar junction transistor (BJT), shows in Fig. 3.4(a), has four regions of operation, cut-off, saturation, active and breakdown regions as shown in Fig. 3.4(b). In the active region, the transistor acts as an amplifier. Therefore, the BJT can be simply used as a controller by implementing the relation between the base and the collector currents. By applying Kirchhoff's voltage law (KVL) on the output closed-loop, the following relationship among the key parameters is derived

$$V_{Ref} - I_C R_C - V_{CE} - I_E R_E = 0 \tag{3.2}$$

In order to make sure that the transistor operates in the active region, the collector-base junction must be reversely biased ($V_{CE} \geq V_{BE}$).

For a better understanding of the control method, the BJT output characteristic (load line) is drawn in Fig. 3.4(b). By substituting $V_{CE} = 0$ in (3.2), the maximum collector current equals $I_C = V_{ref}/(R_C + R_E)$, and by substituting $I_C = 0$ in (3.2), the collector-emitter voltage equals $V_{CE} = V_{ref}$. It is illustrated by the load line that the operation points (Q-Points) will change if the base current (voltage) is changed.

For example, when the base current equals I_{B1}, the output operation point will be at point A. According to $I_C = \beta * I_B$, where β is the BJT DC current gain, the collector current equals $I_C(I_{B1})$ or $I_{C,A}$ and the collector-emitter voltage equals $V_{CE}(I_{B1})$ or $V_{CE,A}$, and so on for other operation points B and C.

3.2.2.2 PWM Signal Generating in Analog Control

Fig. 3.5 shows the simulation of the proposed MPPT algorithm and PWM

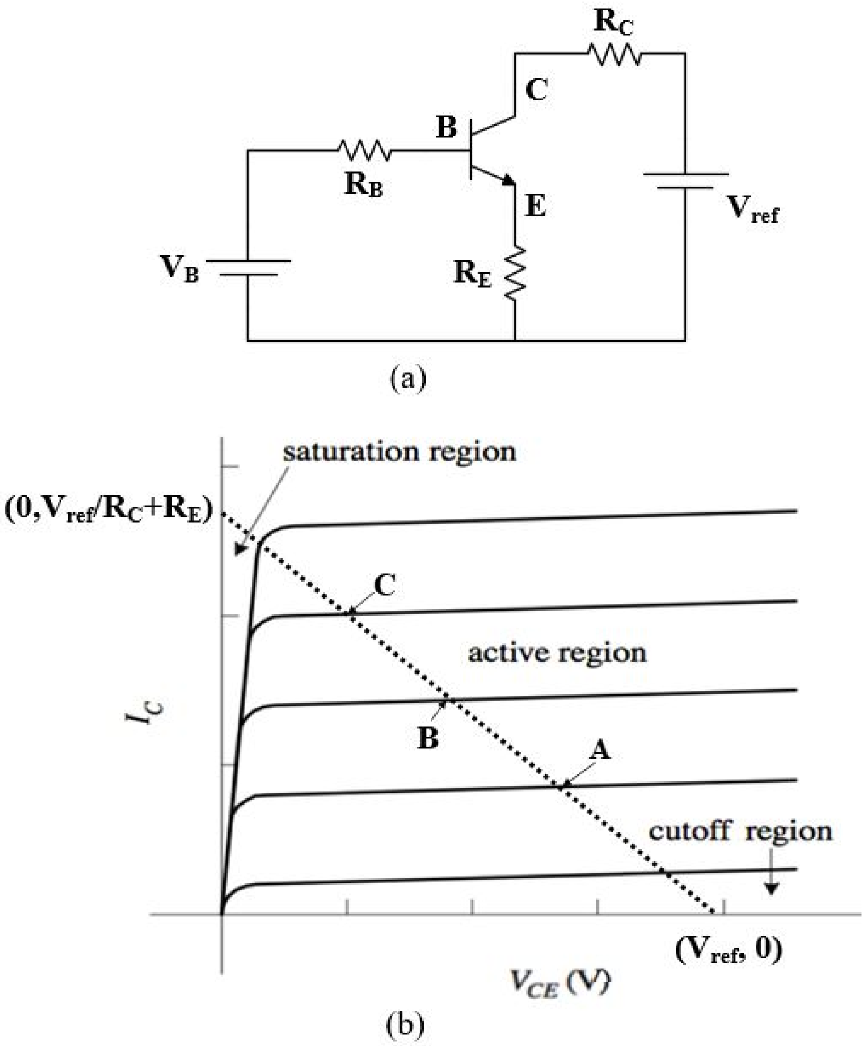

(a)

(b)

Fig. 3.4 : a) BJT circuit. b) BJT load line.

generation, used in the proposed algorithm. Firstly, a PWM signal ,Fig. 3.5(c), needs to be generated from a PWM generator. This signal has a constant frequency, amplitude and duty cycle. Secondly, the updated reference voltage (desired signal), which is taken from the Darlington pair collector terminal, and the sensed PV panel voltage (controlled signal) are compared using a voltage comparator. The output of the voltage comparator ,Fig. 3.5(b), becomes high "1" if the PV voltage is greater than the reference (desired) voltage, and vice versa for a low "0" output. Thus, the output of the voltage comparator will generate an enable signal for the PWM generation.

Finally, the AND gate is used to compare the output of the voltage comparator and PWM signal generated from the PWM generator. As a result, the output signal from the AND gate will be a PWM signal with different effective duty cycles depending on the value of the desired signal and the controlled signal as shown in Fig. 3.5(d). This PWM signal will control the MOSFET driver of the boost converter. Note that in effect, it is somewhat similar to burst mode control technique.

3.2.3 Implementation of the Proposed Analog MPPT Method

Fig. 3.6 shows a circuit schematic diagram of the hardware system. The upper part shows the power stage boost converter where the inductance, MOSFET, diode and capacitance are 100 µH, IRF1405, BY229 and 470 µF respectively. The lower part shows the proposed control circuit – the current sensor is formed by R_{sens} and an RC filter (100 nF and 1 kΩ). A Darlington BJT pair circuit, which is formed by BC549, provides the varying reference voltage, based on (3.5), to the negative pin of the voltage comparator LT1011. The positive pin of the voltage comparator is tracking the PV voltage after it is scaled down by the voltage divider (9 kΩ and 1 kΩ). The AND gate (HEF4082B) mixes the output of LT1011 and the preset PWM signal to reshape the PWM signals that feed into the gate driver TC4428 to drive the power MOSFET. Assuming lossless condition and using the boost converter voltage conversion ratio in continuous conduction mode, the impedance match of the boost converter is given as below

$$R_{PV} = (1 - D)^2 R_O \tag{3.3}$$

where R_O is the output equivalent resistance, and R_{PV} is the equivalent resistance seen by the PV panel. The converter is used to match the input and the output impedances to track the maximum power point. In the first stage of the experiment that will be discussed later, the resistance value that generates the maximum power experimentally equals 57 Ω. In the second stage, the fixed output resistance is assumed to be equal to 220 Ω. By using (3.3), the duty cycle of the boost converter should be at least equal or above 49%.

With the use of BJT in setting the reference voltage, it is important to select the initial reference voltage V_{init}, the base resistor, the collector resistor and the emitter resistor properly to achieve more accurate results. The initial reference voltage V_{init} equals the average voltage at MPPs.

The Output current of the PV module is sensed using a small resistor R_{sens}. Thus, the input current is presented by the voltage across the resistor, $V_{sens} = I_{PV} * R_{sens}$. As the PV module current (voltage across the sensing resistor) flows to the base of the first BJT, the output voltage V_{CE1}, given in (3.4), will change according to the change of the PV current and radiation levels. In fact, the slope of the BJT load line and the slope of the MPPs line is reflected, and then the second BJT is used to reflect the output voltage; therefore, any increase in the input voltage will lead to an increase in output reference voltage and vice versa.

$$V_{CE1} = V_{init} - \beta * R_{C1} \frac{V_{sens} - V_{BE}}{R_{B1} + (1 + \beta) R_{E1}} \tag{3.4}$$

As the two BJTs are cascaded, the output voltage of the first BJT is connected to

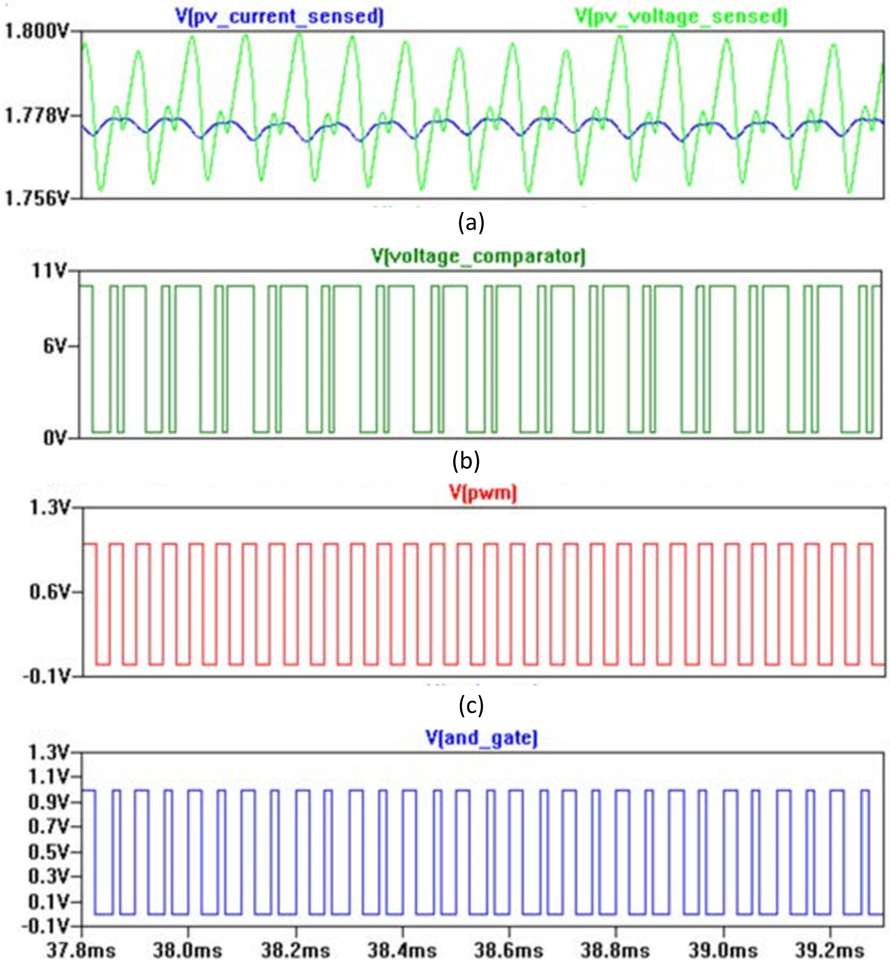

(a)

(b)

(c)

(d)

Fig. 3.5 : Simulation result. a) Solar panel voltage and reference voltage from the Darlington BJT pair which controlled by the PV current. b) Voltage comparator output voltage. c) Constant PWM signal. d) AND gate output voltage.

the base of the second, so the second BJT will be used as a mirror for the V_{CE1}. As a result, the output voltage of the cascaded BJTs, which becomes the MPP reference voltage $V_{ref}(t)$, is given as below

$$V_{ref}(t) = V_{init} - \beta * R_{C2} \frac{V_{CE1} - V_{BE}}{R_{B2} + (1+\beta)R_{E2}} \tag{3.5}$$

If the solar radiation level is changed, the base current will change, i.e. from I_{B1} to I_{B2}, and the BJT operation point will move from point A to point B. Thus, it is possible to generate a variable reference voltage V_{CE} that matches the desired slope of PV module's MPPs if a BJT with proper β is selected correctly. According to (3.5), a BJT with high β and higher collector resistor is suitable for a PV module with a high slope of MPP curve at different radiation levels, and vice versa as shown in Fig. 3.3.

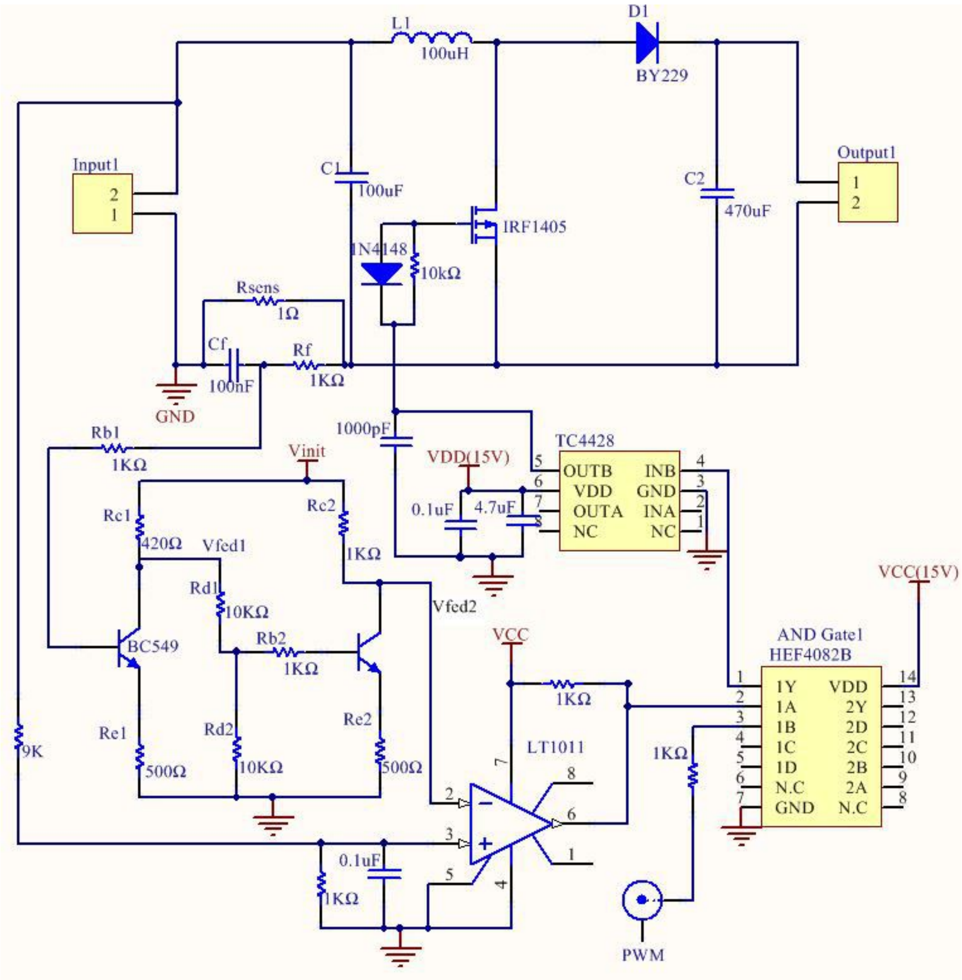

Fig. 3.6 : Schematic diagram of the experimental setup.

3.3 Experimental Setup

A 20W photovoltaic panel was used to verify the proposed circuit by generating power to the boost converter. One 500 W halogen lamp and two 30 W led lamps were used to simulate different solar radiation levels.

The first stage of the experiment was to get the I-V and P-V curves of the PV panel at different solar radiation levels in order to calculate the correct voltage reference and other experimental parameters, such as inductor, capacitor and resistors. Thus, the PV panel was connected with a variable resistance bank, its value varies between 0 to 250 Ω, and the PV panel voltage and current were recorded for different resistor values. This stage was repeated for four different solar radiation scenarios, namely, Radiations A, B, C and D. Radiation scenario A was simulated by using one halogen lamp, and the distance between the lamp and the PV module was 30cm. Also, Radiation scenarios B and C were simulated by using the same halogen lamp, but the distance between the PV module and the lamp was changed to 45 cm and 60 cm respectively. Radiation scenario D was simulated by using two LED lamps at

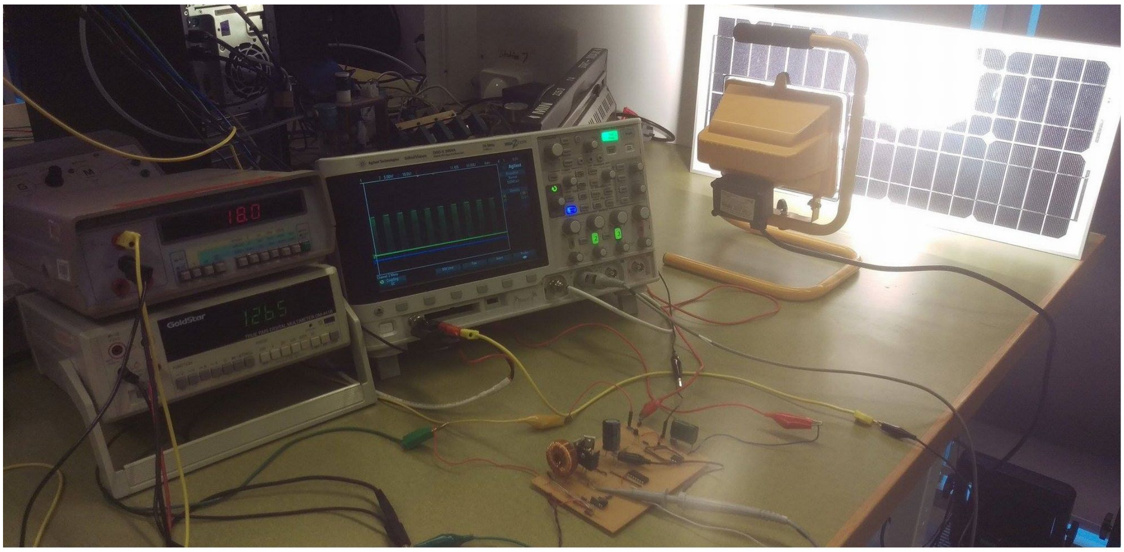

Fig. 3.7 : Experimental setup.

a distance of 20cm from the PV module. Then MATLAB and Excel were used to calculate the output power and to plot the I-V and P-V curve. This curve is shown in Fig. 3.3.

The second stage of the experiment was to verify the proposed circuit, so the laboratory prototype was built as shown in Fig. 3.7. In this stage, the same simulated four solar radiation levels were used, but in this stage, the output port of the converter was connected with a constant resistance in order to verify that the proposed circuit is correctly matching the input and output impedances to track the MPP. The PV module voltage and current are sensed to calculate the total generated power in each scenario. The measured power consumption for the complete MPPT sensor, which includes the BJT for setting the variable reference voltages, a voltage comparator, a MOSFET driver and the voltage dividers, is 43.78 mW.

The third stage was to compare the proposed method with the constant voltage method. To do this, the reference voltage was given a constant value. This is equal to the voltage at the maximum power point, so the duty cycle of the boost converter is constant. The output voltage and current of the PV module are recorded at different solar radiation levels.

3.4 Experimental Results

Firstly the PV module has different operation voltages as listed in Table 3.1. When the MPP moves away from the preset value due to the decreasing insolation level, the tracking efficiency for the constant voltage method reduces significantly. Fig. 3.8(a) shows the transient response when the solar insolation changes from radiation level B to A then returns to B. The PV module voltage remains constant even when the solar radiation is changing. Thus, this proves the drawback and the limitation of using the constant voltage control method to track true MPPs. However, in the proposed algorithm, the voltage variation at different MPPs is taken into consideration by changing the reference voltage according to the change in the solar radiation. The experimental results show improved MPPT efficiency. It varies between 99.2-93.39% for the wide insolation range as compared to efficiency at 97-76%in [90]. The PV panel voltage and the output voltage for the proposed algorithm in response to insolation changes are shown in Fig. 3.8(b). It can be seen that the PV voltage has adjusted slightly to track the MPPs better. Another advantage of proposed circuit is direct MPPT at the startup due to the initial setup at MPP.

Table 3.1 : Comparison of MPPT Performances Between Constant Voltage Reference and Proposed Variable Voltage Reference Method.

Equivalent solar radiation			**PV Module parameters at MPP**		**Constant voltage reference**			**FOV**			**FSC**			**Proposed circuit**		
Radiation Levels scenarios	Insolation (W/mˆ2)	Ambient temperature	Voltage (V)	Power (W)	Voltage (V)	Power (W)	MPPT Efficiency (%)	Voltage (V)	Power (W)	MPPT Efficiency (%)	Voltage (V)	Power (W)	MPPT Efficiency (%)	Voltage (V)	Power (W)	MPPT Efficiency (%)
A	760	32	16.62	6.29	17.65	6.63	99.6	16.49	5.87	93.32	17	5.78	91.88	17.88	6.24	99.2
B	510	29	17.55	5.09	17.65	4.27	83.92	15.91	4.98	94.09	17.8	4.98	97.92	17.69	4.97	97.67
C	370	27	16.37	3.45	17.65	2.64	76.65	17.01	3.23	97.09	17.01	3.23	93.91	16.39	3.29	95.37
D	50	25	14.69	0.73	17.65	0.44	60.08	13.6	0.64	88.93	13.6	0.64	87.03	14	0.686	93.39

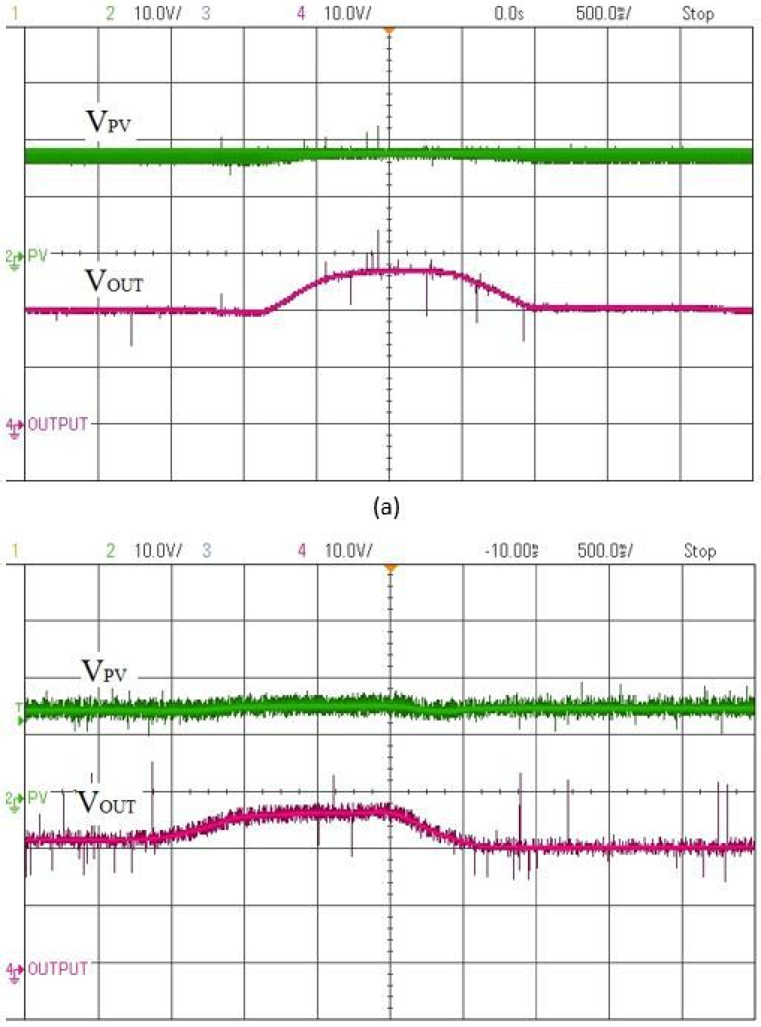

(a)

(b)

Fig. 3.8 : Transient response of PV voltage and corresponding boost converter output voltage during changes in insolation levels: a) by using constant voltage reference. b) by using proposed circuit. [Time base: 500ms. Voltage: 10V/div].

3.5 Summary

This chapter presents an improved analog maximum power point tracking algorithm for the PV system with a tracking efficiency ranging from 93.39 to 99.2% for different solar insolation levels. The proposed circuit shows reduction of tracking error compared with traditional methods as the efficiency ranging between 60.08%-99.6% for constant voltage reference method, 88.93%-93.32% for FOC method and 87.03%-

91.88% for FSC method. The proposed circuit is based on a simple voltage and current feedforward- feedback control. In addition, it takes the advantage of the BJT where the collector current is used to mimic a voltage slope which connects the maximum power voltage points for more accurate tracking. The operation of the proposed analog control is experimentally verified using a 20 W photovoltaic panel. Potential applications for the proposed MPPT circuit are aerospace and low-cost systems due to its pure analog implementation, and it does not require digital memory and control. The proposed approach is best suited for per panel implementation.

Chapter 4

Literature Review of Multiport Power Converters

4.1 Overview

The use of renewable energy sources RES, such as solar, wind, tide, geothermal and wave become popular in recent years as they are environmentally clean and abundant in nature [17]. However, these renewable energy sources have an intermittent nature and are generally unreliable. To resolve this issue, these sources need to be connected to the load through power electronic converters. These power converters perform maximum power tracking from the renewable energy sources, manage the grid and load voltage requirements and interface the renewable energy sources with the energy storage system [72].

Traditionally, a single DC-DC power converter with two ports are used to connect only one energy source with the load [35, 42]. To use more than one input power source or energy storage system (ESS), two or more power converters are required [118], as shown in Fig. 4.1. These power converters could be unidirectional power flow if they are connected to a power source or it could be bidirectional power flow if it is connected to the ESS. Thus, the cost, the number of component and complexity of the system will increase, and the system efficiency will decrease as these converters are normally cascaded [117].

The multiport converter, particularly the three-port converter, Fig. 4.2, offers a better design and implementation for the renewable energy system, electric vehicle, aerospace application and DC distribution power system [14, 72, 82]. As a result, using multiport converters has some advantages, including reducing the cost and

Fig. 4.1 : Traditional multiport connection in a standalone power system: a) Multi-input ports. b) Multi-output ports.

the mass of the system, and improving power density by sharing some components such as switches, capacitors and storage elements [77]. Also, it increases the system reliability and uses central control, so fewer communication channels are required causing no communication delays or errors. Moreover, using a multiport converter offers multi-input multi-output (MIMO) feature, and enhances the dynamic performance of the system [121, 14, 82]. In many applications, a high voltage gain is required; by using the multiport converter structure a high voltage gain can be achieved easily [31].

The three-port converter power can be expressed in (4.1), and its operation mode can be classified into four groups namely; single-input single-output (SISO), single-input dual-output (SIDO), dual-input single-output (DISO) and dual-input dual-output (DIDO). SISO mode occurs when only two ports are active, and the power at the ports is equal. SIDO mode occurs when the input power is greater than the output power, so some of the generated power will be transferred to the storage element. DISO occurs when the input power is less than the demand, so the storage element will supply some power to the load. The last mode, which is (DIDO) occurs when the input power is almost equal to the demand, but the input power is not stable, so the storage element will store and supply some energy to

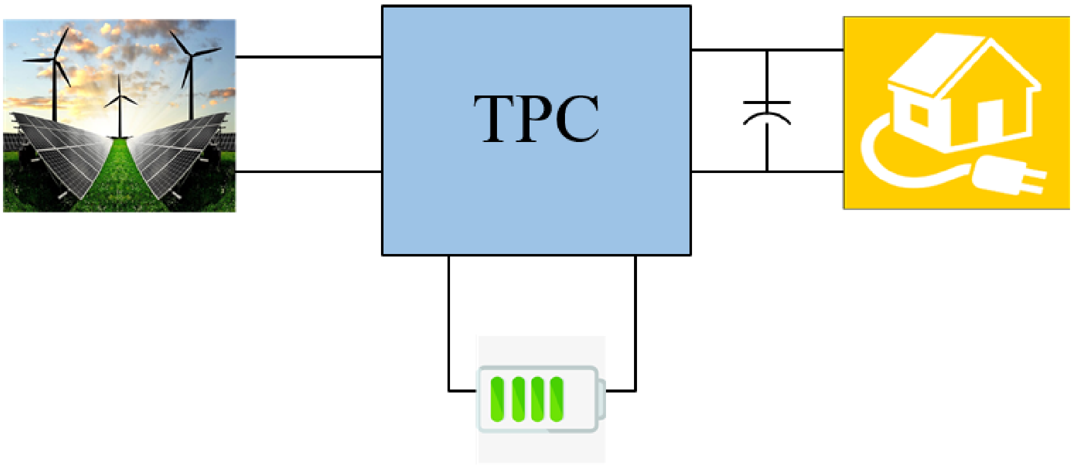

Fig. 4.2 : Three-port converter TPC.

smooth the output power of the solar energy source.

$$P_O = P_{in} + P_B \tag{4.1}$$

where P_O is the output DC power of the converter, P_{in} is the renewable energy source power, and P_B is the battery bidirectional power.

In recent years, several multiport converters (MPC) have been proposed [121, 22, 50, 97, 25, 83, 113, 119, 8, 115, 23, 124, 39, 38, 46]. In general, three-port converters (TPC) are the common MPC, where three ports are used. MPC can be divided into three groups, namely: non-isolated, isolated and partly isolated converters. The three categories of TPC are depicted in Fig. 4.4. Each category has its complexity, number of components, reliability and power ratio. The most recent reported MPC will be reviewed in this chapter; this review helps to select the best topology for a specific application.

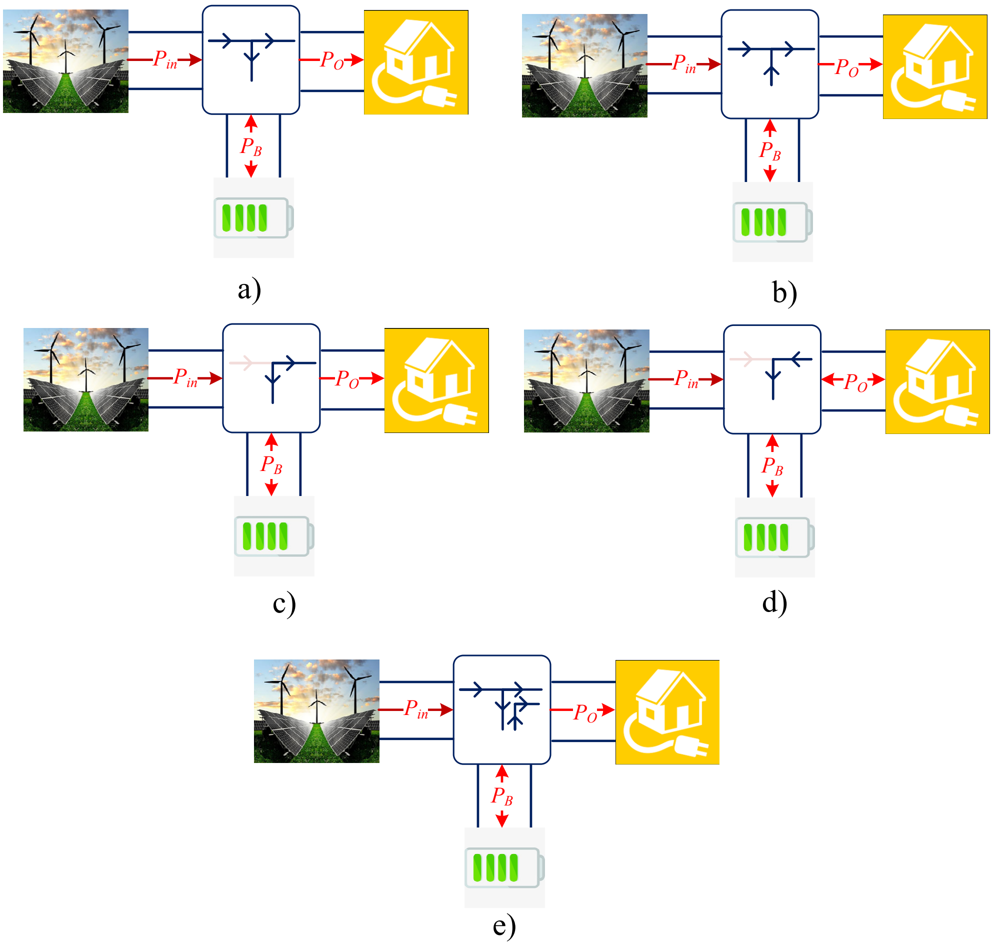

Fig. 4.3 : The general configuration of a renewable energy generation system using a three-port converter: (a) SIDO mode. (b) DISO mode. (c) SISO mode. (d) SISO mode for grid-connected system. (e) DIDO mode.

4.1.1 Non-Isolated Multiport Converter

A non-isolated power converter is used for some applications where the isolation feature is not necessary among the ports. This type of topology has some advantages, such as low cost, high power density and high efficiency [125]. In this topology, all ports are directly connected to each other, and they share the same ground; accordingly it is called non-isolated. In addition, another disadvantage for this topology is the voltage gain between the ports is not relatively large. Thus, in some

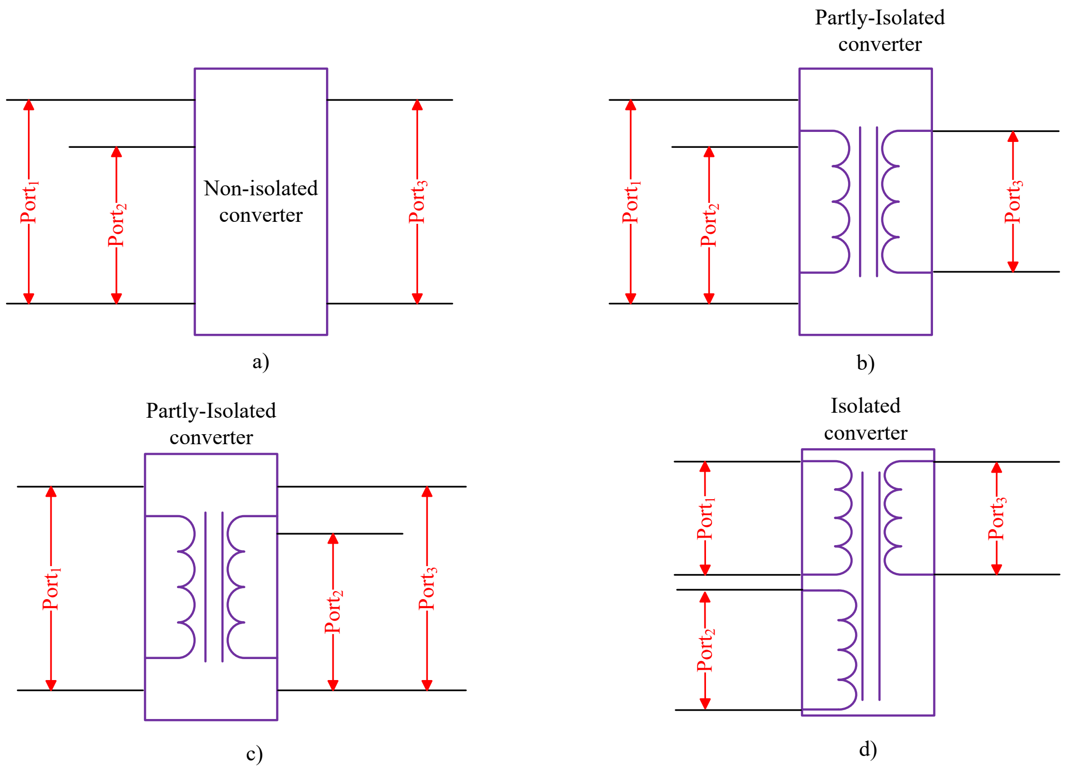

Fig. 4.4 : MPC category: (a) Non-isolated converter. (b), (c) partly isolated converter. (d) Isolated converter.

cases, when there is a need to transfer power in high voltage gain, multi-stages converters are used [66]. Most of the proposed non-isolated multiport converters are based on the traditional DC-DC converter such as buck, boost, buck/boost, Cuk, SEPIC and Zeta converter.

Fig. 4.5 shows a simple design of multi-input buck-boost converter that proposed in [35]. This topology could be used to connect N number of the input sources that have different characteristics. The advantages of using this topology are the low component count and simplicity of control. In the given design, the inputs share one inductor, diode and capacitor. Nevertheless, the ports in this topology are unidirectional power flow. Consequently, this topology is not suitable for ESS.

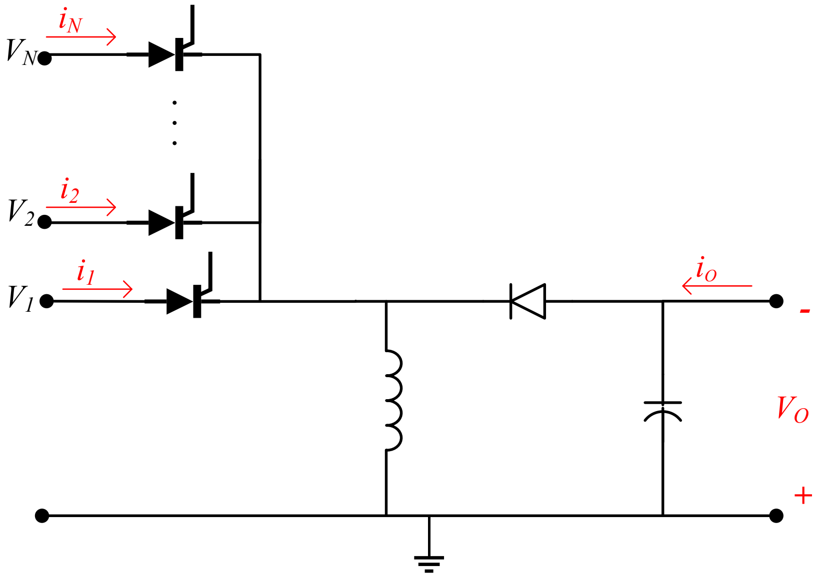

Fig. 4.5 : Multi-input buck-boost converter [35].

Fig. 4.6 shows a multiport converter which is based on the converter proposed in [52]. In addition to the advantages of the previous converter, the output voltage of the new proposed converter has a positive polarity without using an additional transformer. The new modified converter has a bidirectional power flow without a need for an additional converter, and it can act as a buck, boost and buck-boost converter. The converter is designed to operate in both modes, continuous conduction mode (CCM) and discontinuous conduction mode (DCM).

Fig. 4.7 shows a boost three-port non-isolated converter, proposed in [116]. The proposed circuit is used to interface one renewable energy source, battery and load simultaneously. The advantage of this topology is that the power can be transferred simultaneously between the three ports. To smooth the pulsation current of the PV panel and battery, two filter capacitors are connected in parallel with the PV panel and battery. The proposed convert has three operation modes namely; dual-output (DO), dual-input (DI) and single-input single-output (SISO) modes. In

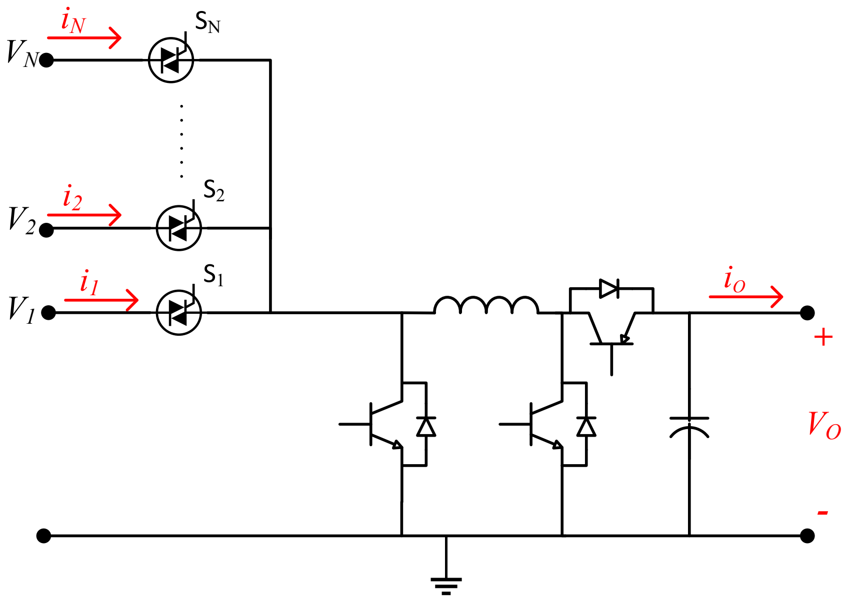

Fig. 4.6 : Multi-input buck-boost converter [52].

order to verify the visibility of the proposed converter, 1-kW prototype is built and experiments have been carried out.

The authors of [8] proposed a single-switch non-isolated DC/DC converter. The number of components is reduced by combining a cascade buck converted with a buck-boost converter. The combination of buck and buck-boost converter has only one switch that can perform maximum power point track (MPPT), manage the battery charging and drive the load, which is a water pump in this study, at a constant flow rate simultaneously. The proposed circuit is depicted in Fig. 4.8. In order to verify the visibility of the proposed converter, a 14-W laboratory prototype is built and texted with a pulse-frequency modulation (PFM) control scheme.

The authors of [39] proposed a non-isolated high step-up three-port converter (TPC) as shown in Fig. 4.9. In order to achieve high voltage gain coupled inductors techniques are used. Two clamped circuits are utilized to suppress the leakage inductance effect. The proposed converter has two distinct power flow paths, one from the main voltage source to the load, and another from the battery to the load. The proposed TPC has three different modes described as follows: transferring power from the input power source and the ESS to the load independently by using the two distinct power flow paths, transferring power from the input power source and the ESS to the load simultaneously and transferring power from the input power source to the load and charging the ESS, simultaneously. The converter is implemented and tested on a 150 W-400 V load.

A battery-integrated boost converter proposed in [37] has only one switch, one diode and one capacitor as shown in Fig. 4.10. A series combination of input solar power and battery offers a direct path to charge the battery, and it also helps to track the maximum power from the solar energy source. The proposed converter can facilitate the distributed maximum power point tracking (DMPPT). The proposed converter is not able to provide power during night-time as the PV module becomes

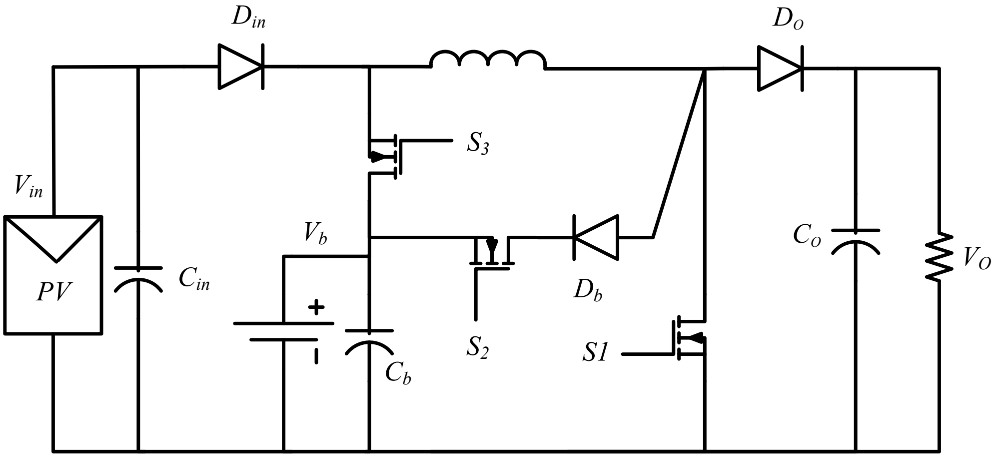

Fig. 4.7 : Boost three-port converter (TPC) proposed in [116].

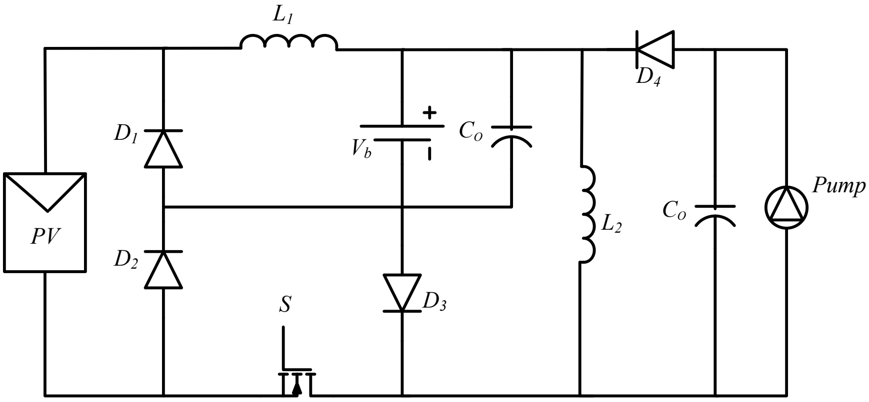

Fig. 4.8 : Single-switch non-isolated dc/dc converter [8].

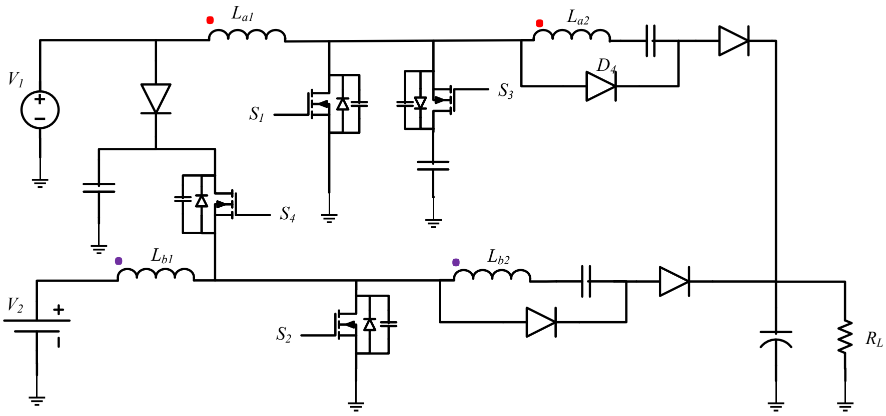

Fig. 4.9 : Non-isolated high step-up three-port DC–DC converter for hybrid energy systems [39].

an open circuit, and the diode does not allow the current to flow in the opposite direction.

4.1.2 Partly-Isolated Converter

In the partly-isolated multiport port converter, there are at least two ports that are directly connected to each other, sharing the same ground; meanwhile, there is at least one port that is connected to a high-frequency transformer [87]. This kind of arrangement is used to afford galvanic isolation for some ports. In addition to offering the isolation feature, the high-frequency transformer is used to achieve a high voltage gain by changing the turns ratio of the transformer.

The authors of [82, 5] introduced a partly-isolated three-port converter that has solar energy port, battery port and output port. The proposed circuit, as shown in Fig. 4.11, is based on the half-bridge converter and the principles of an active clamped forward converter. One switch and one diode are added to the primary side of the transformer, and two switches replaced the output diode for the traditional half-bridge converter.

Meanwhile, the authors of [114] proposed a family of three-port half-bridge converters (TPHBC) namely: three-port half-bridge converters with post regulation (TPHBC-PR), three-port half-bridge converters synchronous regulation (TPHBC-SR) and three-port half-bridge converters with primary freewheeling (TPHBC-PF).

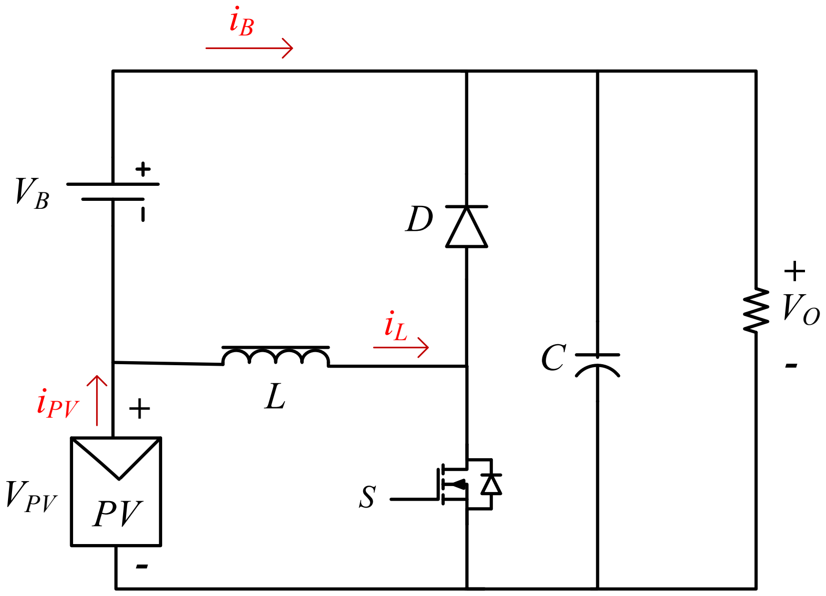

Fig. 4.10 : Three-port battery-integrated boost converter [37].

The converters are suitable for a stand-alone renewable power system. The schematic diagram is shown in Fig. 4.12. The converter efficiency drops at a high output voltage because of the reverse recovery loss associated with the body diode of the output switches.

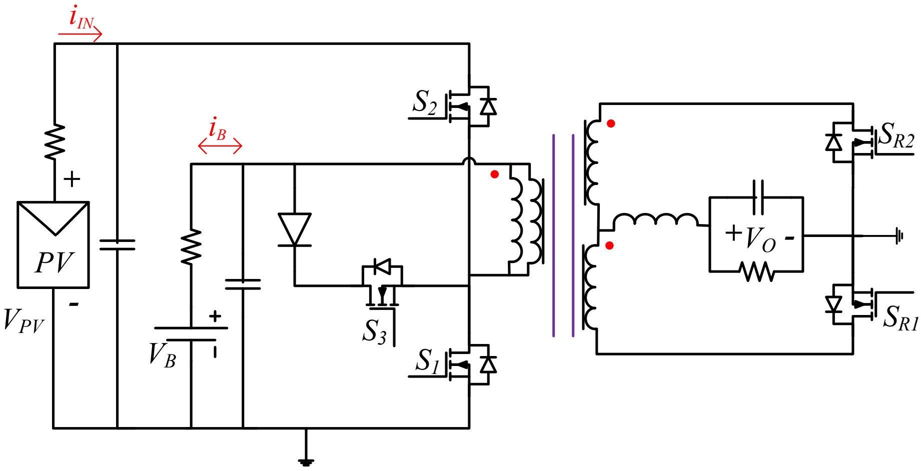

Fig. 4.11 : The converter proposed in [82].

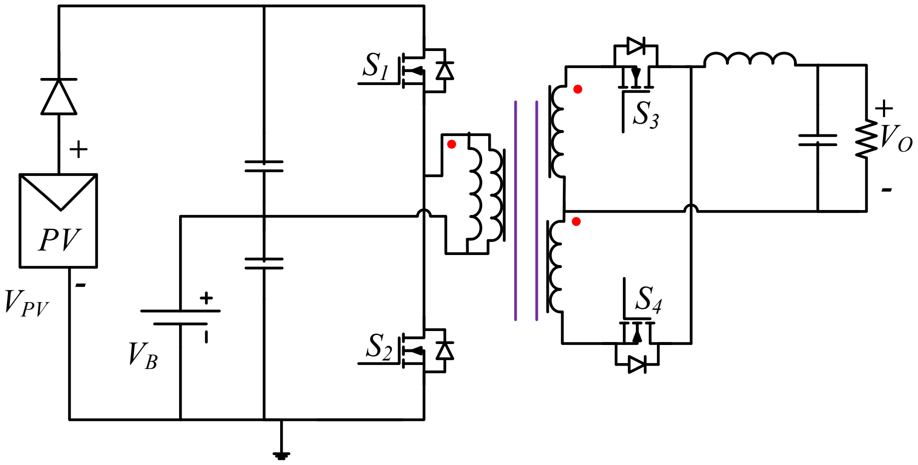

Fig. 4.12 : Three-port half-bridge converter with synchronous regulation (TPHBC-SR) proposed in [114].

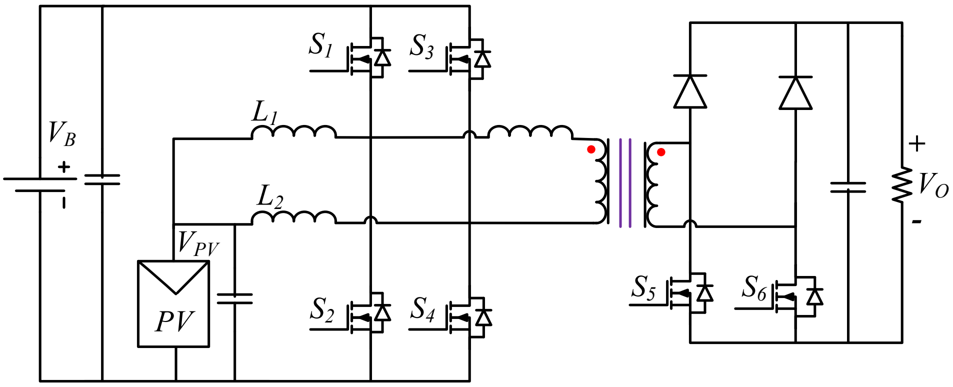

Fig. 4.13 : The pulse width modulation (PWM) plus secondary-side phase-shift (SSPS) controlled full-bridge three-port converter (FB-TPC) proposed in [120].

In [120], A pulse width modulation (PWM) plus secondary-side phase-shift (SSPS) controlled full-bridge three-port converter (FB-TPC) is proposed, as shown in Fig. 4.13 . The converter is formed by integrating an interleaved buck/boost converter and a secondary-side phase-shift full-bridge converter, where the primary active switches are shared. Zero voltage switching ZVS has been achieved for both primary and secondary side, and the power can transfer between any two ports easily. An application for the proposed topology has been implemented in [70] to design a distributed DC grid for PV applications.

4.1.3 Isolated Converter

The isolation converter is based on a traditional full-bridge or half-bridge converter [109,67]. All the ports in the isolated converter are connected with a high-frequency multi-winding transformer. Thus, all ports in this topology are fully galvanic isolated. This topology allows bidirectional power flow between the ports if the bidirectional power switches are used. Nevertheless, the number of components is high. Each port needs its component, so it is hard to share some of the. A high voltage gain

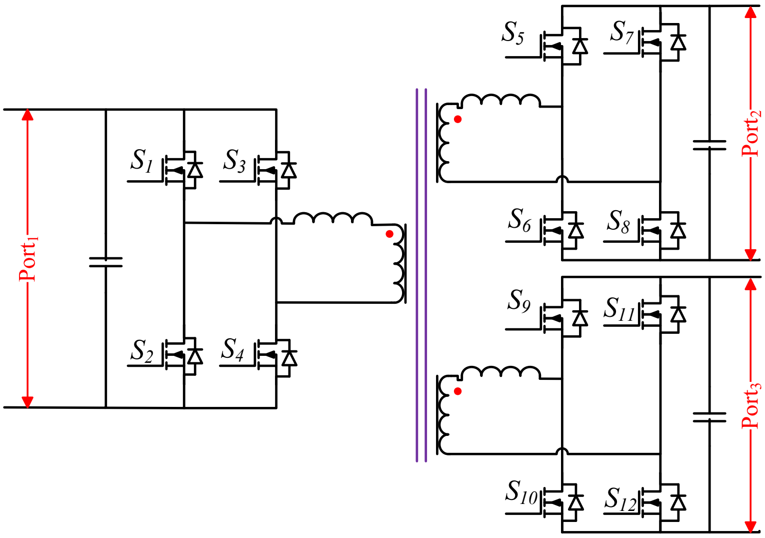

Fig. 4.14 : Isolated triple-active-bridge converter full bridge [122].

can be achieved be increasing the turns ration of the high-frequency transformer.

Fig. 4.14 shows triple full-bridge DC-DC converter [122]. The proposed circuit is able to achieve a bidirectional power flow in all ports. By using a three-winding high-frequency transformer with different turns ratios, it is easy to match different voltage levels at each port. The phase shift control is used to control the power flow. Similar work has been done in [102]. In addition to the previous work, ZVS is extended by proposing a simple and effective duty ratio control method. In order to achieve higher switching frequencies and lower losses, two series resonant tanks have been added to the full-bridge structure [63].

The authors of [101] proposed a three-port triple-half-bridge DC-DC converter where one of the three half-bridge is a boost half-bridge topology. The half-bridges are coupled by using a high-frequency transformer that helps to achieve high voltage and offer galvanic isolation. The current-fed topology which can be regulated as a boost converter offers less current ripple compared to the voltage-fed topology. A

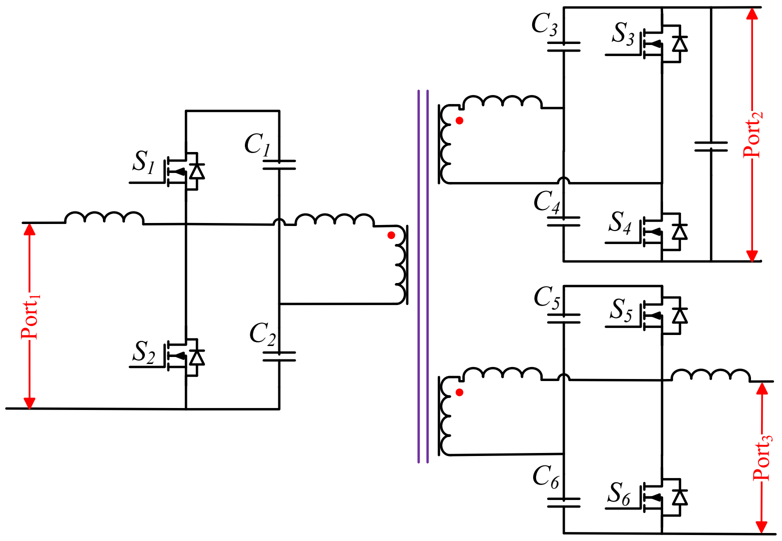

Fig. 4.15 : Isolated triple-active-bridge converter half bridge [109, 67].

high transformer efficiency, as a result, boosts the voltage, reduces the transformer current requirement and offers a current mode control to achieve more control flexibility. The authors of [109, 67] employ two current-fed topologies on the low voltage side to interface low voltage devices such as low voltage battery and ultracapacitor as shown in Fig. 4.15.

4.1.4 Comparison of Different Multiport Converters

Each group of MPC has its advantages and disadvantages. In an isolated and partly isolated multiport converter, all ports are galvanic isolated from each other to prevent shock hazards, and it is very easy to achieve a ZVS. Also, due to the use of a high-frequency transformer, it is more likely to achieve a high voltage regulated ratio. However, due to the use of a high-frequency transformer and more switches in full and half-bridge, the converter's weight, size and magnetic losses increases, so the efficiency and power density reduces. There is often a trade-off between the advantages and the disadvantages.

The non-isolated multiport converter has some disadvantages, the voltage regulated ratio is limited by the duty cycle of the converter, and it is hard to achieve ZVS. On the other hand, the non-isolated converter is more beneficial than the isolated converter because of its high efficiency, a high power density and low cost due to its shared components. The drawback of the non-isolated converters could be mitigated by using a coupled inductor, switched-capacitor, switched-inductor and multiplier circuit.

4.2 Summary

In this Chapter, a review of MPC topologies for integrating PV with ESS is presented. Based on the literature review, the non-isolated topologies are cost-effective, high efficient, and useful for low power applications. Whereas isolated and partly-isolated topologies are suitable for high power applications.Base on the aforementioned conclusion, non-isolated converter is the best topology to integrate the PV with ESS, and it will be considered in the following two Chapters.

Chapter 5

A Reconfigurable Three-Port DC-DC Converter for Integrated PV-Battery System

5.1 Overview

According to the conducted literature review and the findings in Chapter 2 and 3, the PV power is limited to the available solar energy which is uncontrolled in nature. In reality, the MPPT algorithms are used to track the maximum possible power from the exerted solar energy. There is no solution that can solve the solar energy intermittency better than the energy storage system (ESS). According to [44], the battery required low maintenance and its cost becomes reasonable. Based on these reasons, the battery integrated PV module becames very attractive as reviewed in [14, 6].

In addition to solving the intermittency issue, the PV-battery system can store the unused generated solar power that was generated during the peak generation time, so as to be used during no generation instants or peak hours making the solar energy system more reliable and a steady source of power. Having the battery integrated within the PV module during the manufactory process lead to installation cost reduction as the installation cost of the solar system is considered high [106]. In addition, the EES can resolve many of the implementation challenges of PV generation and enables more effective grid management [26]. The authors in [107] discuss the advantages and disadvantages of PV-battery integrated modules and evaluate a physical integration approach via a simple thermal resistance model. The advantages of PV-battery integrated modules are plug-n-play, installation cost reduction, flexible AC/DC loads connections, space-saving and modularity. The challenges are optimizing various parameters of PV module, battery and the cooling system including weight, size, thermal and cost. Different PV-battery integrated modules approaches are evaluated based on efficiency, flexibility and implementation cost. The order of integration is glass, cell, Tedlar, upper casing, battery and lower casing. The glass is used to reflect some irradiation. The Tedlar is used to resist the UV radiation and protect against weather and moisture. A simulation of the thermal model is conducted. The results showed a high temperature above the 320K recommended operating condition. An air gap is inserted to lower the overall temperature significantly.

In this chapter, a new non-isolated three-port converter is proposed for stand-alone PV-battery powered applications such as DC motor and LED lighting. By adding one switch and a coupled inductor to the circuit proposed in [37], the converter is able to achieve MPPT, battery management and output voltage regulation simultaneously by controlling two switches only. In [37], the converter is only able to achieve MPPT, and the battery serves as an automatic buffer according to the difference between PV and Output powers. Moreover, in this chapter, the coupled inductor is used to extend the output voltage to a higher level. The chapter is organized as follows: In Section 5.2, the proposed circuit is introduced and the operation mode is analyzed. In Section 5.3, design considerations of the converter are discussed. In Section 5.4, the experimental results are explained followed by the conclusion in Section 5.5.

5.2 Operation Principle

5.2.1 Proposed Circuit

The proposed three-port converter, shown in Fig. 5.1, has three ports, namely a unidirectional input port, a bi-directional battery port and an output port. S_1

and S_2 are power switches. S_2 is formed by two MOSFETs connected back-to-back to implement a bidirectional switch. Diode D_1 and coupled winding L_S form the flyback output part. C_{PV}, C_1 and C_2 are the filter capacitors at the PV panel, V_1 and V_2 respectively. A coupled inductor formed by L_P and L_S is used as an intermediate storage element for the energy transfer among the three ports. The turns ratio of the designed coupled inductor is N_P/N_S where $N_P < N_S$.

The main input port V_{PV} is connected to a photovoltaic module that has a blocking diode. The bi-directional battery port V_B is connected to a battery storage system so that it can be used to either provide a high voltage gain due to its series configuration with the input port or assist output regulation in response to the intermittency of PV power. Meanwhile, the proposed circuit is able to achieve MPPT, manage battery charging/discharging and regulate the output voltage.

The following conditions are assumed for steady-state analysis:

- The output capacitors C_1 and C_2 are large enough to smooth the output voltage.

- No conversion loss and all components are ideal. The internal resistor of the battery is neglected.

5.2.2 Operation Modes

According to the above assumption and the circuit diagram shown in Fig. 5.1, the input PV power equals the power delivered to the battery plus the power transferred to the load, $P_{PV} = P_B + P_O$ and the PV current equals the primary inductor current plus the battery current, $i_{PV} = i_{LP} + i_B$. Also, the regulated output voltage equals the sum of the voltages on the output series capacitors, $V_O = V_1 + V_2$.

The power flow among the ports in the proposed three-port converter has six operating modes. These modes are listed below:

1. Single-input single-output (SISO) PV-battery mode: This mode is active when the PV module charges the battery at no-load condition, as depicted in Fig. 5.2(a).
2. Single-input single-output (SISO) PV-load mode: This mode is active when the PV module supplies power to the load assuming the battery is not connected, as depicted in Fig. 5.2(b).

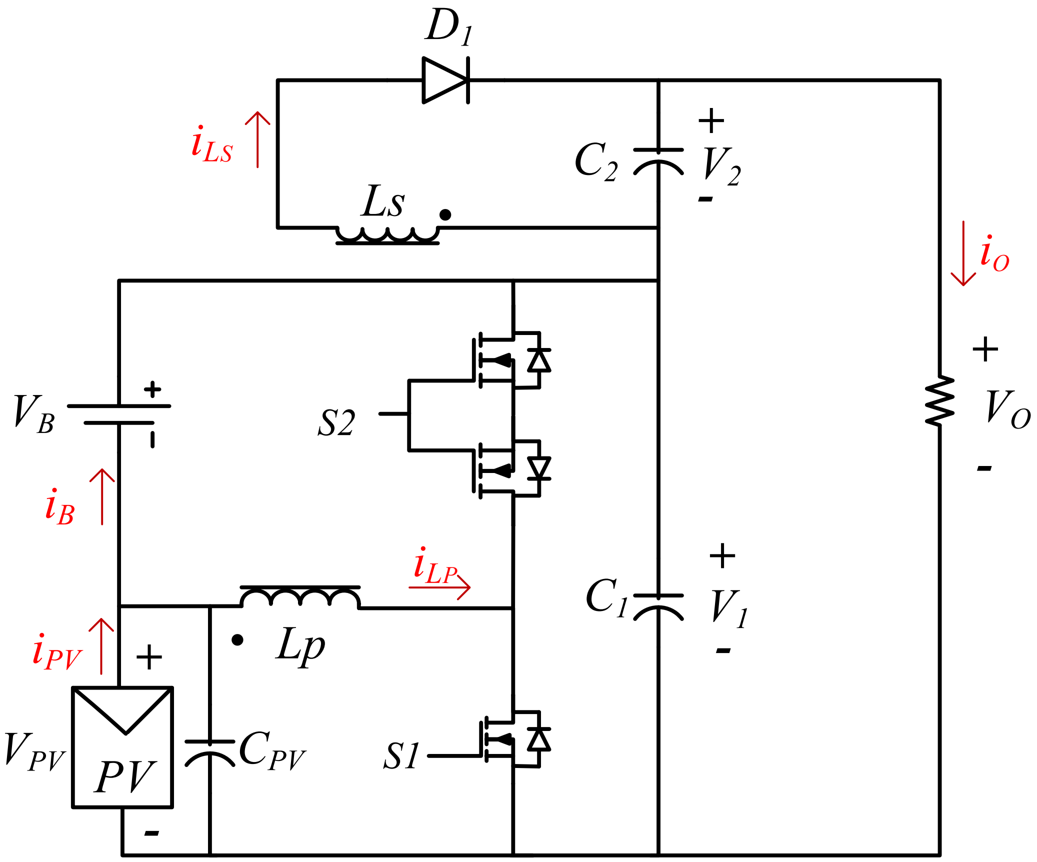

Fig. 5.1 : Proposed integrated PV-battery converter topology.

3. Single-input single-output (SISO) battery-load mode: This mode is active only when the battery supplies power to the load. In this mode, the PV module is either shaded or not supplying power (at night time for instance), as depicted in Fig. 5.2(c).

4. Dual-input single-output (DISO) mode: This mode is active when the PV module and the battery supply power simultaneously to the load, as depicted in Fig. 5.2(d).

5. Single-input dual-output (SIDO): This mode is active when the PV module

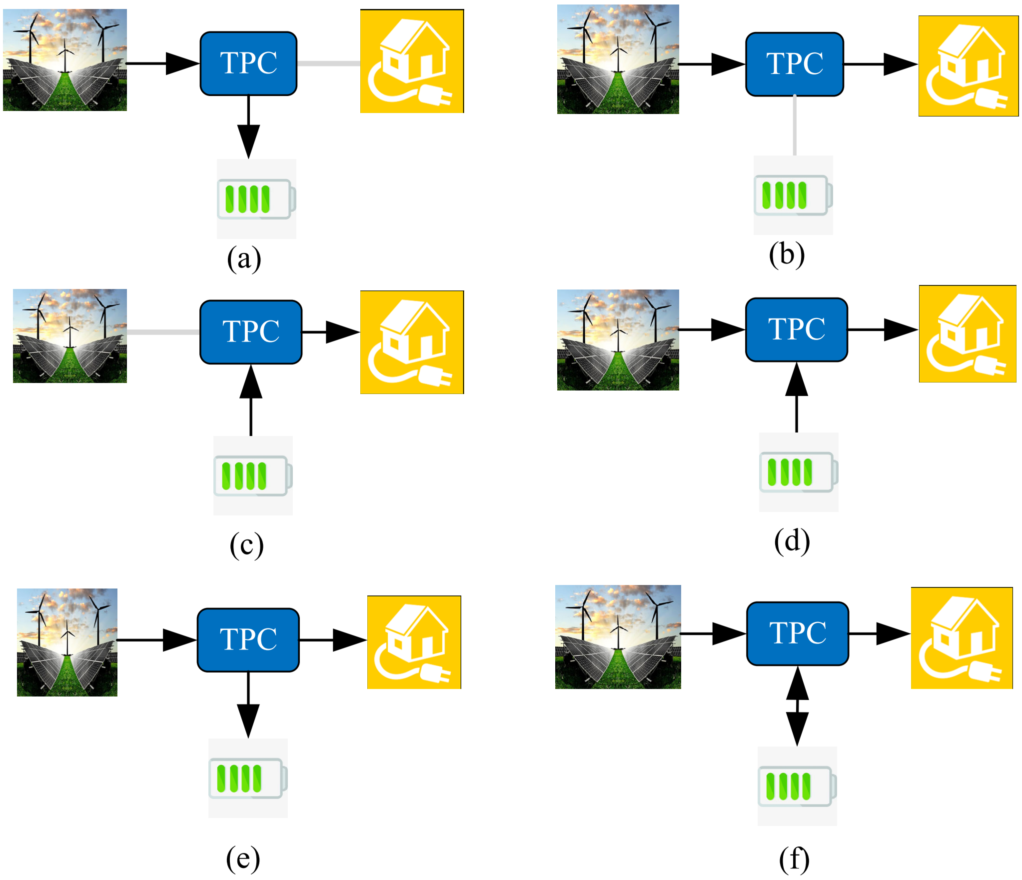

Fig. 5.2 : Power flow TPC and operation modes: (a) SISO PV-battery mode. (b) SISO PV-load mode. (c) SISO battery-load mode. (d) DISO mode. (e) SIDO mode. (f) DIDO mode.

supplies power to the load. The unused power generated from the PV is stored at the battery as depicted in Fig. 5.2(e).

6. Dual-input dual-output (DIDO): This mode is active when the PV supplies power to the load, and the power generated by the PV panel is equal to the power consumed by the load. In other words, although there is an instantaneous power mismatch between the PV and the load, over a certain period of time, the average PV power and the average load power are equal. This mode is depicted in Fig. 5.2(f).

5.2.3 Steady-State Analysis

1. SISO PV-battery mode: In this mode, only two ports are active, namely the input and the battery ports. S_1 and S_2 are operating in a complementary mode, and the duty cycle is given as $d_2 = 1 - d_1$. The power generated by the PV module is used to charge the battery. The combination of V_{PV}, L_P, S_1, S_2 and V_b is considered as a buck-boost converter. This operating mode has two switching states as shown in Fig. 5.3 and discussed below:

   Switching mode I $[t_0 < t < t_1]$: S_1 is turned ON while S_2 is turned OFF. The primary inductor, L_P, starts to charge by the input source V_{PV} and the battery V_B. D_1 is reverse-biased due to the polarity of the secondary winding of the coupled inductor, so no current flows at the secondary inductor. By applying KVL (Kirchhoff's Voltage Law) for the mesh the voltage at the inductor given by $V_{L_P} = V_{PV}$. This mode ends when S_1 turns OFF at $t = t_1$.

   Switching mode II $[t_1 < t < t_2]$: S_1 is turned OFF while S_2 is turned ON. The primary inductor, L_P, starts to discharge and the battery current increases. By applying KVL, the voltage on the inductor given by $V_{L_P} = V_{PV} - V_1$. By using voltage-second balance, the regulated voltage V_1 is obtained in (5.1). By applying KVL for the mesh with V_{PV}, V_B and V_{C_1} the battery

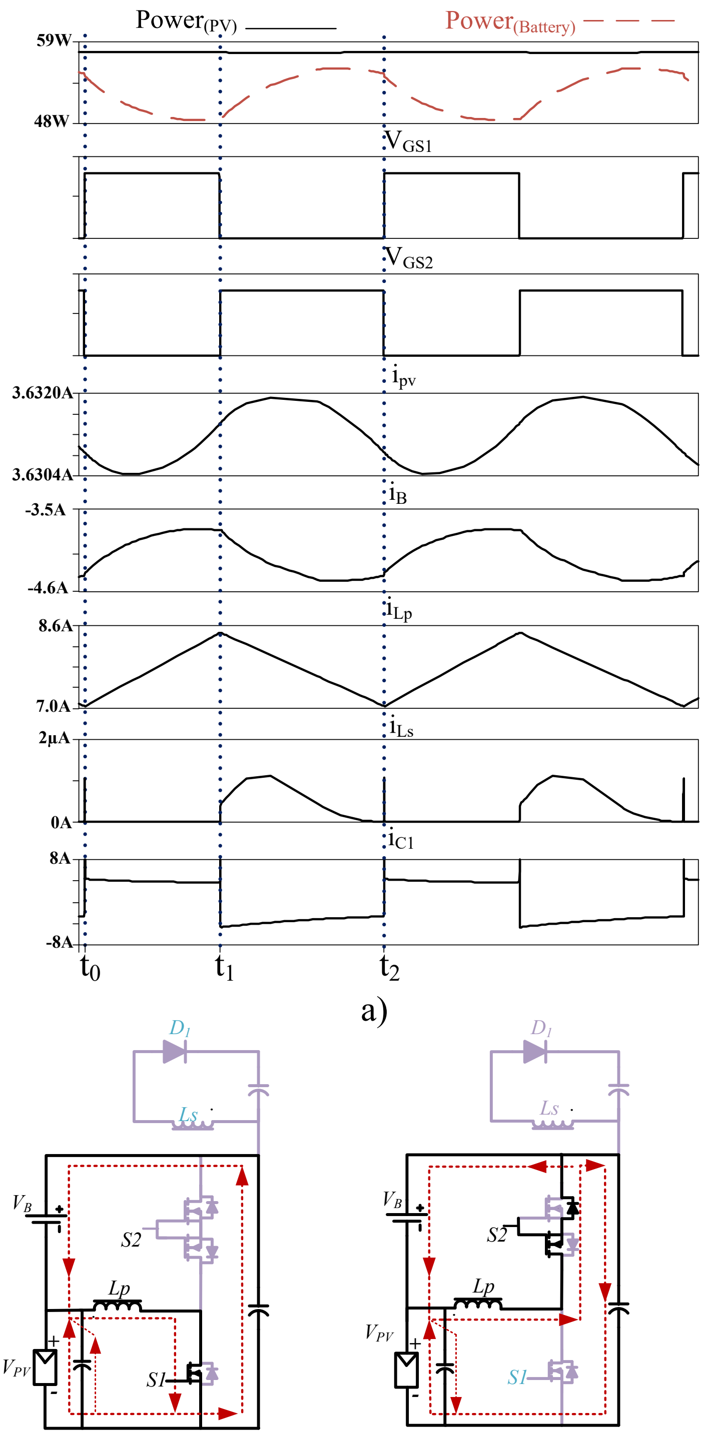

Fig. 5.3 : SISO PV-battery mode under no-load condition: (a) Key switching waveforms. (b) Equivalent circuits and corresponding current flows.

voltage is given as $V_B = V_1 - V_{PV}$. By substituting this relationship in (5.1), the regulated battery voltage is given in (5.2). When S_2 turns OFF at $t = t_2$, this mode ends.

$$V_1 = \frac{V_{PV}}{1 - d_1} \tag{5.1}$$

$$V_B = \frac{d_1}{1 - d_1} V_{PV} = \frac{d_1}{d_2} V_{PV} \tag{5.2}$$

2. SISO PV-Load mode: In this mode, only two ports are active; the PV and the output ports. The battery port is disconnected. The combination of V_{PV}, L_P, S_1, S_2 and C_1 is considered as a boost converter while the combination of $V_{PV}, L_P, L_s, S_1, S_1, D_1$ and C_2 is a flyback converter. The switching waveforms are shown in Fig. 5.4 and discussed as follows:

   Switching mode I $[t_0 < t < t_1]$: S_1 is turned ON while S_2 is OFF. The primary inductor, L_P, starts to charge. D_1 is reverse-biased due to the polarity of the secondary winding of the coupled inductor. The voltage across the inductor is given by $V_{L_P} = V_{pv}$. This mode ends when S_1 turns OFF at $t = t_1$.

   Switching mode II $[t_1 < t < t_2]$: S_2 is turned ON while S_1 is still OFF. The primary inductor, L_P, starts to discharge. The diode D_1 is conducted then the energy stored in the coupled inductor is transferred to the load. By applying KVL for the mesh, the voltage on the inductor is given as $V_{L_P} = V_{PV} - V_1$. When the inductor current reaches zero at $t = t_2$, this mode ends.

   Switching mode III $[t_2 < t < t_3]$: In this switching mode, there is no change in the switching status. Nevertheless, the current direction will be reversed on the primary inductor. By applying KVL for the mesh, the voltage on the inductor is given as $V_{L_P} = V_{PV} - V_1$. This switching mode ends when S_2 turns OFF at $t = t_3$.

   By using voltage-second balance, the voltages for this mode are given as

$$V_1 = \frac{V_{PV}}{1 - d_1} \tag{5.3}$$

$$V_2 = \frac{N_S}{N_P}\frac{d_1}{d_2}V_{PV} \tag{5.4}$$

$$V_O = V_1 + V_2 = \frac{1 + \frac{N_S}{N_P}d_1}{d_2}V_{PV} \tag{5.5}$$

3. SISO Battery-Load mode: In this mode, only two ports are active, namely the battery and the output ports. The combination of $V_B, L_P, S_1, L_S, D_1, C_1$ and C_2 is considered as a forward converter, and the switching waveforms are shown in Fig. 5.5 and discussed as follows:

   Switching mode I $[t_0 < t < t_1]$: S_2 is turned ON since S_1 is always OFF. The primary inductor, L_P, starts to charge. D_1 is forward-biased due to the polarity of the secondary winding of the coupled inductor, then the current flows at the secondary inductor loop. The battery current starts to increase to supply more current to the load. The voltage at the inductor is given by $V_{L_P} = -V_B$. This mode ends when S_2 turns OFF at $t = t_1$.

   Switching mode II $[t_1 < t < t_2]$: In this switching mode, switch S_2 is turned OFF while S_1 is still OFF. The primary inductor, L_P, starts to discharge then the battery current starts to decrease. The current will flow through the antiparallel diode of S_1. The voltage on the inductor is given as $V_{L_P} = V_1 - V_B$. When S_2 switches ON at $t = t_1$, this mode ends. By using voltage-second balance the voltages V_1, V_2 and V_O for this mode are given by

$$V_1 = \frac{V_B}{1 - d_2} \tag{5.6}$$

$$V_2 = \frac{N_S}{N_P}V_1(1 - d_2) \tag{5.7}$$

$$V_O = \frac{N_P V_B + N_S V_1 (1 - d_2)^2}{N_P(1 - d_2)} \tag{5.8}$$

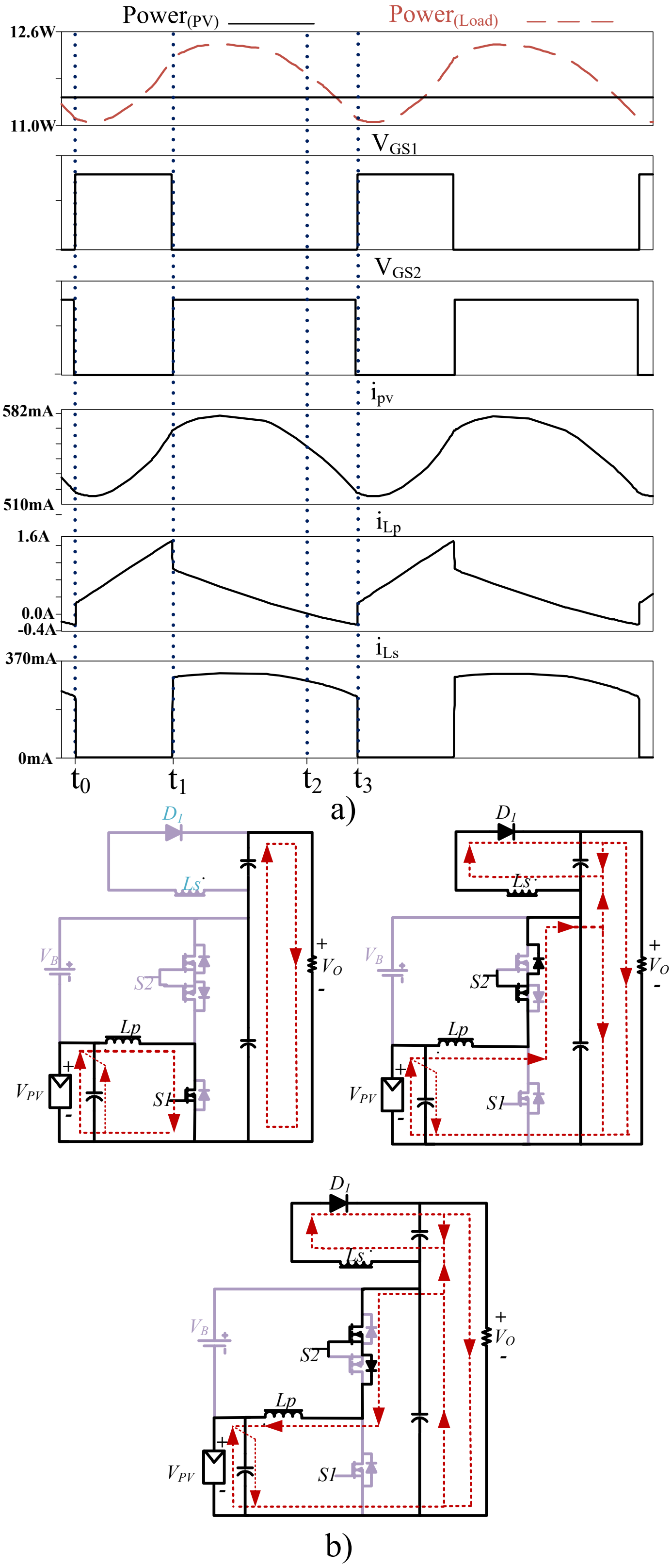

Fig. 5.4 : SISO PV-load mode: (a) Key switching waveforms. (b) Power flow.

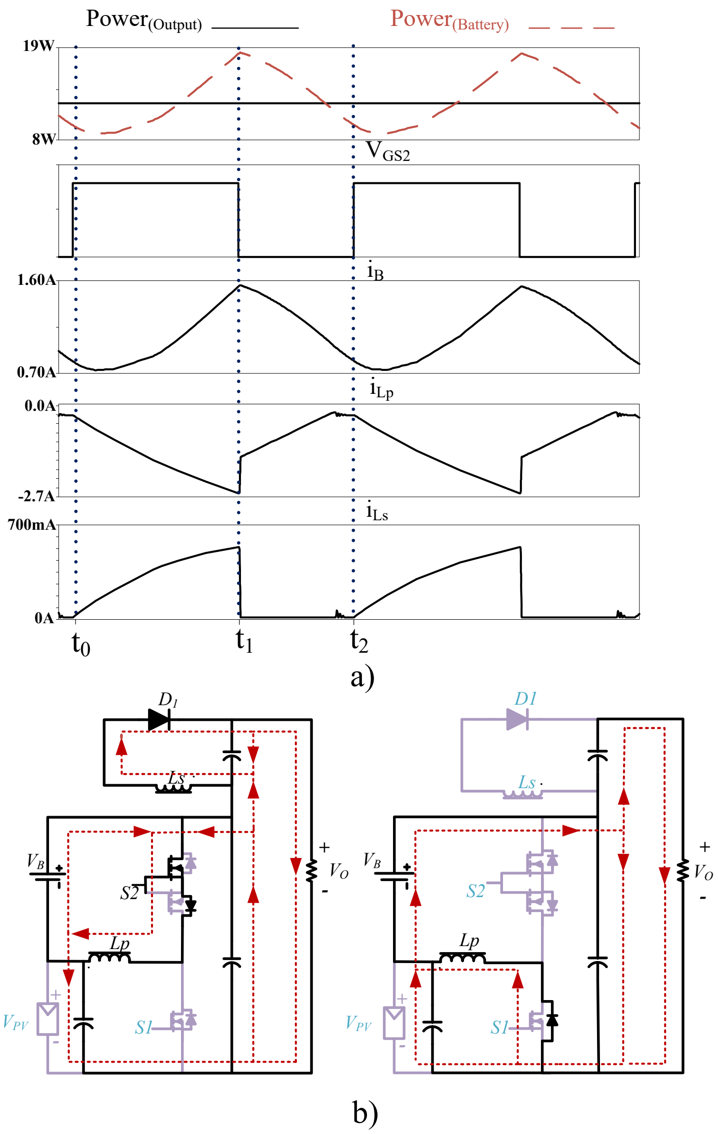

Fig. 5.5 : SISO battery-load mode: (a) Key switching waveforms. (b) Power flow.

4. DISO mode: In this mode and the following two modes, three assumptions are made. The combination of $V_{PV}, L_P, L_S, S_1, D_1$ and C_2 is considered as a flyback converter, the combination of V_{PV}, L_P, S_1, S_2 and V_b is considered as a buck-boost converter and the combination of V_{PV}, L_P, S_1, S_2 and C_1 is considered as a boost converter. All the ports in these modes are active. The only difference is the current flow of the battery port. Due to the insufficient input PV power, the current will be drawn from the battery to supply the load. The switching waveforms for DISO are shown in Fig. 5.6 and discussed as follows:

   Switching mode I $[t_0 < t < t_1]$: S_1 is turned ON while S_2 is turned OFF. The primary inductor, L_P, starts to charge. D_1 is reverse-biased due to the polarity of the secondary winding of the coupled inductor, then no current flows at the secondary inductor loop. The battery current starts to decrease as the primary inductor draws more current from the PV module. By applying KVL, the inductor voltage is given as $V_{L_P} = V_{PV} = V_1 - V_B$. This mode ends when S_1 turns off at $t = t_1$.

   Switching mode II $[t_1 < t < t_2]$: In this switching mode, switch S_2 is turned ON while S_1 is turned OFF. The primary inductor, L_P, starts to discharge. By applying KVL, the voltage on the inductor is given as $V_{L_P} = -V_B = V_{PV} - V_1$. When the primary inductor current reaches zero at $t = t_2$, this mode ends.

   Switching mode III $[t_2 < t < t_3]$: This switching mode is similar to the previous one, but the current direction at the inductor will be reversed, so the current at the battery port will increase. The voltage on the inductor has the same value of the previous switching mode. When S_2 switches OFF at $t = t_3$, this mode ends.

   By using voltage-second balance, the regulated voltages V_1, V_2 and V_O for this mode is given in (5.3), (5.4) and (5.5) respectively. Also, the relation between

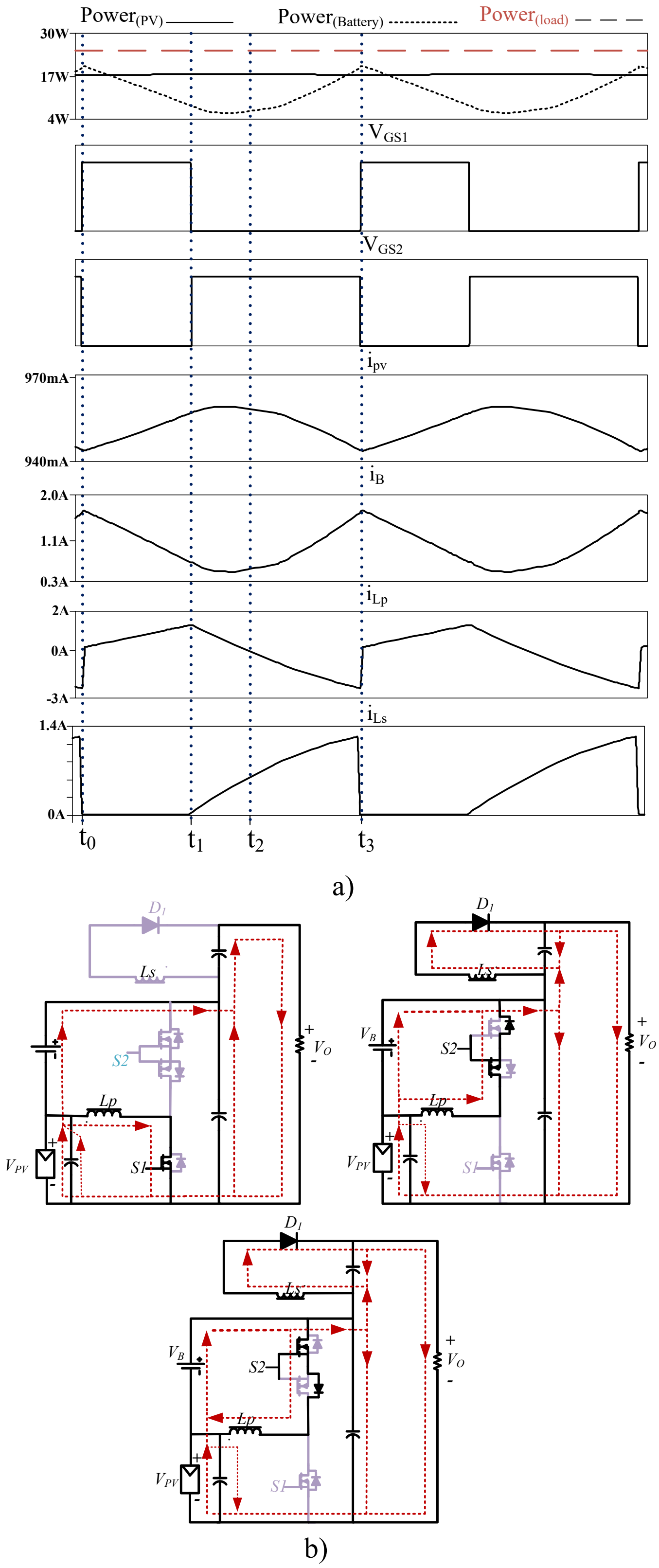

a)

b)

Fig. 5.6 : DISO mode: (a) Key switching waveforms. (b) Power flow.

the voltage on the battery port and V_1 is derived in (5.9).

5. SIDO mode: In this mode, the input PV power is greater than the output power, so some power will be stored in the battery. The switching waveforms are shown in Fig. 5.7 and discussed as follows:

   Switching mode I $[t_0 < t < t_1]$: S_1 is turned ON while S_2 is turned OFF. The primary inductor, L_P, starts to charge. D_1 is reverse-biased due to the polarity of the secondary winding of the coupled inductor, then no current flows at the secondary inductor loop. The voltage at the inductor is given by $V_{L_P} = V_{PV} = V_1 - V_B$. This mode ends when S_1 turns OFF at $t = t_1$.

   Switching mode II $[t_1 < t < t_2]$: S_2 is turned ON, and S_1 is turned OFF. The primary inductor, L_P, starts to discharge. By applying KVL for the mesh, the voltage on the inductor is given as $V_{L_P} = -V_B = V_{PV} - V_1$. When S_2 switches ON at $t = t_1$, this mode ends. V_1, V_2, V_B and V_O for this mode are given in (5.3), (5.4), (5.9) and (5.5) respectively.

$$V_B = V_1 d_1 \tag{5.9}$$

6. DIDO mode: Fig. 5.8 shows the switching modes for this mode. In fact, this mode is a balanced mode between SIDO and DISO modes so the regulated voltages are the same as the previous DISO and SIDO. The switching modes are described as follows:

   Switching mode I $[t_0 < t < t_1]$: In this switching mode, switch S_1 is turned ON while S_2 is turned OFF. The primary inductor, L_P, starts to charge by the input source V_{PV}. D_1 is reverse-biased due to the polarity of the secondary winding of the coupled inductor. The battery current starts to decrease until it reaches zero at $t = t_1$ then this mode ends.

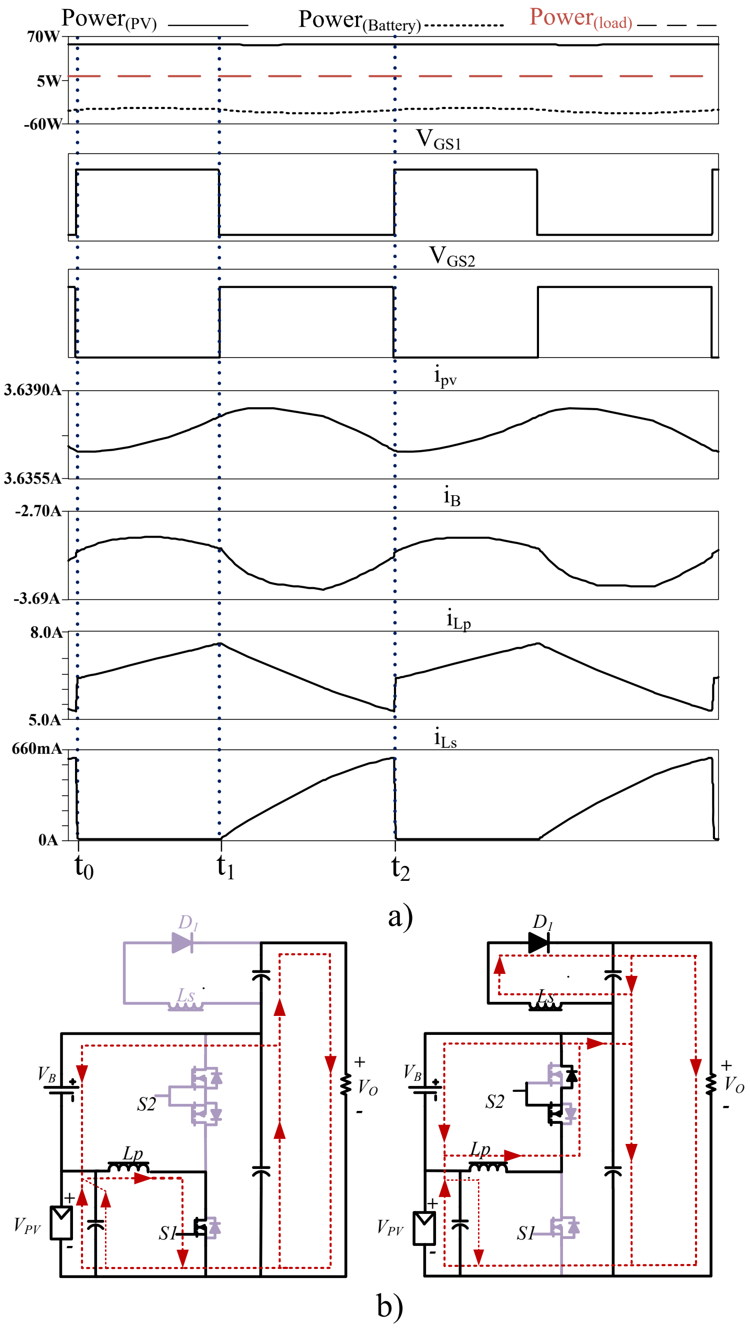

a)

b)

Fig. 5.7 : SIDO mode: (a) Key switching waveforms. (b) Power flow.

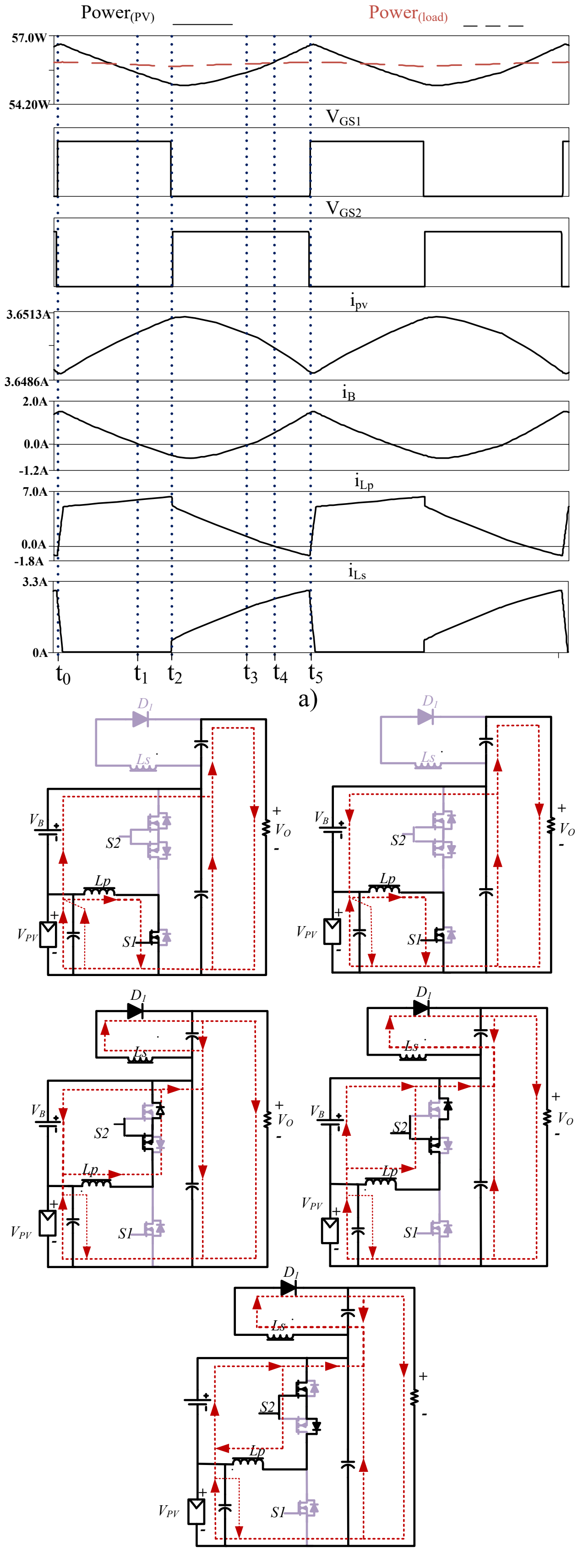

a)

b)

Fig. 5.8 : DIDO mode: (a) Key switching waveforms. (b) Power flow.

Switching mode II $[t_1 < t < t_2]$: S_1 remains ON, and S_2 is still OFF. The primary inductor keeps charging, and D_1 remains reverse-biased. Nevertheless, the battery starts charging, and this mode ends at $t = t_2$.

Switching mode III $[t_2 < t < t_3]$: S_1 is turned OFF while S_2 is turned ON. The primary inductor starts to discharge, and its energy flies to the secondary inductor and the battery at the same time. This mode ends at $t = t_3$ when the battery current equals zero.

Switching mode IV $[t_3 < t < t_4]$: S_1 remains OFF and S_2 remains ON. The battery starts to discharge in order to supply more power to the load. This mode ends at $t = t_4$ when the inductor current equals zero.

Switching mode V $[t_4 < t < t_5]$: S_1 remains OFF and S_2 remains ON. The current direction on the primary inductor will be flipped due to the direction of the current in the battery and the secondary inductor that is coupled with the primary. This mode ends at $t = t_5$.

5.3 Design Considerations

In this section, the design example will be discussed based on the following parameters:

$$V_O = 50 \text{ V}$$

$$V_{PV} = 18.5 \text{ V}$$

$$V_B = 12 \text{ V}$$

$$P_O = 20\text{-}80 \text{ W}$$

$$f_s = 50 \text{ kHz}$$

5.3.1 Duty Cycle Selection

The main design consideration is to select suitable values for d_1, d_2, n, L_P and L_S. The steady-state duty ratio for S_1 can be obtained from (5.2) as

$$d_1 = \frac{V_B}{V_B + V_{pv}} = \frac{12}{12 + 18.5} = 0.395 \tag{5.10}$$

Since S_1, which is the main switch, is responsible for MPPT and battery charging, its duty cycle should be selected carefully. In the present design, the battery port should operate within the range of 10.8-14.8 V for lead-acid battery. The maximum duty cycle $d_{1,max}$ is needed when the input voltage is at the MPP ($V_{MPP} = 18.5$ V), and the battery voltage is at the maximum value. Thus, $d_{1,max} = 0.45$. In fact, this maximum duty cycle is a key parameter for the battery charging control strategy in preventing damaging the battery due to overcharging.

5.3.2 Coupled Inductor Selection

V_1 can be obtained from (5.2) as

$$V_1 = \frac{V_{PV}}{1 - d_1} = \frac{18.5}{1 - 0.4} = 30.5V \tag{5.11}$$

As the output voltage of the proposed converter is given as $V_O = V_1 + V_2$ and the output voltage $V_O = 50$, $V_2 = 50 - 30.5 = 19.5V$. According to (5.4) and the calculated value for V_2, the turns ratio of the coupled inductor can be obtained as

$$\frac{N_S}{N_P} = n = \frac{d_2 V_2}{d_1 V_{PV}} = \frac{(1 - 0.395)19.5}{0.395 * 18.5} = 1.62 \tag{5.12}$$

The converter is designed to operate in continuous conduction modes (CCM). According to the steady-state analysis for DIDO mode, L_P can be given as

$$L_P > \frac{V_{lP} \triangle t}{\triangle i} > \frac{V_{PV} d_1 T_s}{2 i_{input}} > 18uF \tag{5.13}$$

By substituting the coupled inductor ratio and primary inductor value in (5.14) the secondary inductor should be four times the value of the primary inductor.

$$\frac{L_P}{L_S} = (\frac{N_p}{N_S})^2 \tag{5.14}$$

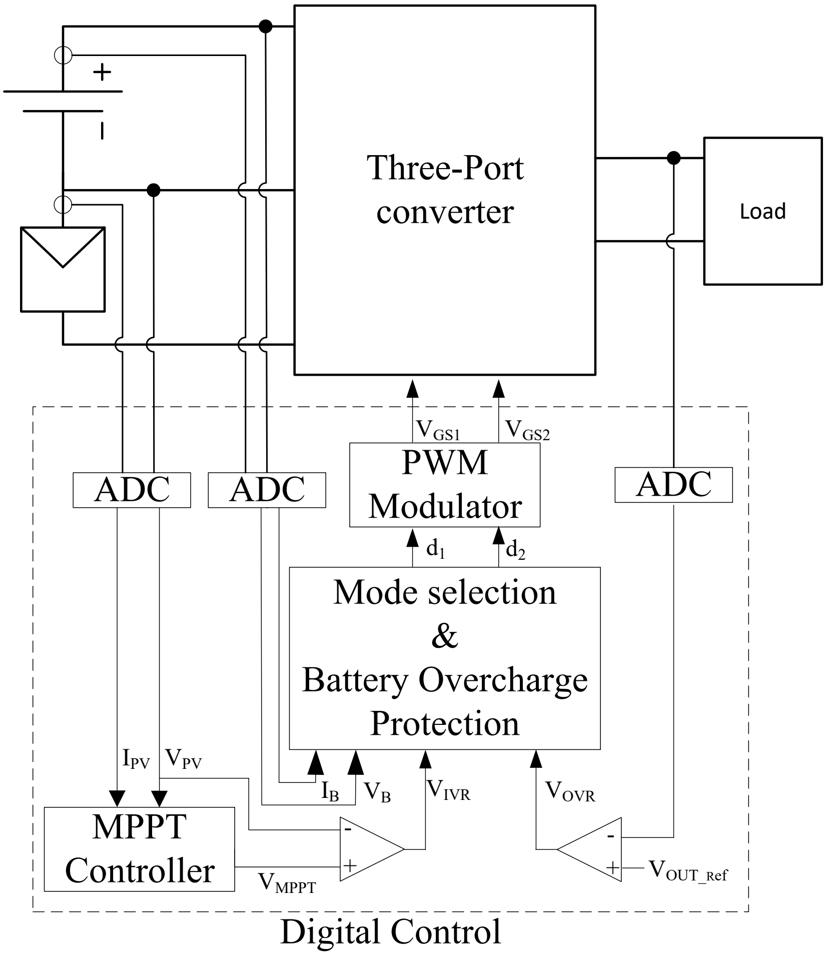

Fig. 5.9 : Control scheme of the proposed three-port converter.

5.3.3 Control Strategy

A Texas Instrument DSP controller (TMS320F28335) is used to control the power flow and generate PWM signals to drive the switches. The available solar power as well as the battery state of charge (SoC) determine the converter's operation modes. The control scheme, shown in Fig. 5.9, has three control loops that are used to control the proposed converter, namely the input voltage regulator (IVR), output voltage regulator (OVR) and battery voltage regulator (BVR).

The OVR is a simple PI voltage regulation loop used to regulate the output

Table 5.1 : Operation Modes Selections and Switches Operation Lookup Table

Modes	**Power Condition (W)**	**S1**	**S2**	**Active components**
SISO PV-battery	$P_{PV} = P_B, P_O = 0$	PWM1 (MPPT and BVR)	PWM2 (Complementary mode)	S_1, S_2, C_1, and L_p
SISO PV-load	$P_{PV} = P_O, P_B = 0$	PWM1 (MPPT)	PWM2 (OVR)	S_1, S_2, C_1, C_2, L_P and L_S
SISO battery-load	$P_B = P_O, P_{PV} = 0$	0	PWM2 (OVR)	S_2, C_1, C_2, L_P and L_S
DISO	$P_{PV} + P_B = P_0$	PWM1 (MPPT and BVR)	PWM2 (OVR)	S_1, S_2, C_1, C_2, L_P and L_S
SIDO	$P_{PV} = P_0 + P_B$	PWM1 (MPPT and BVR)	PWM2 (OVR)	S_1, S_2, C_1, C_2, L_P and L_S
DIDO	$P_{PV} + P_B = P_0 + P_B$	PWM1 (MPPT and BVR)	PWM2 (OVR)	S_1, S_2, C_1, C_2, L_P and L_S

voltage. The input PV port voltage and P&O algorithm are maintained by using an IVR loop to get the maximum input PV power. To prevent the battery from overcharging, a BVR loop is used. In fact, this loop is only active when the battery is fully charged at (SISO) PV-battery or SIDO mode. As the battery port is connected in series with the PV port, the battery cannot be disconnected. As a result, the control variable d_1 will operate away from the MPPT to reduce the power generated from the PV module. Thus, the converter changes the operation mode not to charge the battery. The mode selection flow chart is shown in 5.10, and duty cycle of each power switch are summarized in Table 5.1.

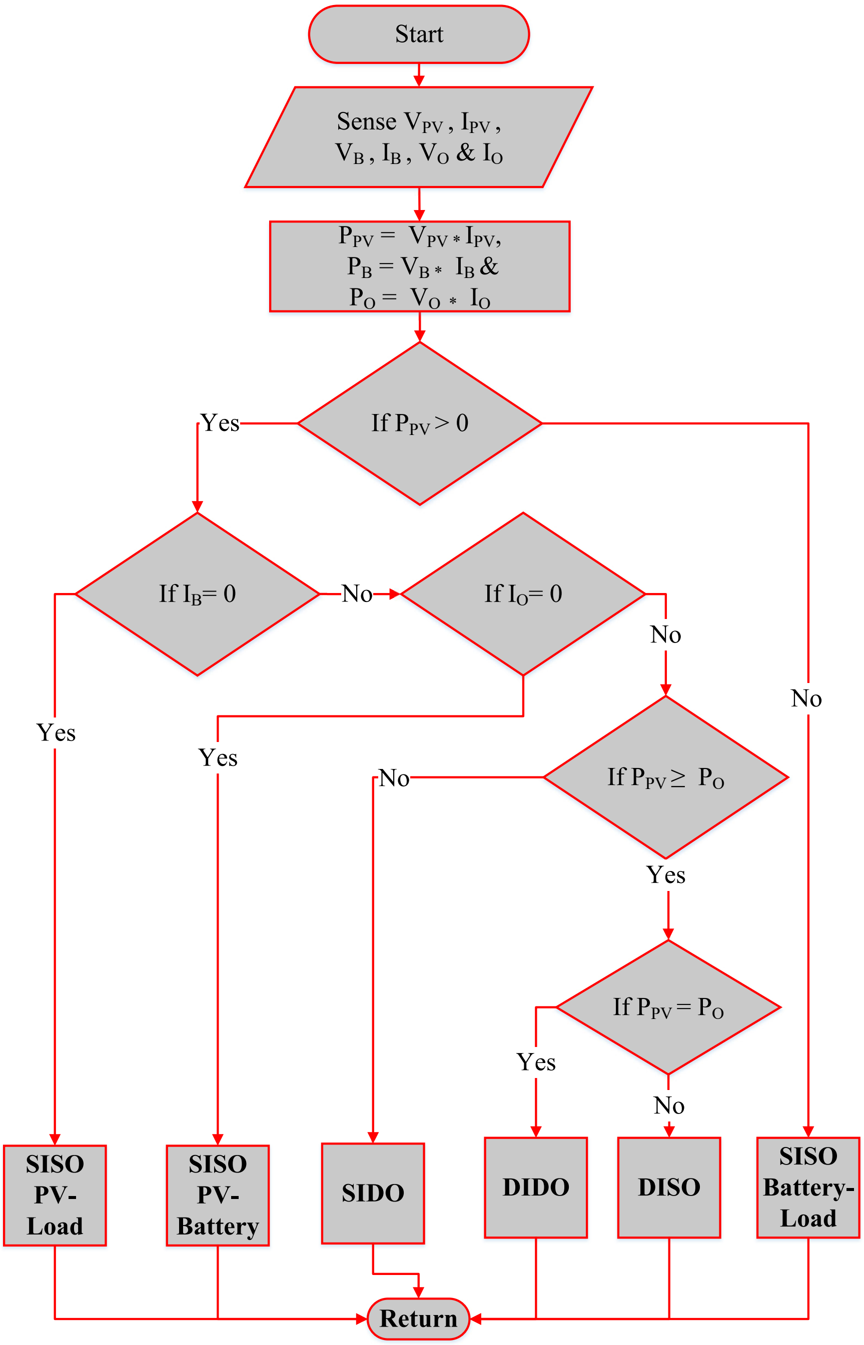

Fig. 5.10 : Flowchart of the operation mode selection algorithm.

5.3.4 Power Device Voltage Stress Analysis

Assuming that the ports voltage and the voltage on the capacitors C_1 and C_2 are constant, the voltage stress on the switching devices are given as below.

$$\begin{aligned} V_{S1} &= V_1 \\ V_{S2} &= V_{PV} + V_B \\ V_{D1} &= V_o \end{aligned} \tag{5.15}$$

5.3.5 Capacitor Design

In order to obtain 98% utilization efficiency for PV module, the voltage ripple at the input port should be below 8.5% of the MPP voltage V_{MPP} [60]. According to this result, the minimum value of the filter capacitor of PV panel can be determined as

$$C_{PV} = I\frac{dt}{dv} = I_{MPP}\frac{d_{1,max}}{0.085V_{MPP}f_s} \tag{5.16}$$

To design the output capacitor for any converter, the hold-up time requirement for step-load should be considered. The minimum output voltage ripple must remain under a suitable value, typically 1% of the output voltage. A nonzero time,τ, is required to get back the load voltage to the study-state, and this duration is usually approximated as $1/(0.1f_s)$ [4]. According to these conditions, the value of the output capacitor should be greater than

$$C_{1,2} = I\frac{dt}{dv} = \frac{I_O}{0.01V_{1,2}(0.1f_s)} \tag{5.17}$$

5.4 Experimental Results

Initially, the proposed converter is simulated using LTSpice to verify its feasibility. A 60 W hardware prototype is built and tested in order to confirm the operation and evaluate the performance, as shown in Fig. 5.11. The values of the key parameters are given in Table 5.2.

A 60 W solar panel is used as a main source of power. The solar radiation emulated by using a set of artificial lights (500 W halogen light). A 12V, 12Ah lead-acid battery is connected to the bidirectional port (battery port) to store the unused power and to supply more power to the load when required to reduce

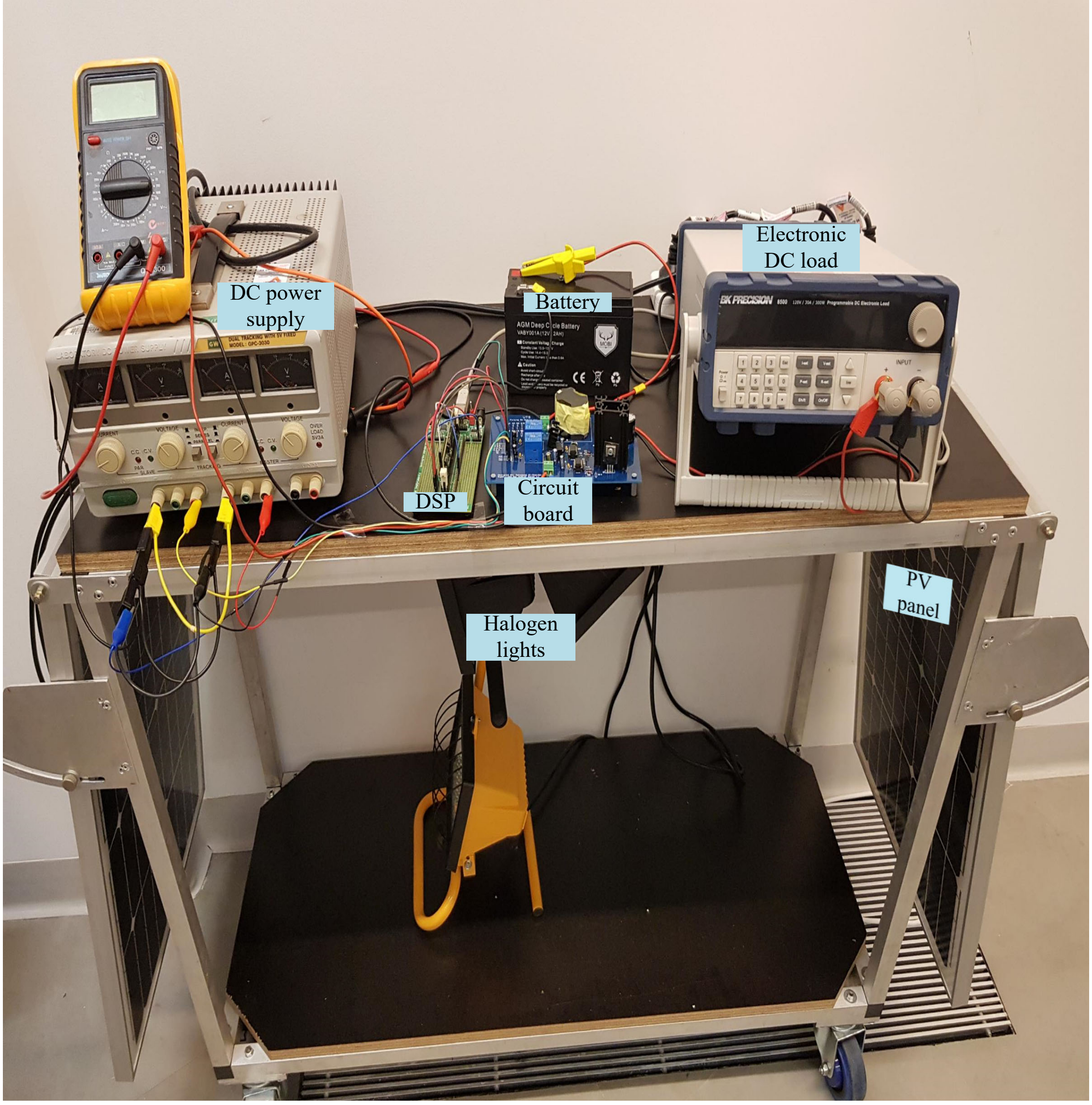

Fig. 5.11 : Laboratory prototype.

the intermittency effects. The output port is connected to a programmable DC electronic load to mimic the change in the power consumption.

The main waveforms of all modes are shown in Fig. 5.12. It is clearly illustrated that the output voltage is regulated at 50 V for all modes while the PV module

Table 5.2 : Components Details.

Component	Model/Value
Digital controller	TMS320F28335
Switching frequency	50 kHz
MOSFET	IRF540N
MOSFET driver for S_1	TC4426
MOSFET driver for S_2	IR2184PBF
D_1	MBR2035CT
Coupled inductor core	RM14/I-3C95
N_P/N_S	1/2
L_P	100 µH
L_S	400 µH
C_1&C_2	470 µF

voltage is regulated at around 18.5 V which is the voltage at the maximum power point (MPP) for the solar panel. The current direction is varied for each mode. In

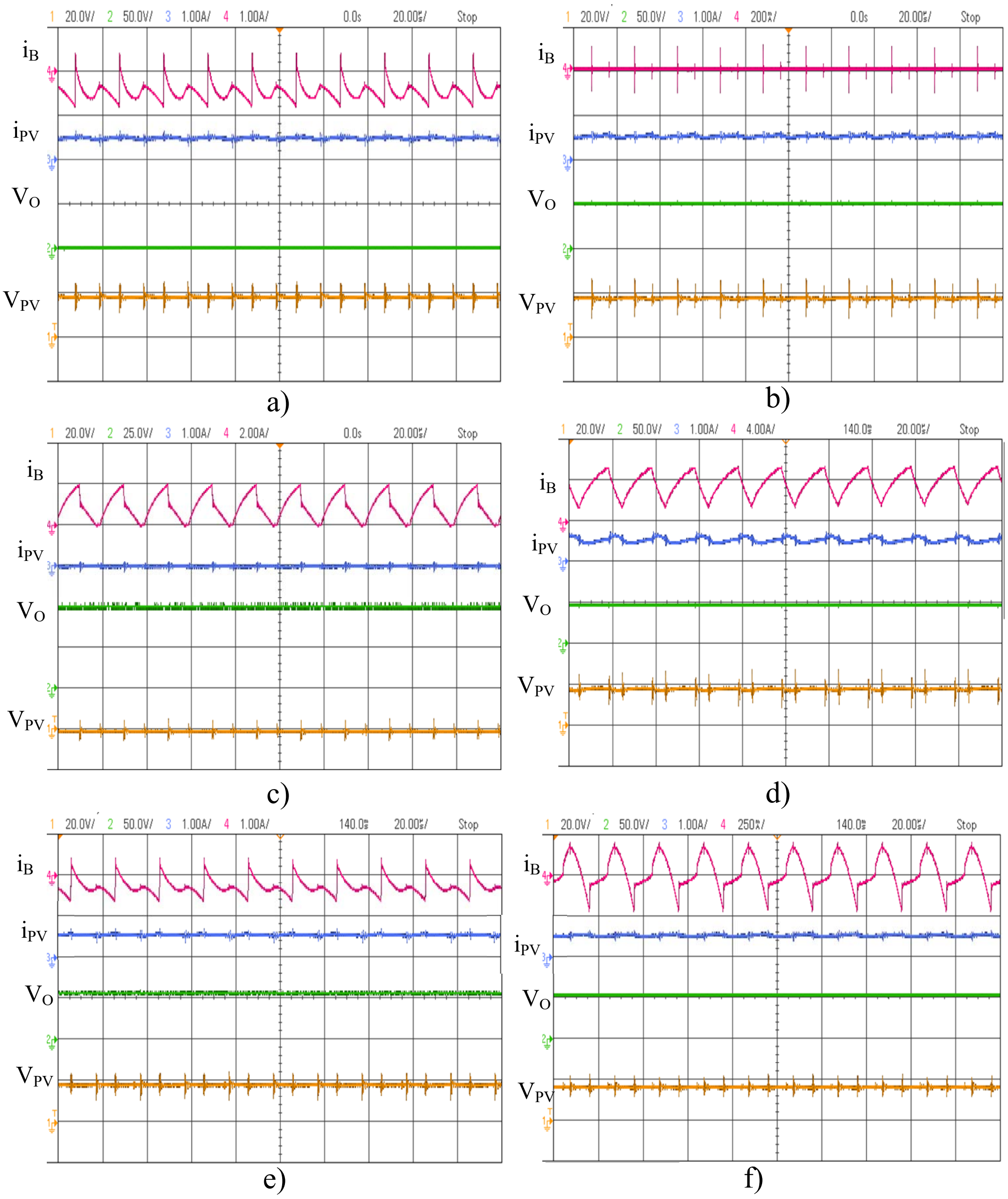

a) b) c) d) e) f)

Fig. 5.12 : Experiment result (waveforms): (a) SISO PV-battery mode. (b) SISO PV-load mode. (c) SISO battery-load mode. (d) DISO mode. (e) SIDO mode. (f) DIDO mode. [Time base: 20µs. V_{PV}: 20V/div. V_O: 50V/div for all mode except (c) V_O: 25V/div. i_{PV}: 1A/div. i_b: 1A/div, 200mA/div, 2A/div, 4A/div, 1A/div, 250mA/div respectively].

(SISO) PV-battery mode and SIDO mode, the current is negative indicating that the battery is charging. In (SISO) battery-load mode and DISO mode, the current is positive. This indicates that the battery is discharging. The battery current of the (SISO) PV-load mode equals zero because it acts as an open circuit while the average current of the DIDO mode equals zero because the input PV power equals the output power. It is noted that the battery current is highly pulsating. According to the literature, this is still a debatable and inconclusive matter. In [7], the authors show that a high pulsation current is considered as one of the promising solutions to get a fast battery charging. On the other hand, in [89], the authors show that it may reduce the life cycle of the battery as the internal resistor of the battery increases with the time if a high pulsating current is used. There have been other charging current patterns proposed with different degrees of effectiveness such as that in [21]. Nevertheless, if a constant current is preferred, it can be achieved easily by adding a passive filter (e.g. C, LC, etc.) in parallel with the battery or a shunt active filter (AF) to remove this harmonic current [45].

Fig. 5.13 shows the transient behaviour between different modes. It is observed that the output voltage is regulated at a constant level. Fig. 5.13(a) shows the transient response when the operation mode changes from DISO to SISO battery-load then goes back to DISO after partial shading is applied on the PV module. It is illustrated that the input current generated from the PV module has reduced. The battery current increases to compensate the amount of current that was generated from the PV module to maintain the output load operating at the same voltage and power. Fig. 5.13(b) shows the transient response when the operation mode changes from DIDO to SISO battery-load then goes back to DIDO after the PV module is fully shaded to emulate the night time. Fig. 5.13(c) shows the transient response when the operation mode changes from DIDO to SISO battery-load. Fig. 5.13(d) shows the transient response for three scenarios: SISO Battery-load to DISO;

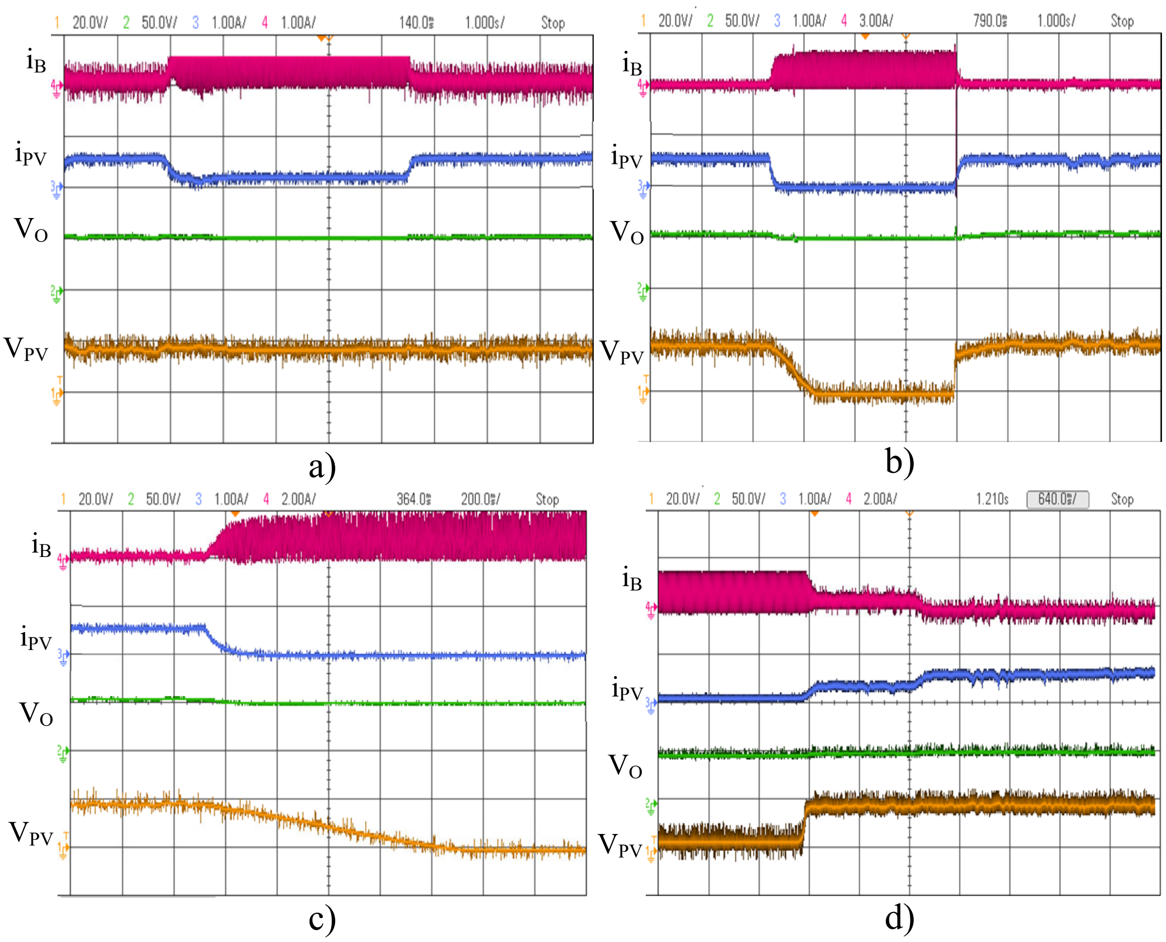

Fig. 5.13 : Experiment result (Transient response) between modes: (a) DISO → SISO battery-load → DISO. (b) DIDO → SISO battery-load → DIDO. (c) DIDO → SISO battery-load. (d) SISO Battery-load → DISO radiation I → DIDO. [V_{PV}: 20V/div. V_O: 50V/div. i_{PV}: 1A/div. i_b: 1A/div, 3A/div, 2A/div, 2A/div respectively].

insolation equals 250 W/m^2; then to DIDO mode.

Based on the experimental results, the average efficiency of the proposed converter varies between 94% for SISO PV-load mode, 93.09% for SISO PV-battery mode (when the battery stat-of-charge SoC equals 60%), 90.75% for SISO battery-load mode, 95.49% for DISO, 94.26% for SIDO and 95.04% for DIDO. Fig. 5.14 shows the efficiency curves for the main operating modes at various output power values. The battery SoC is maintained around 60% in order to achieve a fair comparison.

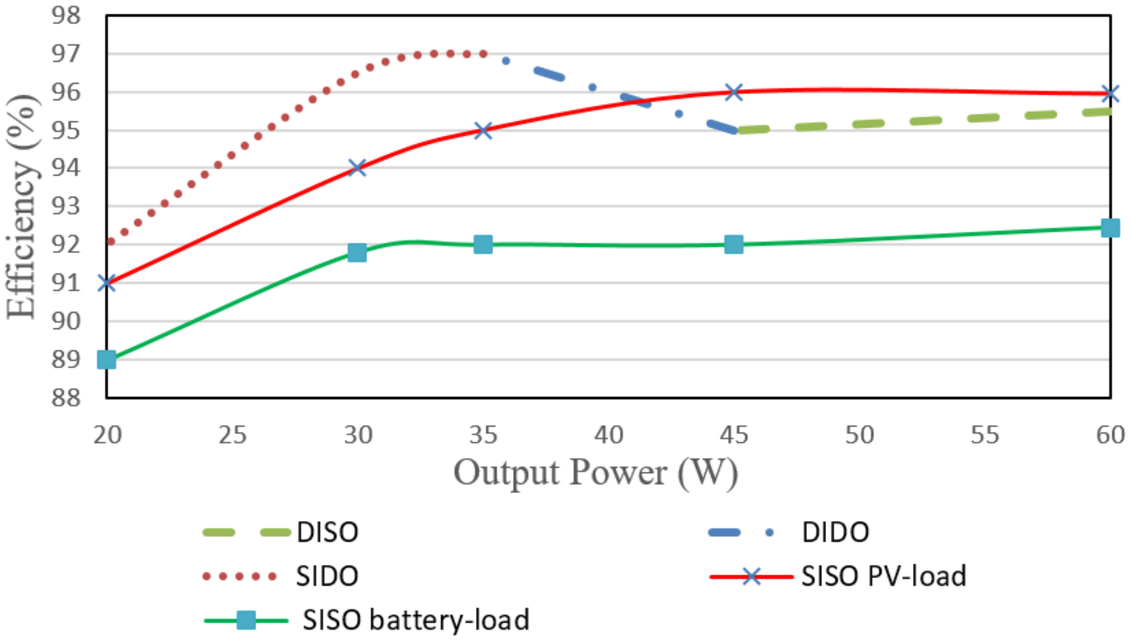

Fig. 5.14 : Measured efficiency curves obtained from the laboratory prototype for main operating modes.

The proposed converter can achieve MPP by using Perturb and Observe (P&O) algorithm and regulate the output voltage at around 50 V for all modes at a lower duty cycle. The operation duty cycle for the main switch changes between 32% and 45%. The comparison between the proposed converter and other converters is given in Table 5.3.

Table 5.3 : Comparison Between Proposed Converter and Other Structures

Topology	Rated Output power (W)	PV Voltage (V)	Battery Voltage (V)	Output Voltage (V)	Switching Frequency (kHz)	Component count			bidirectional ports	voltage gain	Average Efficiency
						switches	**Diodes**	**Inductors**			
[116]	500	35-70	70-100	100	100	3	3	One	ESS	1.7	97.2%
[22]	200	52.8	48	380	50	5	-	Two coupled-inductors and two leakage inductors	ESS	7.2	90.1%
[39]	150	72	36	400	50	4	4	Two coupled-inductors	ESS	5.5	95.5%
[23]	50	17	36	24	20	4	5	One	ESS	1.4	90%
[78]	1000	100-200	50-100	400	100	4	1	Two	ESS	4-8	97.5%
proposed converter	80	18	12	50	50	3	1	One coupled-inductor	ESS	2.7	93.7%

5.5 Summary

A new non-isolated multiport converter is proposed and experimentally verified to integrate a backup battery with a PV module for stand-alone power systems such as DC motor drives and LED drivers. A converter has an input unidirectional port for the PV module, a bidirectional port for a backup battery and an output port. The converter can provide a highly regulated output voltage by connecting the renewable energy source in series with the battery, and by using a coupled inductor. In addition, the proposed MPC can easily solve the problem of intermittency by using a simple control method. The highest average efficiency equals 93.7% while the highest average efficiency reaches 95.49% and the lowest at 90.75%. The MOSFET, coupled inductor and power diode are the major contributors to the total power loss for this converter design as the voltage stress on these components are high.

Chapter 6

A Novel High Step-up Three-Port Converter for PV-Battery Integrated System

6.1 Overview

The inverter design for the grid-connected PV system has skyrocketed; in fact it requires a special design specification to meet the performance requirements of the utility operator's specifications. As discussed earlier in Chapter 2, the solar system can be formed in the following main architectures [123]:

- Centralized DC/AC inverter structure.
- String DC/AC inverter structure.
- Centralized DC/AC inverter with centralized DC/DC converter structure.
- Centralized DC/AC inverter with string DC/DC converter structure.
- Centralized DC/AC inverter with string DC/DC optimizer structure.
- Detached microinverter or the AC module structure.

A microinverter (detached inverter) is used to integrate each PV module with its inverter; hence, it has been developed to eliminate the problem of MPPT. In general, to enhance the performance of the microinverter, the non-isolated topology is preferred due to its high efficiency, less component count, less bulky design, less cost and more compact compared to other topologies. The microinverter improves the system flexibility by supporting "plug and play" application and removing power mismatch that may occur between the panels. Also, it helps reduce the installing cost [76].

In general, the inverter in the above-mentioned architectures can be classified into two groups, namely single-stage microinverters and double-stage microinverters. In single-stage microinverters, MPPT and the grid requirement are managed in one stage which requires big capacitors and causes control limitation. On the other hand, double-stage microinverters, where two stages of power conversion are used, more control freedom is achieved, and low power decoupling capacitance is needed. As a result, double-stage microinverters increase microinverter reliability [6]. A non-isolated three-port converter plays a key role in the electric vehicle where a highly efficient and high voltage gain converter is needed to combine the battery, power source and motor [99]. Based on the above discussions, the proposed converter in Chapter 5 is modified to be implemented as the first stage in double-stage microinverters.

In this chapter, a new high step-up non-isolated three-port DC-DC converter (HS-NITPC) is proposed by enhancing the circuit proposed in Chapter 5. Nevertheless, the flyback diode is replaced by a power switch to allow the power to transfer back from the dc bus to the battery. In addition to replacing the flyback diode, the coupled inductor ratio is redesigned to boost the output voltage to a higher level. The converter is designed to integrate a solar panel with battery storage in order to boost its voltage, reduce the effect of solar energy intermittency and enhance the solar power performance under an unpredictable load demand. The converter combines three converters to form one integrated converter by sharing some components. Thus, the converter has high power density and fewer components compared to the traditional DC-DC converters. The coupled inductor is used to achieve a high output regulated voltage, transfer energy among the ports and facilitate maximum power point tracking for the solar panel. A hardware prototype

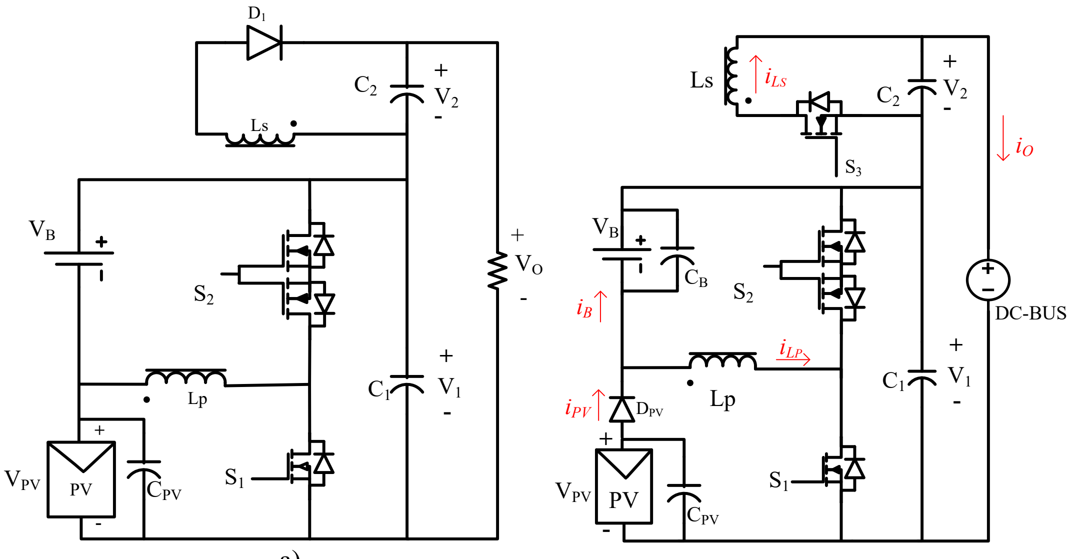

a) b)

Fig. 6.1 : a) Three-port converter proposed in Chapter 5. b) proposed circuit.

was built and tested to verify the proposed circuit for 180 W input power. The proposed converter is suitable for a stand-alone or grid-connected solar system. Moreover, it could be used in the electric vehicle where regenerative braking is used.

6.2 OPERATION PRINCIPLE

6.2.1 Proposed Circuit

Fig. 6.1(b) shows the proposed three-port bi-directional converter. The converter is composed of three main switches S_1, S_2 and S_3. S_2 is a bidirectional power switch that is implemented by using two switches connected back-to-back. One coupled inductor is formed by L_P and L_S, with a winding ratio 1:2.5 which is used as a voltage gain extension. C_1 and C_2 are used to smooth the output voltage while C_{PV} is used as a filter capacitor for the solar panel. V_{PV} is a unidirectional input port that is connected to the solar panel while the blocking diode D_{PV} is used to prevent the current from going back to the panel. This port is able to harvest the maximum power from the solar panel by tracking the maximum power point (MPP). V_B is a bi-directional battery port that can be used either to boost the input voltage to a high level due to its seriesconfiguration with the input port or to supply more power to the output when required in order to solve the intermittency issue and smooth the output power. The output capacitors C_1 and C_2 are large enough to smooth the output voltage. The proposed three-port converter has four main possible operating modes. The power flow among the ports is shown in Fig. 6.2.

6.2.2 Operation Modes

The proposed three-port converter has four main possible operation modes. The power flow among the ports are listed below:

1. **Single-input single-output (SISO) PV-battery**: This mode is active when the PV module charges the battery under no-load condition, as depicted in Fig. 6.2(a).
2. **Single-input single-output (SISO) battery-output**: This mode is active only when the battery supplies power to the load. In this mode, the PV module is either shaded or unable to supply power at night, as depicted in Fig. 6.2(b).
3. **Dual-input dual-output (DIDO)**: This mode is active when the PV supplies power to the load, and the battery is charged or discharged depending on the amount of power generated by the PV module and the power consumed by the load. This mode is depicted in Fig. 6.2(c).
4. **Single-input single-output (SISO) output-battery**: This mode is active when there is a need to recharge the battery when the solar panel is not able to supply power and the battery state of charge (SoC) is low. This newly added mode is useful for a grid-tie solar system application and it may also be

used for an electric vehicle (EV) where the regenerative breaker is changing the battery during its power recovery mode. This mode is depicted in Fig. 6.2(d).

6.2.3 Steady-State Analysis

1. SISO PV-battery mode: In this mode, S_1 and S_2 are operating in a complementary mode where S_3 is always OFF. The power generated by the PV module charges the battery to be used later. The combination of V_{PV}, L_P, S_1, S_2 and V_B is considered as a buck-boost converter. Thus, the battery at this mode charges effectively. Fig. 6.3(a) shows the current bath flow for the proposed converter. The regulated battery voltage is given in (6.1).

$$V_B = \frac{d_1}{1-d_1} V_{PV} = \frac{d_1}{d_2} V_{PV} \tag{6.1}$$

2. SISO battery-output mode: In this mode, only two ports are active, the battery and the output port. The combination of $V_{PV}, L_P, L_S, S_2, S_3, C_2$ and V_2 is considered as a forward converter. The converter regulated output voltage derives in (6.2), and the current path flow is shown in Fig. 6.3(d).

$$V_O = \frac{N_P V_B + N_S V_1 (1-d_2)^2}{N_P(1-d_2)} = \frac{N_P V_B + N_S V_B (1-d_2)}{N_P(1-d_2)} \tag{6.2}$$

3. DIDO modes: In this mode, the following three assumptions are made: the combination of $V_{PV}, L_P, L_S, S_1, S_3, C_2$ and V_2 is considered as a flyback converter, the combination of V_{PV}, L_P, S_1, S_2 and V_b is considered as a buck-boost converter and the combination of $V_{PV}, L_P, S_1, S_2, C_1$ and V_1 is considered as a boost converter. In this mode all ports are active.

   When S_1 is turned ON, and S_2 and S_3 are turned OFF, the inductor starts charging by the PV panel. No current will flow in L_S due to the polarity of

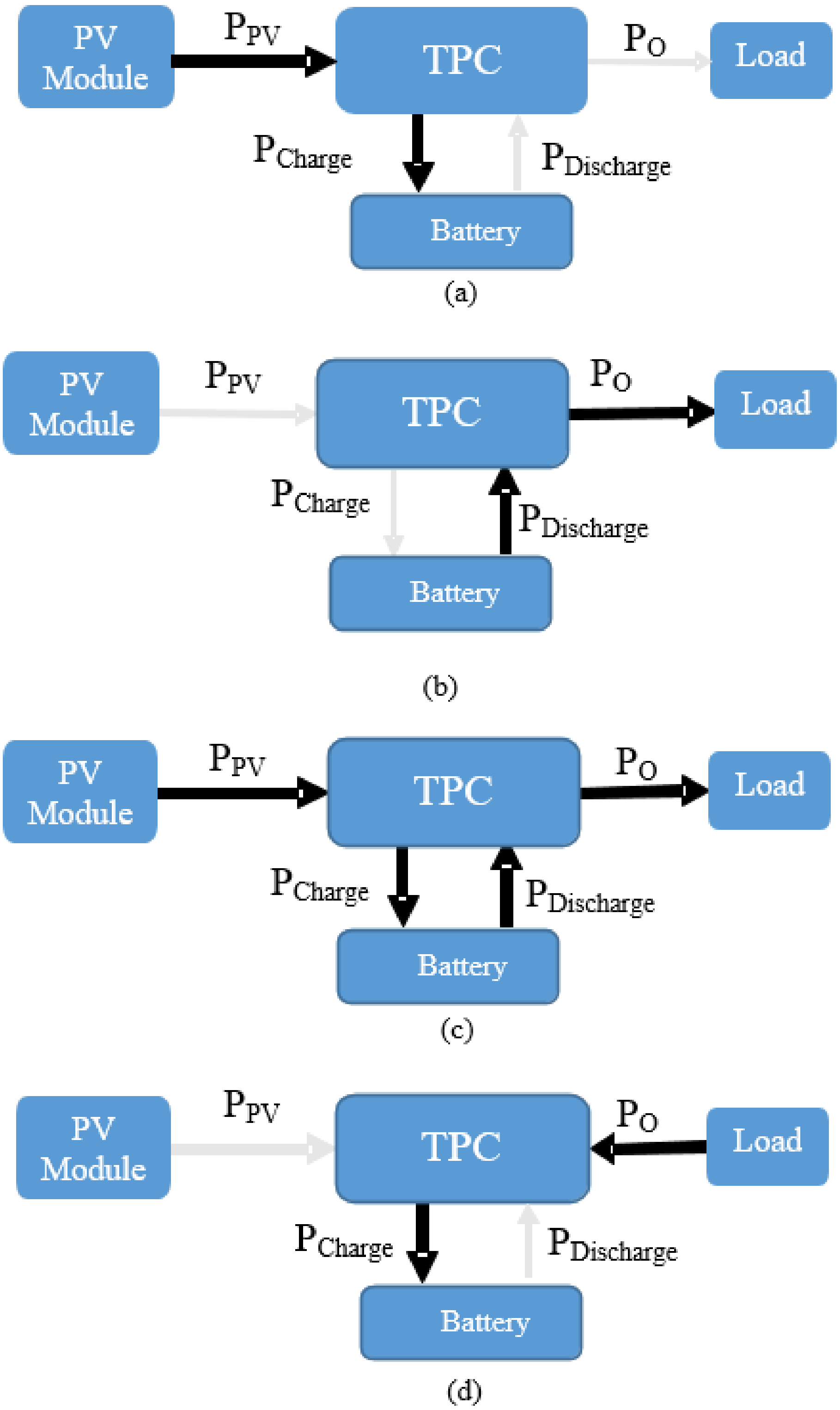

Fig. 6.2 : Power flow: a) SISO PV-battery. b) SISO battery-output. c) DIDO. d) SISO output-battery.

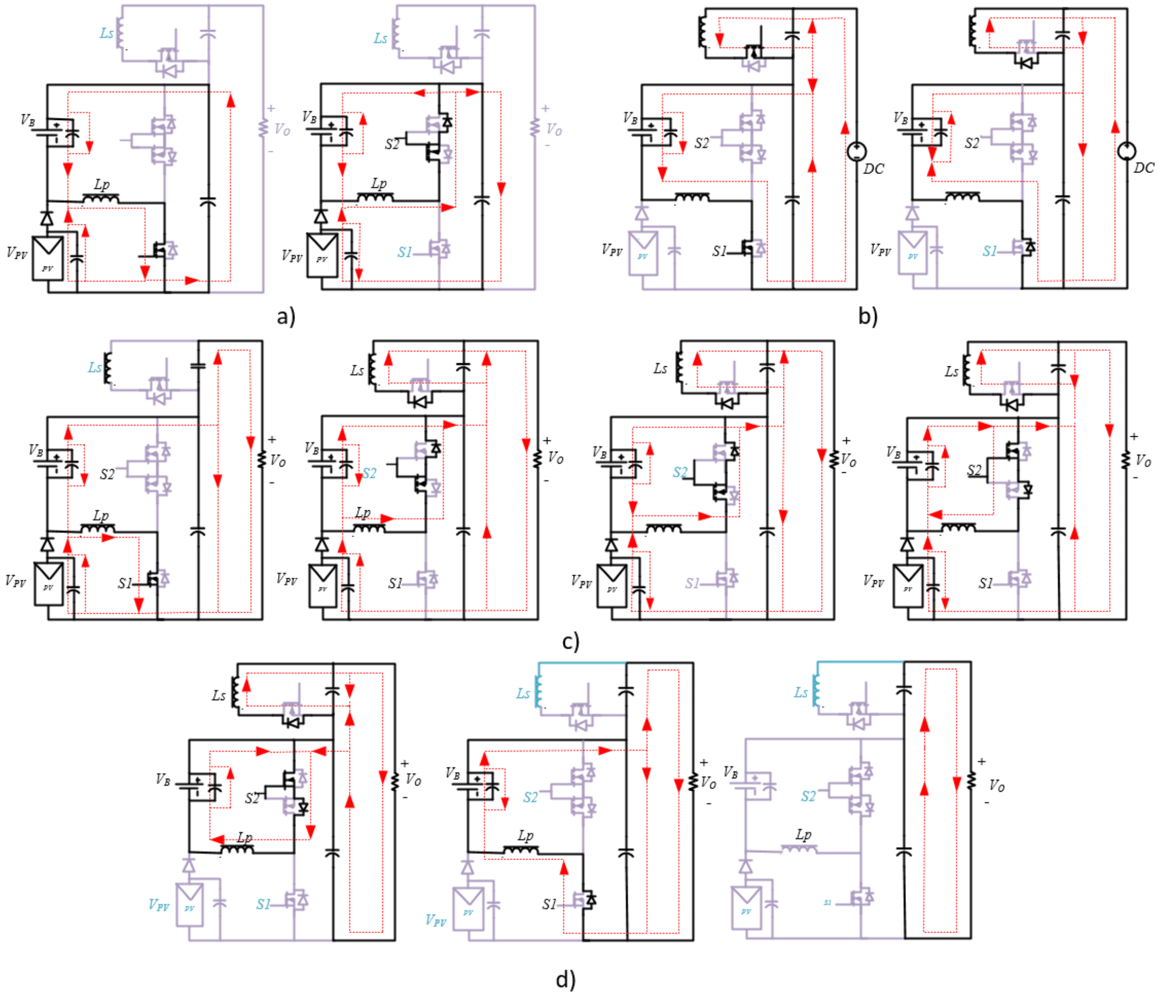

Fig. 6.3 : Current flow TPC and operation modes: (a) SISO PV-battery mode. (b) SISO output-battery mode. (c) DIDO. (d) SISO battery-output mode.

the coupled inductor which makes the body diode of S_3 reverse-biased, and consequently some energy will be stored in the coupled inductor. When S_2 and S_3 are turned ON, S_1 will turn OFF and the primary inductor then starts to discharge to charge the battery. At the same time, the energy stored in the coupled inductor will be transferred to the output. If the power generated by the PV panel is not enough to supply the load, more current will be taken from the battery. As a result, the current direction at the battery port is reversed. The current path flow is depicted in Fig. 6.3(c). V_B, V_1, V_2, and V_O for this mode are given in (6.1) (6.3), (6.4), and (6.5) respectively.

$$V_1 = \frac{V_{PV}}{1 - d_1} \tag{6.3}$$

$$V_2 = \frac{N_S}{N_P}\frac{d_1}{d_2}V_{PV} = \frac{N_S}{N_P}V_B \tag{6.4}$$

$$V_O = V_1 + V_2 = \frac{1 + \frac{N_S}{N_P}d_1}{d_2}V_{PV} \tag{6.5}$$

4. SISO Output-Battery mode: This mode is similar to the SISO battery-Output mode. However, the current direction is flipped, as shown in Fig. 6.3(b). In this mode, the output port connected to the 169 V DC bus which is suitable for 120 V AC mains power.

$$V_B = \frac{V_O N_P d_1}{N_P + N_S d_1} \tag{6.6}$$

6.3 Simulation and Experiment Results

The converter is simulated using Switcher-CADIII-LTSpice from Linear Technology then an experimental prototype is built to verify the performance and feasibility of the proposed converter, as shown in Fig. 6.4. A programmable power supply (model: EA-PSI 9750-12 2U) that has the solar PV emulator function is used to

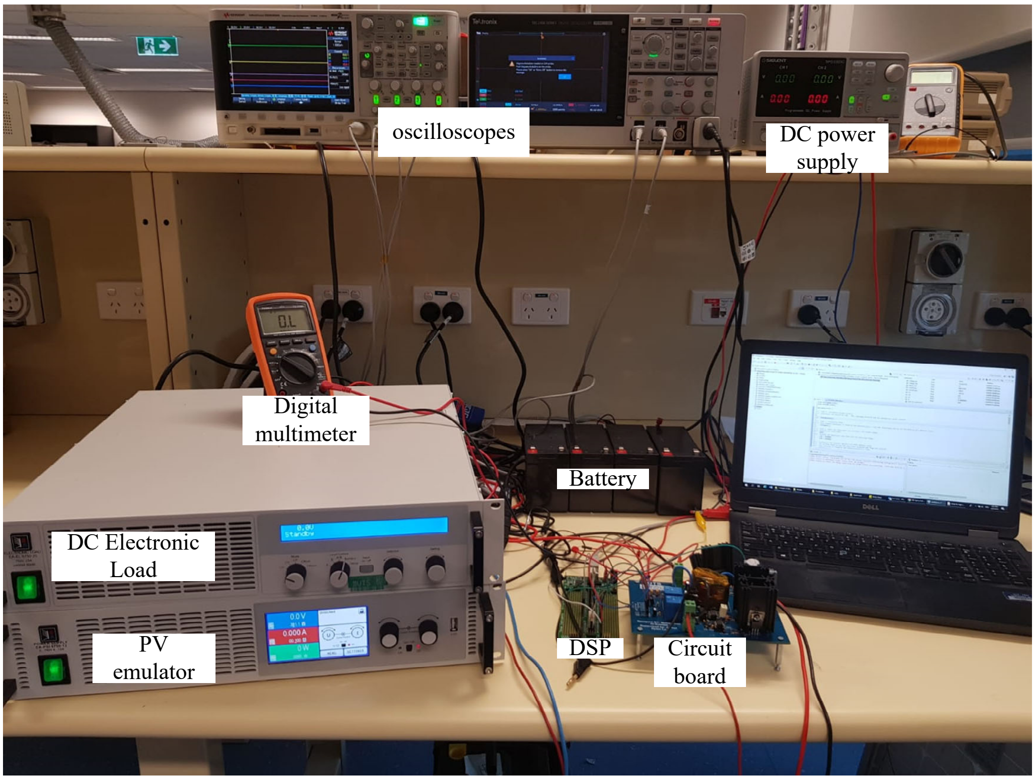

Fig. 6.4 : Experimental setup of laboratory prototype.

mimic the behaviour of a 180 W solar panel, and it is connected with the input port V_{PV}. In order to ensure the accuracy of the used PV emulator, an experiment was carried out to plot the P-V curve of 180 W solar panel, and then to compare the result with the actual PV module. It is experimentally found that the voltage at the maximum power point (V_{MPP}) is equal 38 V. Three 12V, 12Ah lead-acid batteries are connected in series to obtain the desired voltage which is 36 V. Then it is connected with battery port V_B. The output port $V_O = 170$ V is connected to DC Electronic Load (model: EA-EL 9750-25). The design consideration and the control circuit are similar to the one in Chapter 5. The values of the key parameters are given in Table 6.1.

Table 6.1 : Components Details.

Component	Parameter	Model/Value
Digital controller	-	TMS320F28335
Switching frequency	f_s	50 kHz
MOSFET	S_2&S_2	IRF540N
MOSFET	S_3	C3M0065090D
MOSFET driver for S_1	-	TC4426
MOSFET driver for S_2&S_3	-	IR2184PBF
Coupled inductor core	-	RM14/I-3C95
Coupled inductor turns ratio	N_P/N_S	1/2.5
primary inductor	L_P	100 µH
secondary inductor	L_S	625 µH
output capacitor	C_1	470 µF
output capacitor	C_2	330 µF
PV filter capacitor	C_2	100 µF

Key experimental waveforms are shown in Fig. 6.5. The average simulation efficiency is 91.2% for SISO PV-Battery, 89.5% for SISO Battery-Output, 87% for SISO Output-Battery and 89.99% for DIDO mode while the average experimental efficiency is 86.5% for SISO PV-Battery, 85% for SISO Battery-Output, 81% for SISO Output-Battery and 88.3% for DIDO mode. The comparison between the proposed converter and other converters is given in Table 6.2.

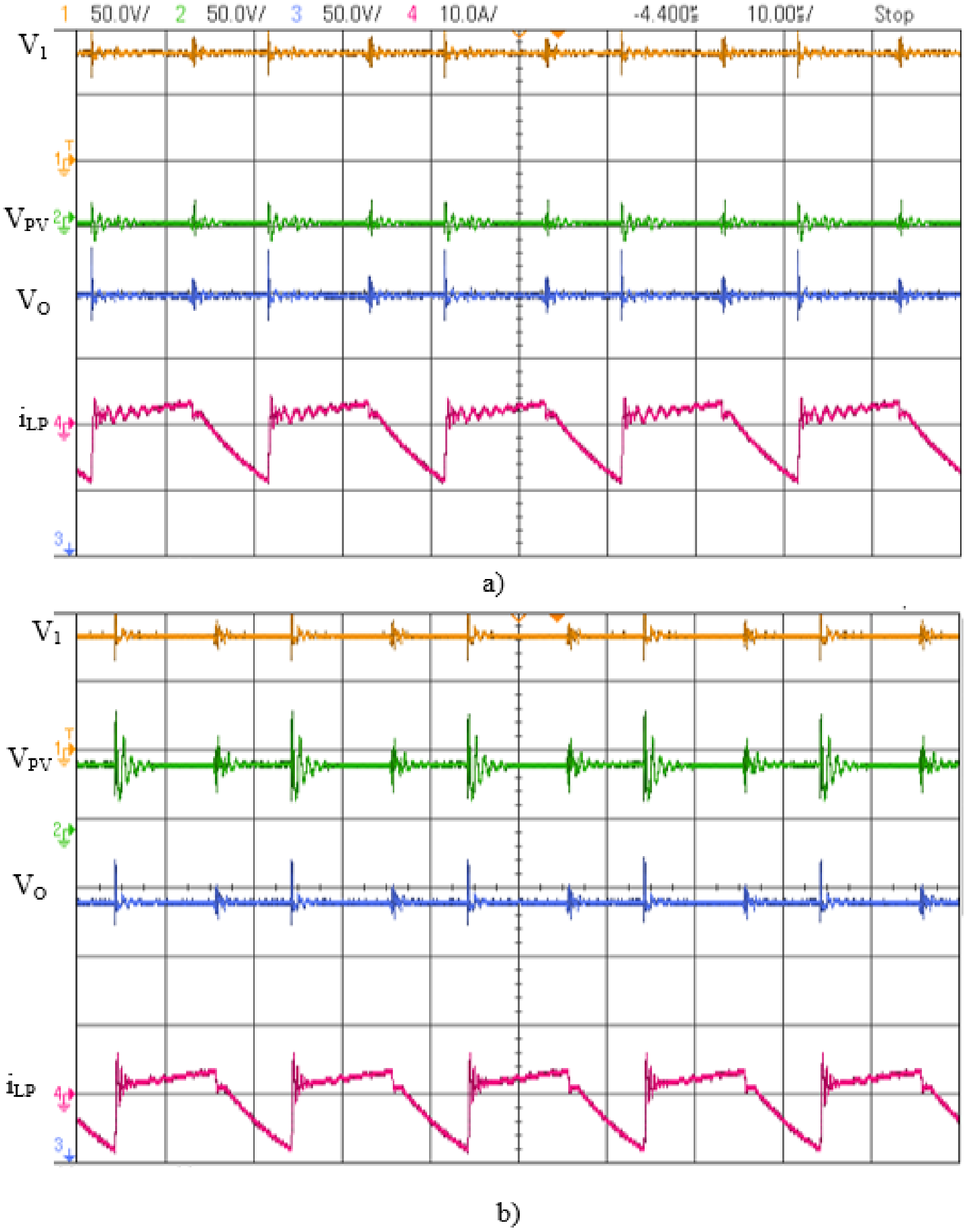

Fig. 6.5 : Experiment result: a) SISO battery-Load. b) DIDO mode. [Time base: 20s. V1: 40V/div, VPV: 40V/div, VO: 40V/div and iLP: 10A/div].

Table 6.2 : Comparison of Proposed Converter and Other Converters.

Topology	Rated Output power (W)	PV Voltage (V)	Battery Voltage (V)	Output Voltage (V)	Switching Frequency (kHz)	Component count			bidirectional ports	voltage gain	Average Efficiency
						switches	**Diodes**	**Inductors**			
[116]	500	35-70	70-100	100	100	3	3	One	ESS	1.7	97.2%
[22]	200	52.8	48	380	50	5	-	Two coupled-inductors and two leakage inductors	ESS	7.2	90.1%
[39]	150	72	36	400	50	4	4	Two coupled-inductors	ESS	5.5	95.5%
[23]	50	17	36	24	20	4	5	One	ESS	1.4	90%
[78]	1000	100-200	50-100	400	100	4	1	Two	ESS	4-8	97.5%
TPC in Chapter 5	80	18	12	50	50	3	1	One coupled-inductor	ESS	2.7	93.7%
proposed converter	180	38	36	168	50	4	0	One coupled-inductor	ESS	4.74	85.2%

6.4 Summary

In this chapter, a bi-directional non-isolated high step-up DC-DC converter is proposed and experimentally verified for the standalone and grid-connected system. The proposed converter is able to achieve MPP by implementing the Perturb and Observe (P&O) algorithm, regulating the output voltage and performing the battery management simultaneously. By using such a converter, the output voltage for the solar panel can be boosted easily by using a lower duty cycle, resulting in less voltage stress on the switches. It also facilitates the use of the microinverter and plug-and-play concept. The solar energy intermittency and unpredictable change in demand effects are eliminated by using energy storage system (ESS).

Chapter 7

Conclusion and Future Work

7.1 Conclusion

This thesis focuses on improving the capability and solving the intermittency of the PV generation where four different contributions are proposed, designed, and validated by the experimental results under different applications. They are:

- A non-intrusive method to detect the cracked and aged PV cells by studying the dynamic regime of the solar cells.
- A simple analog approach to improving maximum power point tracking efficiency by using a bipolar junction transistor that has characteristic similar to the PV cell.
- A non-isolated three-port converter to integrate a backup battery with a PV module for stand-alone power systems.
- A high step-up non-isolated three-port DC-DC converter (HS-NITPC) with two bidirectional ports for grid-connected power systems and electric vehicle where the regenerative breaker is used.

The following conclusions can be drawn upon the fulfillment of the research:

The loss of electrical connection between the PV cell and busbar would cause a significant reduction of the entire PV string power generation capability. It is experimentally verified that the fully cracked cells show a higher resistive and capacitive characteristic at high frequency than others. A crack detection technique is proposed to investigate the cracked and aged cells to improve overall solar system efficiency and reliability. The experiment result shows that the current leads the voltage by 27° for the normal string while it increases by 11.66° to become 38.66° for string with one cell totally cracked. A comparison between the series and parallel connected PV panel strings are given. Bypass diodes are recommended to be added to the PV panel string to mitigate the current reduction by the seriously cracked cells to increase the solar cell lifetime, improve the solar system efficiency and reliability.

BJT has a characteristic similar to the PV cell that can be used for MPPT by using a simple voltage and current feedforward- feedback control. The collector current of the BJT is used to mimic a voltage slope that matches the maximum power points for the PV cell under different radiation levels providing more accurate tracking compared to the constant voltage tracking technique. The proposed analog control with a tracking efficiency ranging from 93.39% to 99.2% for different solar insolation levels can be used in aerospace and low-cost system applications due to its pure analog implementation and cost-effective nature.

The ESS becomes a necessary element for the RES as it can solve the intermittency issue, unpredictable change in demand, and help to manage the grid requirements. A bi-directional non-isolated high step-up three-port DC-DC converter is one of the best candidates to integrate the ESS with a PV module as it can reach high efficiency, and it can share some components. The converter proposed in chapter 5 can be used for stand-alone power systems, such as DC motor drives and LED drivers. The highest average efficiency equals 93.7%, while the highest average efficiency reaches 95.49% and the lowest at 90.75%. The converter has only one bidirectional switch, one unidirectional switch, one coupled inductor, one diode and two capacitors.

The converter proposed in Chapter 6 is suitable for stand-alone or grid solar system, and it could be used for the electric vehicle where the regenerative breaker is used. In this converter, the diode in the previous topology is replaced by bidirectional switch to allow the current flow back to the battery. The measured experimental efficiency is 86.5% for SISO PV-Battery, 85% for SISO Battery-Output, 81% for SISO Output-Battery and 88.3% for DIDO mode. The voltage gain for this converter equals 4.45.

7.2 Future Work

Recommendations for future research are listed as follows:

- The crack tracking technique was implemented by injecting a variable frequency AC signal by using a function generator. For future work, the proposed technique will be implemented within the power converter that can be operated at a variable frequency. The converter will be controlled by DSP where the current waveform can be captured.
- The MPP tracking technique was implemented by BJT with variable resistor (potentiometer). For future work, the digital potentiometer will be used to modify the generated MPP reference voltage curve as that curve could differ from one cell to other, and it may change with the cell aging.
- Thermal coupling and electromagnetic interference aspects of the proposed three-port converter.
- A PV module prototype could be built to integrate all of the proposed techniques and converters to show the visibility and reliability for the integrated PV-battery system with this crack detection technique.
- Extending the capability of the proposed TPC by integrating a proper inverter to facilitate plug and play PV-battery system.

Bibliography

[1] J. A. Abu Qahouq and Y. Jiang, “Distributed photovoltaic solar system architecture with single-power inductor single-power converter and single-sensor single maximum power point tracking controller,” *IET Power Electronics*, vol. 7, no. 10, pp. 2600–2609, 2014.

[2] G. W. Adhyaksa, L. W. Veldhuizen, Y. Kuang, S. Brittman, R. E. Schropp, and E. C. Garnett, “Carrier diffusion lengths in hybrid perovskites: processing, composition, aging, and surface passivation effects,” *Chemistry of Materials*, vol. 28, no. 15, pp. 5259–5263, 2016.

[3] J. Ahmad, “A fractional open circuit voltage based maximum power point tracker for photovoltaic arrays,” in *2010 2nd International Conference on Software Technology and Engineering*, vol. 1, Oct 2010, pp. V1–247–V1–250.

[4] A. Ajami, H. Ardi, and A. Farakhor, “A novel high step-up dc/dc converter based on integrating coupled inductor and switched-capacitor techniques for renewable energy applications,” *IEEE Transactions on Power Electronics*, vol. 30, no. 8, pp. 4255–4263, Aug 2015.

[5] H. Al-Atrash, F. Tian, and I. Batarseh, “Tri-modal half-bridge converter topology for three-port interface,” *IEEE Transactions on Power Electronics*, vol. 22, no. 1, pp. 341–345, Jan 2007.

[6] K. Alluhaybi, I. Batarseh, H. Hu, and X. Chen, “Comprehensive review and comparison of single-phase grid-tied photovoltaic microinverters,” *IEEE Journal of Emerging and Selected Topics in Power Electronics*, pp. 1–1, 2019.

[7] J. Amanor-Boadu, A. Guiseppi-Elie, and E. Sánchez-Sinencio, “The impact of pulse charging parameters on the life cycle of lithium-ion polymer batteries,” *Energies*, vol. 11, no. 8, p. 2162, 2018.

[8] L. An and D. D. Lu, “Design of a single-switch dc/dc converter for a pv-battery-powered pump system with pfm+pwm control,” *IEEE Transactions on Industrial Electronics*, vol. 62, no. 2, pp. 910–921, Feb 2015.

[9] D. Baimel, R. Shkoury, L. Elbaz, S. Tapuchi, and N. Baimel, “Novel optimized method for maximum power point tracking in pv systems using fractional open circuit voltage technique,” in *2016 International Symposium on Power Electronics, Electrical Drives, Automation and Motion (SPEEDAM)*, June 2016, pp. 889–894.

[10] E. I. Batzelis, “Simple pv performance equations theoretically well founded on the single-diode model,” *IEEE Journal of Photovoltaics*, vol. 7, no. 5, pp. 1400–1409, Sep. 2017.

[11] E. I. Batzelis, G. E. Kampitsis, S. A. Papathanassiou, and S. N. Manias, “Direct mpp calculation in terms of the single-diode pv model parameters,” *IEEE Trans. Energy Convers.*, vol. 30, no. 1, pp. 226–236, March 2015.

[12] E. I. Batzelis and S. A. Papathanassiou, “A method for the analytical extraction of the single-diode pv model parameters,” *IEEE Transactions on Sustainable Energy*, vol. 7, no. 2, pp. 504–512, April 2016.

[13] N. D. Benavides and P. L. Chapman, “Modeling the effect of voltage ripple on the power output of photovoltaic modules,” *IEEE Transactions on Industrial Electronics*, vol. 55, no. 7, pp. 2638–2643, 2008.

[14] A. K. Bhattacharjee, N. Kutkut, and I. Batarseh, “Review of multiport converters for solar and energy storage integration,” *IEEE Transactions on*

Power Electronics, vol. 34, no. 2, pp. 1431–1445, Feb 2019.

[15] A. Bidram, A. Davoudi, and R. S. Balog, “Control and circuit techniques to mitigate partial shading effects in photovoltaic arrays,” *IEEE Journal of Photovoltaics*, vol. 2, no. 4, pp. 532–546, Oct 2012.

[16] L. Bird, M. Milligan, and D. Lew, “Integrating variable renewable energy: Challenges and solutions,” National Renewable Energy Lab.(NREL), Golden, CO (United States), Tech. Rep., 2013.

[17] H. Bizhani, R. Noroozian, S. M. Muyeen, K. Techato, and F. Blaabjerg, “A grid-connected smart extendable structure for hybrid integration of distributed generations,” *IEEE Access*, vol. 7, pp. 105 235–105 246, 2019.

[18] F. Blaabjerg, Z. Chen, and S. B. Kjaer, “Power electronics as efficient interface in dispersed power generation systems,” *IEEE Transactions on Power Electronics*, vol. 19, no. 5, pp. 1184–1194, Sep. 2004.

[19] B. K. Bose, “Power electronics, smart grid, and renewable energy systems,” *Proceedings of the IEEE*, vol. 105, no. 11, pp. 2011–2018, Nov 2017.

[20] J. M. Carrasco, L. G. Franquelo, J. T. Bialasiewicz, E. Galvan, R. C. PortilloGuisado, M. A. M. Prats, J. I. Leon, and N. Moreno-Alfonso, “Power-electronic systems for the grid integration of renewable energy sources: A survey,” *IEEE Transactions on Industrial Electronics*, vol. 53, no. 4, pp. 1002–1016, June 2006.

[21] L. Chen, S. Wu, D. Shieh, and T. Chen, “Sinusoidal-ripple-current charging strategy and optimal charging frequency study for li-ion batteries,” *IEEE Transactions on Industrial Electronics*, vol. 60, no. 1, pp. 88–97, Jan 2013.

[22] Y. Chen, A. Q. Huang, and X. Yu, “A high step-up three-port dc–dc converter

for stand-alone pv/battery power systems," *IEEE Transactions on Power Electronics*, vol. 28, no. 11, pp. 5049–5062, Nov 2013.

[23] T. Cheng, D. D. Lu, and L. Qin, "Non-isolated single-inductor dc/dc converter with fully reconfigurable structure for renewable energy applications," *IEEE Transactions on Circuits and Systems II: Express Briefs*, vol. 65, no. 3, pp. 351–355, March 2018.

[24] D. Chenvidhya, K. Kirtikara, and C. Jivacate, "Pv module dynamic impedance and its voltage and frequency dependencies," *Solar Energy Materials and Solar Cells*, vol. 86, no. 2, pp. 243–251, 2005.

[25] L. Chien, C. Chen, J. Chen, and Y. Hsieh, "Novel three-port converter with high-voltage gain," *IEEE Transactions on Power Electronics*, vol. 29, no. 9, pp. 4693–4703, Sept 2014.

[26] J. Confrey, A. H. Etemadi, S. M. F. Stuban, and T. J. Eveleigh, "Energy storage systems architecture optimization for grid resilience with high penetration of distributed photovoltaic generation," *IEEE Systems Journal*, pp. 1–12, 2019.

[27] D. Cotfas, P. Cotfas, and S. Kaplanis, "Methods to determine the dc parameters of solar cells: A critical review," *Renewable and Sustainable Energy Reviews*, vol. 28, pp. 588–596, 2013.

[28] D. "Cotfas, P. Cotfas, and S. Kaplanis, "Methods and techniques to determine the dynamic parameters of solar cells," *Renewable and Sustainable Energy Reviews*, vol. 61, pp. 213–221, 2016.

[29] W. T. da Costa, J. F. Fardin, D. S. L. Simonetti, and L. de V. B. M. Neto, "Identification of photovoltaic model parameters by differential evolution," in

2010 IEEE International Conference on Industrial Technology, March 2010, pp. 931–936.

[30] M. Danesh and J. R. Long, "Photovoltaic antennas for autonomous wireless systems," *IEEE Transactions on Circuits and Systems II: Express Briefs*, vol. 58, no. 12, pp. 807–811, Dec 2011.

[31] J. Deng, H. Wang, and M. Shang, "A zvs three-port dc/dc converter for high-voltage bus based photovoltaic systems," *IEEE Transactions on Power Electronics*, pp. 1–1, 2019.

[32] M. Dhimish, V. Holmes, M. Dales, and B. Mehrdadi, "Effect of micro cracks on photovoltaic output power: case study based on real time long term data measurements," *Micro & Nano Letters*, vol. 12, no. 10, pp. 803–807, 2017.

[33] M. Dhimish, V. Holmes, B. Mehrdadi, and M. Dales, "The impact of cracks on photovoltaic power performance," *Journal of Science: Advanced Materials and Devices*, vol. 2, no. 2, pp. 199–209, 2017.

[34] K. Ding, X. Bian, H. Liu, and T. Peng, "A matlab-simulink-based pv module model and its application under conditions of nonuniform irradiance," *IEEE Transactions on Energy Conversion*, vol. 27, no. 4, pp. 864–872, Dec 2012.

[35] B. G. Dobbs and P. L. Chapman, "A multiple-input dc-dc converter topology," *IEEE Power Electronics Letters*, vol. 1, no. 1, pp. 6–9, March 2003.

[36] A. Dolara, S. Leva, G. Manzolini, and E. Ogliari, "Investigation on performance decay on photovoltaic modules: Snail trails and cell microcracks," *IEEE journal of photovoltaics*, vol. 4, no. 5, pp. 1204–1211, 2014.

[37] Y. Du and D. D.-C. Lu, "Battery-integrated boost converter utilizing distributed mppt configuration for photovoltaic systems," *Solar energy*, vol. 85, no. 9, pp. 1992–2002, 2011.

[38] J. L. Duarte, M. Hendrix, and M. G. Simoes, “Three-port bidirectional converter for hybrid fuel cell systems,” *IEEE Transactions on Power Electronics*, vol. 22, no. 2, pp. 480–487, March 2007.

[39] R. Faraji and H. Farzanehfard, “Soft-switched nonisolated high step-up three-port dc–dc converter for hybrid energy systems,” *IEEE Transactions on Power Electronics*, vol. 33, no. 12, pp. 10 101–10 111, Dec 2018.

[40] N. Femia, G. Petrone, G. Spagnuolo, and M. Vitelli, “Optimization of perturb and observe maximum power point tracking method,” *IEEE Transactions on Power Electronics*, vol. 20, no. 4, pp. 963–973, July 2005.

[41] V. Gade, N. Shiradkar, M. Paggi, and J. Opalewski, “Predicting the long term power loss from cell cracks in pv modules,” in *2015 IEEE 42nd Photovoltaic Specialist Conference (PVSC)*. IEEE, 2015, pp. 1–6.

[42] H. Tao and A. Kotsopoulos and J. L. Duarte and M. A. M. Hendrix, “Family of multiport bidirectional DC-DC converters,” *IEE Proceedings - Electric Power Applications*, vol. 153, no. 3, pp. 451–458, May 2006.

[43] M. Hejri and H. Mokhtari, “On the comprehensive parametrization of the photovoltaic (pv) cells and modules,” *IEEE Journal of Photovoltaics*, vol. 7, no. 1, pp. 250–258, Jan 2017.

[44] C. A. Hill, M. C. Such, D. Chen, J. Gonzalez, and W. M. Grady, “Battery energy storage for enabling integration of distributed solar power generation,” *IEEE Transactions on Smart Grid*, vol. 3, no. 2, pp. 850–857, June 2012.

[45] R. Hou and A. Emadi, “A primary full-integrated active filter auxiliary power module in electrified vehicles with single-phase onboard chargers,” *IEEE Transactions on Power Electronics*, vol. 32, no. 11, pp. 8393–8405, Nov 2017.

[46] Y. Hu, W. Xiao, W. Cao, B. Ji, and D. J. Morrow, "Three-port dc–dc converter for stand-alone photovoltaic systems," *IEEE Transactions on Power Electronics*, vol. 30, no. 6, pp. 3068–3076, June 2015.

[47] C. Hua and C. Shen, "Comparative study of peak power tracking techniques for solar storage system," in *APEC '98 Thirteenth Annual Applied Power Electronics Conference and Exposition*, vol. 2, Feb 1998, pp. 679–685 vol.2.

[48] S. . P. Independence, "Pv module bypass diodes – what are they and what do they do?" 2019, retrieved on 14/8/2019. [Online]. Available: https://www.sunwize.com/tech-notes/pv-module-bypass-diodes-what-are-they-and-what-do-they-do/

[49] S. Kajari-Schršder, I. Kunze, and M. Kšntges, "Criticality of cracks in pv modules," *Energy Procedia*, vol. 27, pp. 658–663, 2012.

[50] F. Kardan, R. Alizadeh, and M. R. Banaei, "A New Three Input DC/DC Converter for Hybrid PV/FC/Battery Applications," *IEEE Journal of Emerging and Selected Topics in Power Electronics*, vol. 5, no. 4, pp. 1771–1778, Dec 2017.

[51] N. Katayama, S. Osawa, S. Matsumoto, T. Nakano, and M. Sugiyama, "Degradation and fault diagnosis of photovoltaic cells using impedance spectroscopy," *Solar Energy Materials and Solar Cells*, vol. 194, pp. 130–136, 2019.

[52] A. Khaligh, J. Cao, and Y. Lee, "A multiple-input dc–dc converter topology," *IEEE Transactions on Power Electronics*, vol. 24, no. 3, pp. 862–868, March 2009.

[53] O. Khan and W. Xiao, "Integration of start–stop mechanism to improve maximum power point tracking performance in steady state," *IEEE*

Transactions on Industrial Electronics, vol. 63, no. 10, pp. 6126–6135, Oct 2016.

[54] H. Kim, Y. J. Min, C. H. Jeong, K. Y. Kim, C. Kim, and S. W. Kim, "A 1-mw solar-energy-harvesting circuit using an adaptive mppt with a sar and a counter," *IEEE Transactions on Circuits and Systems II: Express Briefs*, vol. 60, no. 6, pp. 331–335, June 2013.

[55] J. Kim, J. Kim, and C. Kim, "A regulated charge pump with a low-power integrated optimum power point tracking algorithm for indoor solar energy harvesting," *IEEE Transactions on Circuits and Systems II: Express Briefs*, vol. 58, no. 12, pp. 802–806, Dec 2011.

[56] K. A. Kim, G.-S. Seo, B.-H. Cho, and P. T. Krein, "Photovoltaic hot-spot detection for solar panel substrings using ac parameter characterization," *IEEE Transactions on Power Electronics*, vol. 31, no. 2, pp. 1121–1130, 2015.

[57] K. A. Kim, C. Xu, L. Jin, and P. T. Krein, "A dynamic photovoltaic model incorporating capacitive and reverse-bias characteristics," *IEEE Journal of photovoltaics*, vol. 3, no. 4, pp. 1334–1341, 2013.

[58] S. Kirmani, M. Jamil, and I. Akhtar, "Economic feasibility of hybrid energy generation with reduced carbon emission," *IET Renewable Power Generation*, vol. 12, no. 8, pp. 934–942, 2018.

[59] J. Kivimäki, S. Kolesnik, M. Sitbon, T. Suntio, and A. Kuperman, "Revisited perturbation frequency design guideline for direct fixed-step maximum power point tracking algorithms," *IEEE Transactions on Industrial Electronics*, vol. 64, no. 6, pp. 4601–4609, June 2017.

[60] S. B. Kjaer, J. K. Pedersen, and F. Blaabjerg, "A review of single-phase grid-connected inverters for photovoltaic modules," *IEEE Transactions on Industry*

Applications, vol. 41, no. 5, pp. 1292–1306, Sep. 2005.

[61] M. Köntges, I. Kunze, S. Kajari-Schröder, X. Breitenmoser, and B. Bjørneklett, "The risk of power loss in crystalline silicon based photovoltaic modules due to micro-cracks," *Solar Energy Materials and Solar Cells*, vol. 95, no. 4, pp. 1131–1137, 2011.

[62] M. Köntges, S. Kurtz, C. Packard, U. Jahn, K. A. Berger, and K. Kato, *Performance and reliability of photovoltaic systems: Subtask 3.2: Review of failures of photovoltaic modules.* IEA PVPS task 13: External final report IEA-PVPS. International Energy Agency, Photovoltaic Power Systems Programme, 2014.

[63] H. Krishnaswami and N. Mohan, "Three-port series-resonant dc–dc converter to interface renewable energy sources with bidirectional load and energy storage ports," *IEEE Transactions on Power Electronics*, vol. 24, no. 10, pp. 2289–2297, Oct 2009.

[64] S. Kumar, V. Sareen, N. Batra, and P. Singh, "Study of c–v characteristics in thin n+-p-p+ silicon solar cells and induced junction np-p+ cell structures," *Solar Energy Materials and Solar Cells*, vol. 94, no. 9, pp. 1469–1472, 2010.

[65] S. Li, T. A. Haskew, D. Li, and F. Hu, "Integrating photovoltaic and power converter characteristics for energy extraction study of solar pv systems," *Renewable Energy*, vol. 36, no. 12, pp. 3238–3245, 2011.

[66] T. J. Liang and K. C. Tseng, "Analysis of integrated boost-flyback step-up converter," *IEE Proceedings - Electric Power Applications*, vol. 152, no. 2, pp. 217–225, March 2005.

[67] D. Liu and H. Li, "A zvs bi-directional dc–dc converter for multiple energy storage elements," *IEEE Transactions on Power Electronics*, vol. 21, no. 5,

pp. 1513–1517, Sep. 2006.

[68] F. Liu, S. Duan, F. Liu, B. Liu, and Y. Kang, "A variable step size inc mppt method for pv systems," *IEEE Transactions on Industrial Electronics*, vol. 55, no. 7, pp. 2622–2628, July 2008.

[69] S. T. I. Ltd, "5-150 watt solar panel kit," retrieved on 15/8/2019. [Online]. Available: https://www.solartechnology.co.uk/solar-panels/pv-logic-panels/standard-solar-panels

[70] Y. Lu, K. Sun, H. Wu, X. Dong, and Y. Xing, "A three-port converter based distributed dc grid connected pv system with autonomous output voltage sharing control," *IEEE Transactions on Power Electronics*, vol. 34, no. 1, pp. 325–339, Jan 2019.

[71] S. Lyden, M. E. Haque, A. Gargoom, and M. Negnevitsky, "Review of maximum power point tracking approaches suitable for pv systems under partial shading conditions," in *2013 Australasian Universities Power Engineering Conference (AUPEC)*, Sep. 2013, pp. 1–6.

[72] H. Mahmood, D. Michaelson, and J. Jiang, "A power management strategy for pv/battery hybrid systems in islanded microgrids," *IEEE Journal of Emerging and Selected Topics in Power Electronics*, vol. 2, no. 4, pp. 870–882, Dec 2014.

[73] Y. Mahmoud and E. El-Saadany, "Accuracy improvement of the ideal pv model," *IEEE Transactions on Sustainable Energy*, vol. 6, no. 3, pp. 909–911, July 2015.

[74] Y. Mahmoud and W. Xiao, "Evaluation of shunt model for simulating photovoltaic modules," *IEEE Journal of Photovoltaics*, vol. 8, no. 6, pp. 1818–1823, Nov 2018.

[75] Y. Mahmoud, W. Xiao, and H. H. Zeineldin, “A simple approach to modeling and simulation of photovoltaic modules,” *IEEE Transactions on Sustainable Energy*, vol. 3, no. 1, pp. 185–186, Jan 2012.

[76] D. Meneses, F. Blaabjerg, . García, and J. A. Cobos, “Review and comparison of step-up transformerless topologies for photovoltaic ac-module application,” *IEEE Transactions on Power Electronics*, vol. 28, no. 6, pp. 2649–2663, June 2013.

[77] S. K. Mishra, K. K. Nayak, M. S. Rana, and V. Dharmarajan, “Switched-boost action based multiport converter,” *IEEE Transactions on Industry Applications*, vol. 55, no. 1, pp. 964–975, Jan 2019.

[78] H. Moradisizkoohi, N. Elsayad, M. Shojaie, and O. A. Mohammed, “Pwm plus phase-shift-modulated three-port three-level soft-switching converter using gan switches for photovoltaic applications,” *IEEE Journal of Emerging and Selected Topics in Power Electronics*, vol. 7, no. 2, pp. 636–652, June 2019.

[79] G. P. Office, “”international energy outlook 2016: With projections to 2040”,” U.S. Department of Energy, Tech. Rep., 2016. [Online]. Available: https://www.eia.gov/outlooks/ieo/pdf/0484(2016).pdf

[80] E. V. Paraskevadaki and S. A. Papathanassiou, “Evaluation of mpp voltage and power of mc-si pv modules in partial shading conditions,” *IEEE Transactions on Energy Conversion*, vol. 26, no. 3, pp. 923–932, Sep. 2011.

[81] H. Patel and V. Agarwal, “Matlab-based modeling to study the effects of partial shading on pv array characteristics,” *IEEE Transactions on Energy Conversion*, vol. 23, no. 1, pp. 302–310, March 2008.

[82] Z. Qian, O. Abdel-Rahman, H. Al-Atrash, and I. Batarseh, “Modeling and control of three-port dc/dc converter interface for satellite applications,” *IEEE*

Transactions on Power Electronics, vol. 25, no. 3, pp. 637–649, March 2010.

[83] Z. Qian, O. Abdel-Rahman, and I. Batarseh, "An integrated four-port dc/dc converter for renewable energy applications," *IEEE Transactions on Power Electronics*, vol. 25, no. 7, pp. 1877–1887, July 2010.

[84] M. A. Ramli, S. Twaha, K. Ishaque, and Y. A. Al-Turki, "A review on maximum power point tracking for photovoltaic systems with and without shading conditions," *Renewable and Sustainable Energy Reviews*, vol. 67, pp. 144–159, 2017.

[85] REN21, "Renewables 2018 global status report," *Paris: REN21 Secretariat*, 2018.

[86] A. Safari and S. Mekhilef, "Simulation and hardware implementation of incremental conductance mppt with direct control method using cuk converter," *IEEE Transactions on Industrial Electronics*, vol. 58, no. 4, pp. 1154–1161, April 2011.

[87] S. Salehi Dobakhshari, S. H. Fathi, and J. MiliMonfared, "A new fully soft-switched three-port dc/dc converter with high voltage gain and reduced number of semiconductors for hybrid energy applications," *IEEE Transactions on Power Electronics*, pp. 1–1, 2019.

[88] A. Samieipour, C. Neubauer, S. Oueslati, V. Mikli, and D. Meissner, "Ageing of kesterite solar cells 2: Impact on photocurrent generation," *Thin Solid Films*, vol. 669, pp. 509–513, 2019.

[89] F. Savoye, P. Venet, M. Millet, and J. Groot, "Impact of periodic current pulses on li-ion battery performance," *IEEE Transactions on Industrial Electronics*, vol. 59, no. 9, pp. 3481–3488, Sep. 2012.

[90] D. Selcan, G. Kirbis, and I. Kramberger, “Analog maximum power point tracking for spacecraft within a low earth orbit,” *IEEE Transactions on Aerospace and Electronic Systems*, vol. 52, no. 1, pp. 368–378, February 2016.

[91] Sharp, “Solar panel 300w – sharp nu-rc300 mono,” retrieved on 15/8/2019. [Online]. Available: https://www.sfe-solar.com/en/pv-panels/sharp-solar/solar-panel-300w-sharp-nurc300/

[92] H. A. Sher, A. F. Murtaza, A. Noman, K. E. Addoweesh, K. Al-Haddad, and M. Chiaberge, “A new sensorless hybrid mppt algorithm based on fractional short-circuit current measurement and p amp;o mppt,” *IEEE Transactions on Sustainable Energy*, vol. 6, no. 4, pp. 1426–1434, Oct 2015.

[93] S. Shongwe and M. Hanif, “Comparative analysis of different single-diode pv modeling methods,” *IEEE Journal of Photovoltaics*, vol. 5, no. 3, pp. 938–946, May 2015.

[94] S. Silvestre, A. Boronat, and A. Chouder, “Study of bypass diodes configuration on pv modules,” *Applied Energy*, vol. 86, no. 9, pp. 1632–1640, 2009.

[95] S. Sinha and S. Chandel, “Review of recent trends in optimization techniques for solar photovoltaic–wind based hybrid energy systems,” *Renewable and Sustainable Energy Reviews*, vol. 50, pp. 755–769, 2015.

[96] B. Subudhi and R. Pradhan, “A comparative study on maximum power point tracking techniques for photovoltaic power systems,” *IEEE Transactions on Sustainable Energy*, vol. 4, no. 1, pp. 89–98, Jan 2013.

[97] X. Sun, Y. Shen, W. Li, and H. Wu, “A pwm and pfm hybrid modulated three-port converter for a standalone pv/battery power system,” *IEEE Journal of*

Emerging and Selected Topics in Power Electronics, vol. 3, no. 4, pp. 984–1000, Dec 2015.

[98] SunPower, "Sunpower x-series: X22-370 datasheets." [Online]. Available: https://us.sunpower.com/sites/default/files/sp-x22-370-ds-en-ltr-mc4comp-527787.pdf

[99] K. Suresh, N. Chellammal, C. Bharatiraja, P. Sanjeevikumar, F. Blaabjerg, and J. B. H. Nielsen, "Cost-efficient nonisolated three-port dc-dc converter for ev/hev applications with energy storage," *International Transactions on Electrical Energy Systems*, p. e12088, 2019.

[100] P. Suskis and I. Galkin, "Enhanced photovoltaic panel model for matlab-simulink environment considering solar cell junction capacitance," in *IECON 2013 - 39th Annual Conference of the IEEE Industrial Electronics Society*, Nov 2013, pp. 1613–1618.

[101] H. Tao, J. L. Duarte, and M. A. M. Hendrix, "Three-port triple-half-bridge bidirectional converter with zero-voltage switching," *IEEE Transactions on Power Electronics*, vol. 23, no. 2, pp. 782–792, March 2008.

[102] H. Tao, A. Kotsopoulos, J. L. Duarte, and M. A. M. Hendrix, "Transformer-Coupled Multiport ZVS Bidirectional DC–DC Converter With Wide Input Range," *IEEE Transactions on Power Electronics*, vol. 23, no. 2, pp. 771–781, March 2008.

[103] A. Tariq and M. S. J. Asghar, "Development of an analog maximum power point tracker for photovoltaic panel," in *2005 International Conference on Power Electronics and Drives Systems*, vol. 1, Nov 2005, pp. 251–255.

[104] D. M. Tobnaghi, "Recovery of the electrical parameters of degraded solar cells by ultrasonic treatment," *Journal of Electrical Engineering & Technology*,

vol. 11, no. 5, pp. 1337–1341, 2016.

[105] D. o. E. United Nations and S. Affairs, "Population division (2017). world population prospects: The 2017 revision, key findings and advance tables," *Working Paper No. ESA/P/WP/248.*, 2017.

[106] V. Vega-Garita, A. P. Harsarapama, L. Ramirez-Elizondo, and P. Bauer, "Physical integration of pv-battery system: Advantages, challenges, and thermal model," in *2016 IEEE International Energy Conference (ENERGYCON).* IEEE, 2016, pp. 1–6.

[107] V. Vega-Garita, L. Ramirez-Elizondo, and P. Bauer, "Physical integration of a photovoltaic-battery system: A thermal analysis," *Applied energy*, vol. 208, pp. 446–455, 2017.

[108] M. G. Villalva, J. R. Gazoli, and E. R. Filho, "Comprehensive approach to modeling and simulation of photovoltaic arrays," *IEEE Transactions on Power Electronics*, vol. 24, no. 5, pp. 1198–1208, May 2009.

[109] L. Wang, Z. Wang, and H. Li, "Asymmetrical duty cycle control and decoupled power flow design of a three-port bidirectional dc-dc converter for fuel cell vehicle application," *IEEE Transactions on Power Electronics*, vol. 27, no. 2, pp. 891–904, Feb 2012.

[110] W. Wang, A. C. Liu, H. S. Chung, R. W. Lau, J. Zhang, and A. W. Lo, "Fault diagnosis of photovoltaic panels using dynamic current–voltage characteristics," *IEEE Transactions on Power Electronics*, vol. 31, no. 2, pp. 1588–1599, Feb 2016.

[111] Y. Wang, F. Han, L. Yang, R. Xu, and R. Liu, "A three-port bidirectional multi-element resonant converter with decoupled power flow management for hybrid energy storage systems," *IEEE Access*, vol. 6, pp. 61 331–61 341, 2018.

[112] Y. Wang, Y. Li, and X. Ruan, "High-accuracy and fast-speed mppt methods for pv string under partially shaded conditions," *IEEE Transactions on Industrial Electronics*, vol. 63, no. 1, pp. 235–245, Jan 2016.

[113] Z. Wang and H. Li, "An integrated three-port bidirectional dc–dc converter for pv application on a dc distribution system," *IEEE Transactions on Power Electronics*, vol. 28, no. 10, pp. 4612–4624, Oct 2013.

[114] H. Wu, R. Chen, J. Zhang, Y. Xing, H. Hu, and H. Ge, "A family of three-port half-bridge converters for a stand-alone renewable power system," *IEEE Transactions on Power Electronics*, vol. 26, no. 9, pp. 2697–2706, Sep. 2011.

[115] H. Wu, K. Sun, R. Chen, H. Hu, and Y. Xing, "Full-bridge three-port converters with wide input voltage range for renewable power systems," *IEEE Transactions on Power Electronics*, vol. 27, no. 9, pp. 3965–3974, Sept 2012.

[116] H. Wu, K. Sun, S. Ding, and Y. Xing, "Topology derivation of nonisolated three-port dc–dc converters from dic and doc," *IEEE Transactions on Power Electronics*, vol. 28, no. 7, pp. 3297–3307, July 2013.

[117] H. Wu, Y. Xing, Y. Xia, and K. Sun, "A family of non-isolated three-port converters for stand-alone renewable power system," in *IECON 2011-37th Annual Conference on IEEE Industrial Electronics Society*. IEEE, 2011, pp. 1030–1035.

[118] T. Wu, W. Li, K. Ni, S. Song, and M. Alkahtani, "Modular tri-port converter for switched reluctance motor based hybrid electrical vehicles," *IEEE Access*, vol. 7, pp. 15 989–15 998, 2019.

[119] J. Zeng, W. Qiao, and L. Qu, "An isolated three-port bidirectional dc–dc converter for photovoltaic systems with energy storage," *IEEE Transactions on Industry Applications*, vol. 51, no. 4, pp. 3493–3503, July 2015.

[120] J. Zhang, H. Wu, X. Qin, and Y. Xing, “Pwm plus secondary-side phase-shift controlled soft-switching full-bridge three-port converter for renewable power systems,” *IEEE Transactions on Industrial Electronics*, vol. 62, no. 11, pp. 7061–7072, Nov 2015.

[121] N. Zhang, D. Sutanto, and K. M. Muttaqi, “A review of topologies of three-port dc–dc converters for the integration of renewable energy and energy storage system,” *Renewable and Sustainable Energy Reviews*, vol. 56, pp. 388–401, 2016.

[122] C. Zhao, S. D. Round, and J. W. Kolar, “An isolated three-port bidirectional dc-dc converter with decoupled power flow management,” *IEEE Transactions on Power Electronics*, vol. 23, no. 5, pp. 2443–2453, Sep. 2008.

[123] H. Zheng, S. Li, R. Challoo, and J. Proano, “Shading and bypass diode impacts to energy extraction of pv arrays under different converter configurations,” *Renewable Energy*, vol. 68, pp. 58–66, 2014.

[124] H. Zhu, D. Zhang, H. S. Athab, B. Wu, and Y. Gu, “Pv isolated three-port converter and energy-balancing control method for pv-battery power supply applications,” *IEEE Transactions on Industrial Electronics*, vol. 62, no. 6, pp. 3595–3606, June 2015.

[125] H. Zhu, D. Zhang, B. Zhang, and Z. Zhou, “A nonisolated three-port dc–dc converter and three-domain control method for pv-battery power systems,” *IEEE Transactions on Industrial Electronics*, vol. 62, no. 8, pp. 4937–4947, Aug 2015.